

Matter waves from localized sources in homogeneous force fields

Dissertation
von
Tobias Kramer

30. Januar 2003

Physik-Department der Technischen Universität München
Institut für theoretische Physik T30

Matter waves from localized sources in homogeneous force fields

Tobias Kramer

Vollständiger Abdruck der von der Fakultät für Physik der Technischen Universität München zur Erlangung des akademischen Grades eines Doktors der Naturwissenschaften (Dr. rer. nat.) genehmigten Dissertation.

Vorsitzender: Univ.-Prof. Dr. Gerhard Abstreiter

Prüfer der Dissertation:

1. Univ.-Prof. Dr. Manfred Kleber
2. Hon.-Prof. Dr. Ignacio Cirac

Die Dissertation wurde am 30.1.2003 bei der Technischen Universität München eingereicht und durch die Fakultät für Physik am 3.4.2003 angenommen.

Contents

Contents	i
List of Figures	iii
1 Introduction	1
2 Sources in quantum mechanics	3
2.1 Interference of matter waves	3
2.2 Currents generated by quantum sources	11
2.3 Feynman's path integral	14
3 Properties of Green functions	17
3.1 The energy-dependent Green function	17
3.2 Connection to Fermi's golden rule	21
3.3 The general quadratic Hamiltonian	23
3.4 Multipole sources	25
3.5 Green functions from complex integration	28
4 Uniform magnetic and electric fields	35
4.1 Gauge properties of the Green function	35
4.2 Propagator in crossed magnetic and electric fields	37
4.3 Purely electric field	38
4.4 Parallel magnetic and electric fields	39
4.5 Purely magnetic field	47
4.6 Crossed magnetic and electric fields	49
5 Currents in 2D electric and magnetic fields	53
5.1 Two-dimensional Green function for crossed fields	53
5.2 Properties of the two-dimensional density of states	59
5.3 Spin and effective mass	62
5.4 Conductivity in the quantum Hall regime	63

6	Source model in strong fields	69
6.1	Connection to experiments	69
6.2	Predictions for the photodetachment rate	75
7	Spatially extended quantum sources	77
7.1	Gaussian source distribution in a linear force field	78
7.2	Gaussian sources in parallel fields	82
7.3	General source distribution	83
7.4	The Franck-Condon principle	86
8	Atom laser	91
8.1	Bose-Einstein condensation	91
8.2	Radio output coupling from a BEC	93
8.3	Transition from a BEC state to the gravitational field	94
8.4	Energy range for the operation of an atom laser	95
8.5	Vortices and atom lasers	96
9	Summary	107
A	Linear canonical transformation	111
A.1	Evaluation of the matrix representation	111
A.2	Homogeneous fields at arbitrary angles	112
B	Integrals involving Airy functions	115
C	Useful relations involving Hermite polynomials	119
D	The reflection approximation	121
	References	123
	List of publications	131
	Danksagung	133
	Lebenslauf	135

List of Figures

2.1	Two slit experiments.	4
2.2	Probability density for a two-slit configuration	6
2.3	Probability density for a uniform field	8
2.4	Trajectories in the uniform field	9
2.5	Pulsed emission from a quantum source in a linear field	10
2.6	Potential scattering and long range forces	11
3.1	Saddle points in the complex plane	29
3.2	Uniform Airy and saddle point approximation	34
4.1	Total current from multipole sources in parallel fields	41
4.2	Current density in parallel fields: overview	43
4.3	Current density in parallel fields: four path interference	45
4.4	Lateral uncertainty product in parallel fields	46
4.5	Density of states in a 3D electron gas with magnetic field	49
4.6	Propagator for crossed fields in three dimensions.	50
4.7	Total current in crossed fields in three dimensions	51
5.1	2D electronic density of states in crossed fields	60
5.2	Hall resistance ρ_{xy} and longitudinal resistance ρ_{xx} as a function of the magnetic field.	65
5.3	Breakdown of the quantized Hall resistance.	66
6.1	Photodetachment in crossed fields at different temperatures.	73
6.2	Zeeman splitted energy levels in sulfur.	74
6.3	Photodetachment rate of S^- in crossed fields	75
7.1	Virtual point source for a Gaussian distribution	79
7.2	Transition from a point-like to an extended source in a linear potential. . .	81
7.3	Transition from a point-like to an extended source in a quadratic potential. .	84
7.4	Franck-Condon factor in the quantum source model	87
8.1	Ground state of a Bose-Einstein condensate	93
8.2	Total current of an atom-laser: theory vs. experiment	96

8.3	Current density of an atom-laser for different BEC sizes	97
8.4	Total current originating from a single vortex	100
8.5	Atom laser density profiles for a single vortex	101
8.6	BEC wave function with an embedded vortex lattice	103
8.7	Total current originating from a vortex lattice	105
8.8	Atom laser beam profile originating from a vortex lattice	106

Chapter 1

Introduction

The motion of particles in a uniform force field is a standard subject of classical mechanics. For given initial momentum and position, the equations of motion contain all information about the further path of the particle. In quantum mechanics the simultaneous specification of position and momentum is not possible. However, the question of how a particle evolves, that starts at a given time, or, alternatively, with fixed energy from a well-defined place is meaningful. A convenient way to deal with these initial conditions is the use of the time-evolution operator in its coordinate representation (the propagator) and its Laplace transform, the so-called energy-dependent Green function. The systematic study of propagators is progressing well, as recent compilations of known solutions show (i.e. about 1000 references in [GS98]). Unfortunately, the situation for three-dimensional energy-dependent Green functions is not keeping pace, and “simple” analytic solutions for only six(!) cases are known: the free particle; a particle subject to uniform electric or magnetic fields; the isotropic harmonic oscillator; the Coulomb potential; and the combination of parallel electric and magnetic fields.

More analytic solutions are urgently needed, since perturbation theory for constant or linear (and therefore extremely long range) potentials is not applicable. The availability of the Green function offers the possibility to treat stationary scattering problems by obtaining the total scattering current and the spatial density distribution. Combined with quantum-source formalism, more complicated emission characteristics and distributions of particle emitting sources can be incorporated in the calculations. Due to the known differentiation properties of an analytically given Green function, most of the results for the currents can again be evaluated as closed expressions. The density of states in electronic systems is also directly related to the energy-dependent Green function and is highly relevant for the calculation of electric, magnetic and thermal properties of materials.

The six already available Green functions have profound implications for many different physical systems: the angular momentum dependence of continuum cross sections was studied by Wigner; photodetachment experiments into external fields probe the binding energy of electrons with unprecedented accuracy; and the interference of atomic matter waves in the gravitational field has become a standard topic in quantum optics. Likewise many effects in solid state physics depend on the density of states in the presence of external

fields. In all these cases a formulation in terms of Green functions is possible and this, in turn, leads to a coherent theoretical description.

How can we find new energy-dependent Green functions? A thoroughly mathematical understanding of the propagator is needed, since it provides one possibility to construct the corresponding Green functions by a Laplace transform. The theory of residues is one main ingredient for the calculations. However, the singularities of the propagator often show a complicated structure and render this method unusable. A numerical integration is frequently difficult, since the strong oscillations of the propagator lead to the cancellation of terms that affect the accuracy critically. The analytic construction of the Green function is a main topic of this thesis. The second one is the application and demonstration of the Green function in a variety of systems and processes in quantum physics.

In the next chapter we will show how in the quantum realm interference phenomena in uniform fields emerge and establish a theoretical description that is suitable for scattering from localized sources into external fields. The quantum-source approach provides an excellent theoretical basis for the embedding of localized sources into external potentials. As a first example we review two-slit experiments and show how a uniform field provides a virtual double-slit for emitted waves from a quantum source.

In Chapter 3 we review different mathematical concepts and apply them to the calculation of Green functions. The presence of magnetic and electric fields leads to quadratic Hamiltonians in the momentum and position operators. We analyze and construct Green functions for this type of Hamiltonian in Chapter 4 and look for general properties that simplify the calculations. A comparison with semiclassical results and approximations helps to clarify the influence of classical physics on the quantum results.

In specific applications given in Chapters 5 and 6 we use the newly derived results to obtain insight into the effects of constant fields on two-dimensional and three-dimensional systems. The quantum Hall effect is a prime example, since it involves crossed electric and magnetic fields in a two-dimensional system.

The recent advances in the cooling of trapped gases and the formation of coherent atomic ensembles containing thousands of atoms in a spatially localized quantum state allow the construction of a macroscopic source for matter waves. The theoretical description of waves from an extended source in Chapters 7 and 8 is necessary for understanding the efficiency of such a source and studying the interference phenomena of these waves. A completely analytical theory of extended quantum sources is not easily accomplished, but we solve very useful reference cases that allow to establish the range of validity for some commonly applied approximations. Finally, a summary of the obtained results is given in Chapter 9.

Chapter 2

A source term in the Schrödinger equation

In this chapter we aim to establish a scattering theory which is useful for the description of spatially localized sources of particles. As the starting point for a more formal treatment of the theory, we introduce the quantum propagator and apply it to two physical systems. Feynman's approach to space-time quantum-mechanics relies on these propagators [FH65] (sometimes called Feynman path integrals) and one major advantage of the propagator formalism is the consistent treatment of interference phenomena in terms of trajectories. The idea of quantum sources was promoted by Schwinger [Sch73] and we will see how these sources naturally arise in the context of scattering theory.

2.1 Interference of matter waves

Before we discuss interference phenomena we have to recall some basic concepts of time-dependent quantum mechanics. The following analysis makes extensive use of propagator methods to calculate the time evolution of an initial quantum state. At time $t = t_0$ the initial state is given by

$$\psi(\mathbf{r}, t = t_0) = \langle \mathbf{r} | \psi(t = t_0) \rangle, \quad (2.1)$$

and the time evolution of this state is governed by the time-dependent Schrödinger equation

$$[i\hbar\partial_t - \mathbf{H}] |\psi(t)\rangle = 0. \quad (2.2)$$

The formal solution of equation (2.2) can be expressed with the time evolution operator $U(t, t_0)$:

$$|\psi(t)\rangle = U(t, t_0) |\psi(t = t_0)\rangle. \quad (2.3)$$

The introduction of the time evolution operator allows us to convert the differential Schrödinger equation (2.2) to an integral equation:

$$\langle \mathbf{r} | \psi(t) \rangle = \int d^3\mathbf{r}' \langle \mathbf{r} | U(t, t_0) | \mathbf{r}' \rangle \langle \mathbf{r}' | \psi(t = t_0) \rangle. \quad (2.4)$$

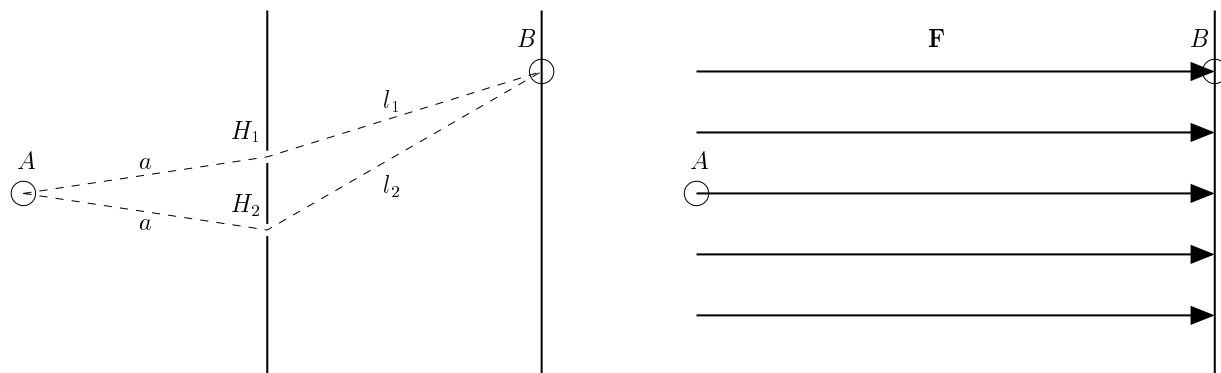


Figure 2.1: Left panel: Configuration for a typical two slit experiment. Particles emitted at A travel through the two holes H_1 and H_2 to the detector at position B . Right panel: The particle source and the detector are now placed in a uniform force field \mathbf{F} .

The coordinate space representation of the time evolution operator is often called propagator or Feynman kernel and commonly denoted by

$$K(\mathbf{r}, t | \mathbf{r}', t_0) \equiv \langle \mathbf{r} | U(t, t_0) | \mathbf{r}' \rangle. \quad (2.5)$$

Directly related to the propagator is the notion of the time-dependent Green function. Since we are mainly concerned with non-relativistic quantum mechanics, we will only discuss the evolution of states evolving in positive direction of time ($t > t_0$). Causality enforces the use of the time-retarded Green function

$$G(\mathbf{r}, t; \mathbf{r}', t_0) \equiv -\frac{i}{\hbar} \Theta(t - t_0) K(\mathbf{r}, t | \mathbf{r}', t_0). \quad (2.6)$$

The Green function itself is a solution to the differential equation

$$[i\hbar\partial_t - \mathbf{H}] G(\mathbf{r}, t; \mathbf{r}', t_0) = \delta^{(3D)}(\mathbf{r} - \mathbf{r}') \delta(t - t_0), \quad (2.7)$$

which has on the left hand side the same structure as the Schrödinger equation (2.2). However, at $\mathbf{r} = \mathbf{r}'$ the kernel becomes singular in coordinate space since $U(t_0, t_0) \equiv 1$ and the inhomogeneity on the right hand side of equation (2.7) arises. From the derivative of the step function $\Theta(t - t_0)$ we obtain another delta function in the time-parameter for $t = t_0$. A systematic treatment of the retarded Green function will be given in Chapter 3.

We continue our discussion with the comparison of two seemingly different physical systems, which share a surprisingly similar behavior. The first system is a typical two-slit interference experiment, shown on the left panel in Figure 2.1. A quantum-particle source emits monochromatic particles at point A . From A the resulting matter waves travel through a field free region to a wall with two holes, H_1 and H_2 . On a distant screen we place a particle detector at position B . On the right hand side of Figure 2.1 we sketch a different system with an electron emitting source located again at A . This time, however, the emitted electrons travel in a uniform and constant force field \mathbf{F} to the

detector at point B . We want to calculate the probability amplitude that a particle which is emitted from the source located at A arrives on the detector screen at B . To simplify our considerations, we will assume a point source of particles. According to the definition of the propagator in equation (2.7), the kernel describes the evolution of an initially sharply localized “state” $\delta(\mathbf{r} - \mathbf{r}')$ and therefore contains all necessary information to answer our question about the probability amplitude. The remaining task is to write down and to evaluate the propagators for the two different experimental setups. Since the double-slit configuration contains two possible particle paths, one from $A \rightarrow H_1 \rightarrow B$ and the other one from $A \rightarrow H_2 \rightarrow B$, we have to form a superposition of the two probability amplitudes

$$\begin{aligned} K_{\text{slit}}(B, T|A, 0) &= \int_0^T dt_1 K_{\text{free}}(B, T|H_1, t_1) K_{\text{free}}(H_1, t_1|A, 0) \\ &+ \int_0^T dt_2 K_{\text{free}}(B, T|H_2, t_2) K_{\text{free}}(H_2, t_2|A, 0). \end{aligned} \quad (2.8)$$

By integrating over t_1 and t_2 from 0 to T we consider a time evolution that starts at $t = 0$ at A and ends at $t = T$ at B . In between a passage through the holes occurs at some intermediate time t_i . We also use the composition property of the time evolution operator $U(t_3, t_2)U(t_2, t_1) = U(t_3, t_1)$. The propagator in the field free region is denoted by K_{free} . Methods for calculating the kernel are discussed in Chapter 3. Here, we will just quote the analytic result for the free propagator

$$K_{\text{free}}(\mathbf{r}, t|\mathbf{r}', t') = \left(\frac{m}{2\pi i \hbar (t - t')} \right)^{3/2} \exp \left(\frac{im|\mathbf{r} - \mathbf{r}'|^2}{2\hbar(t - t')} \right). \quad (2.9)$$

Knowing the form of the propagator, we have to carry out the intermediate time integration over t_i . However, in an experimental setup we would like to eliminate the need to measure exactly at time T . Instead one prefers to record a static pattern on the detector screen. Mathematically, we can calculate the stationary probability amplitude by taking the Laplace transform of the time retarded Green function

$$G_{\text{slit}}(\mathbf{r}, t; \mathbf{r}', 0) = -\frac{i}{\hbar} \theta(t) K_{\text{slit}}(\mathbf{r}, t|\mathbf{r}', 0) \quad (2.10)$$

with respect to the energy E of the emitted particle:

$$\begin{aligned} G_{\text{slit}}(A, B; E) &= -\frac{i}{\hbar} \int_0^\infty dT e^{-iET/\hbar} K_{\text{slit}}(A, T|B, 0) \\ &= -\frac{i}{\hbar} \int_0^\infty dT e^{-iET/\hbar} \sum_{i=1}^2 \int_0^T dt_i K_{\text{free}}(B, T|H_i, t_i) K_{\text{free}}(H_i, t_i|A, 0) \end{aligned} \quad (2.11)$$

At this point it is convenient to introduce the Laplace transform of the free particle propagator

$$\begin{aligned} G_{\text{free}}(\mathbf{r}, \mathbf{r}'; E) &= -\frac{i}{\hbar} \int_0^\infty dT e^{-iET/\hbar} K_{\text{free}}(\mathbf{r}, T|\mathbf{r}', 0) \\ &= -\frac{m}{2\pi \hbar^2 |\mathbf{r} - \mathbf{r}'|} \exp \left(\frac{i}{\hbar} \sqrt{2mE} |\mathbf{r} - \mathbf{r}'| \right). \end{aligned} \quad (2.12)$$

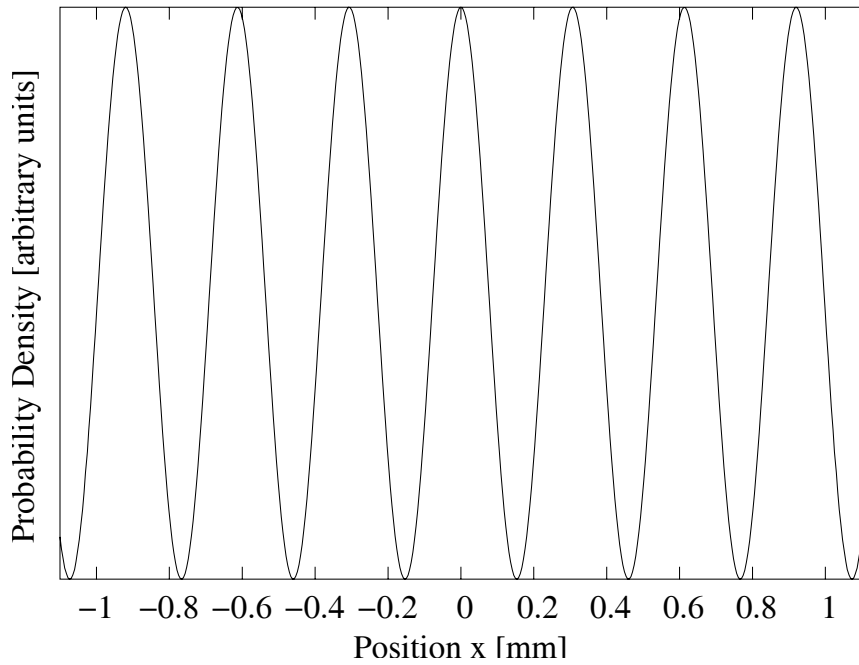


Figure 2.2: Probability density on a distant detector plane for electrons passing through two slits. Parameters: Distance between the holes 0.2 mm, distance between slit and detector plane 0.5 m, initial energy $E = 100 \mu\text{eV}$.

Using the convolution theorem for the Laplace transform (see [AS65], 29.2.8)

$$\int_0^\infty dt e^{-st} \int_0^t d\tau F_1(t-\tau)F_2(\tau) = \left(\int_0^\infty dt e^{-st} F_1(t) \right) \left(\int_0^\infty dt e^{-st} F_2(t) \right), \quad (2.13)$$

we can rewrite the probability amplitude according to equation (2.11) as

$$\begin{aligned} G_{\text{slit}}(A, B; E) &= -\frac{i}{\hbar} \int_0^\infty dT e^{-iET/\hbar} K_{\text{slit}}(A, T|B, 0) \\ &= -\frac{i}{\hbar} \int_0^\infty dT e^{-iET/\hbar} \sum_{i=1}^2 \int_0^T dt_i K_{\text{free}}(B, T-t_i|H_i, 0) K_{\text{free}}(H_i, t_i|A, 0) \\ &= i\hbar \sum_{i=1}^2 G_{\text{free}}(B, H_i; E) G_{\text{free}}(H_i, A; E). \end{aligned} \quad (2.14)$$

Figure 2.2 shows the probability density $|G_{\text{slit}}(A, B; E)|^2$ of electrons at a screen 0.5 m displaced from the slits. The familiar two-slit interference pattern is clearly visible. The use of point-like slits simplified the calculation considerably. Including effects of a finite slit width requires additional integrations and is more complicated [FH65] because the sharp

edges of the slit produce Fresnel-type interference patterns [Mos52]. The somewhat arbitrary introduction of a Gaussian transparency function for each slit simplifies the situation drastically and yields similar results as the use of point-like slits [FH65].

Instead of further investigating these details of the two-slit experiment we will now discuss the second experimental configuration depicted on the right hand side of Figure 2.1. In 1981 Demkov, Kondratovich, Ostrovskii, and Fabrikant pointed out that a linear force field can act as a double slit without the need for an actual material slit [DKO82, Fab81]. In the language of quantum propagators this situation was accurately analyzed by Bracher [Bra99]. The propagator for a particle in a uniform force field $\mathbf{F} = F\mathbf{e}_z$ is given by

$$K_{\text{field}}(\mathbf{r}, t | \mathbf{r}', t') = \left(\frac{m}{2\pi i \hbar T} \right)^{3/2} \exp \left(\frac{im|\mathbf{r} - \mathbf{r}'|^2}{2\hbar T} + \frac{iFT}{2\hbar}(z + z') - \frac{iF^2 T^3}{24m\hbar} \right), \quad (2.15)$$

where $T = t - t'$. As before, we want to calculate the probability amplitude for a particle traveling from the source A to hit the detector at B (see Figure 2.1). Using again a monochromatic particle source, the stationary probability amplitude is derived similarly to equation (2.11) and reads

$$G_{\text{field}}(\mathbf{r}, \mathbf{r}'; E) = -\frac{i}{\hbar} \int_0^\infty dT \left(\frac{m}{2\pi i \hbar T} \right)^{3/2} \exp(iET/\hbar) \times \exp \left(\frac{im|\mathbf{r} - \mathbf{r}'|^2}{2\hbar T} + \frac{iFT}{2\hbar}(z + z') - \frac{iF^2 T^3}{24m\hbar} \right). \quad (2.16)$$

Although $G_{\text{field}}(\mathbf{r}, \mathbf{r}'; E)$ is available in closed analytic form (see Chapter 3), we will retain the integral form for the following discussion. We can approximate the integral with the method of stationary phases for a wide range of parameters. At a stationary point the derivative with respect to T of the exponent in equation (2.16) vanishes and we get a large contribution from the region close to this point to the otherwise oscillatory integral (a general description of the method of stationary phases is presented in Chapter 3). For G_{field} the stationary points of the exponent are readily obtained from the condition

$$E - \frac{m|\mathbf{r} - \mathbf{r}'|^2}{2T^2} + \frac{F}{2}(z + z') - \frac{F^2 T^2}{8m} \stackrel{!}{=} 0. \quad (2.17)$$

This biquadratic expression in T has two roots, denoted by T_1 and T_2

$$T_{1,2}(\mathbf{r}, \mathbf{o}; E) = \frac{\sqrt{m}}{F} \left(\sqrt{2E + F(r+z)} \pm \sqrt{2E - F(r-z)} \right). \quad (2.18)$$

Here, we will assume $E > 0$ and $2E - F(r-z) > 0$. Then we obtain two real-valued solutions for the time of flight T_i . Replacing the integral in equation (2.16) by a sum comprising these two stationary points yields

$$G_{\text{field}}(\mathbf{r}, \mathbf{o}; E) \approx -\frac{i}{\hbar} \sum_{i=1}^2 a(T_i) \sqrt{\frac{2\pi\hbar}{\left| \frac{\partial S_{\text{cl}}(\mathbf{r}, T, \mathbf{o}, 0)}{\partial T^2} \right|}} e^{\frac{iET}{\hbar} + \frac{i}{\hbar} S_{\text{cl}}(\mathbf{r}, T, \mathbf{o}, 0) + \frac{i\pi}{4} \text{sgn} \left[\frac{\partial S_{\text{cl}}(\mathbf{r}, T, \mathbf{o}, 0)}{\partial T^2} \right]} \Bigg|_{T=T_i}, \quad (2.19)$$

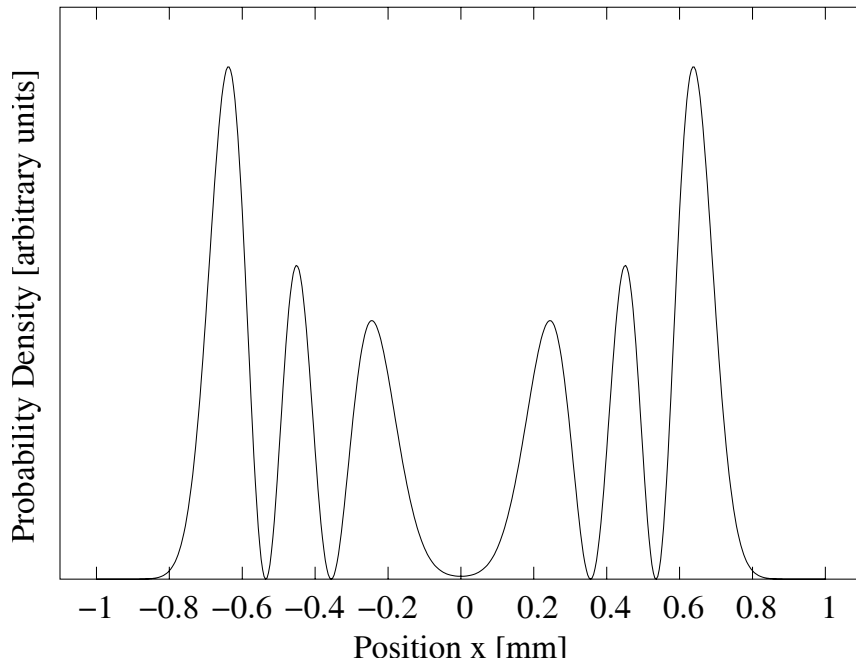


Figure 2.3: Probability density on a distant detector plane for electrons emitted in a uniform electric field. Distance from the source to the detector plane 0.5 m, field strength 400 V/m, initial energy 100 μeV .

where

$$a(T) = \left(\frac{m}{2\pi i \hbar T} \right)^{3/2}, \quad \text{and} \quad S_{\text{cl}}(\mathbf{r}, T, \mathbf{r}', 0) = \frac{m|\mathbf{r} - \mathbf{r}'|^2}{2T} + \frac{FT}{2}(z + z') - \frac{F^2 T^3}{24m}. \quad (2.20)$$

The sum representing the Green function resembles equation (2.14), which was derived for the two-slit propagator. Indeed, the plot of the probability density $|G_{\text{field}}^{\text{stat}}(A, B; E)|^2$ in Figure 2.3 shows pronounced interference fringes. The spacing of the fringes depends on the energy of the emitted particles E , the strength of the uniform force field F and the distance between source and detector (r, z) .

The number of contributing stationary points is related to the classical equations of motion. The propagator of a Hamiltonian which is at most quadratic in x and p (i.e. the uniform field) can always be written in the form

$$K(\mathbf{r}, t | \mathbf{r}', t') = a(t, t') \exp\left(\frac{i}{\hbar} S_{\text{cl}}(\mathbf{r}, t, \mathbf{r}', t') \right), \quad (2.21)$$

where $S_{\text{cl}}(\mathbf{r}, t, \mathbf{r}', t')$ denotes the classical action defined by the integral of the Lagrangian [Pau51]

$$S_{\text{cl}}(\mathbf{r}, t, \mathbf{r}', t') = \int_{\mathbf{q}(t')=\mathbf{r}'}^{\mathbf{q}(t)=\mathbf{r}} dt L(\mathbf{q}, \dot{\mathbf{q}}, t). \quad (2.22)$$

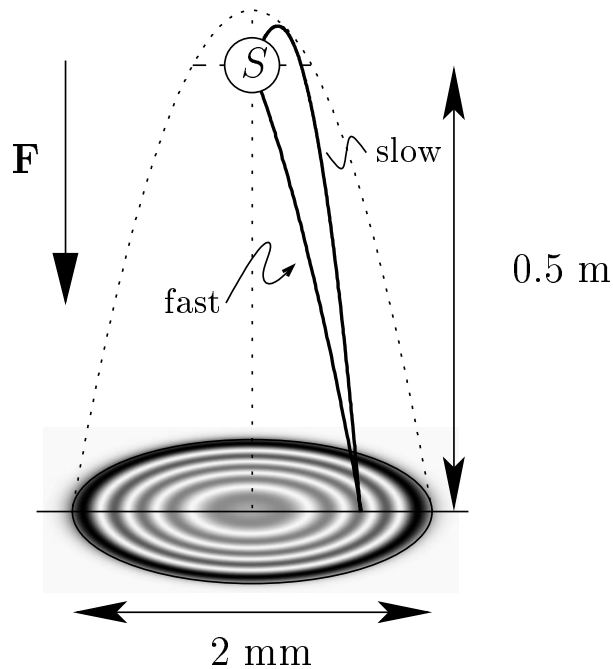


Figure 2.4: Trajectories in the uniform force field \mathbf{F} . The dashed parabola denotes the classical accessible region. In this region, two trajectories with the same energy connect the source S with a point on the detector plane. For electrons emitted in an electric field macroscopically visible interference fringes emerge.

The stationary points T_k of the exponent of the kernel

$$E + \left. \frac{\partial S_{\text{cl}}(\mathbf{r}, T, \mathbf{r}', 0)}{\partial T} \right|_{T=T_k} = 0 \quad (2.23)$$

are therefore identical to the extrema of the classical action. From the Lagrange formulation of classical mechanics we know that T_k is the time of flight for the motion of a point-mass from the starting-point A to the end-point B with initial kinetic energy E . In the case of the uniform field we get two stationary points, corresponding to one slow and one fast trajectory connecting A with B . The existence of two parabolic trajectories in a linear potential with the same energy but different time of flights from one point to another was first analyzed by Galilei [Gal38]. In Figure 2.4 we plot the two trajectories which constitute the intrinsic double-slit of a uniform force field.

Experimental data for both types of slits are available. Using an electron source and a material two-slit Jönsson obtained beautiful pictures of the interference structure in 1959 [MJ59]. Following the idea of Demkov et al. [DKO82, Fab81], Blondel constructed a device to realize the field double-slit (also for electrons), the so-called photodetachment-microscope [BDD96, BDDV99].

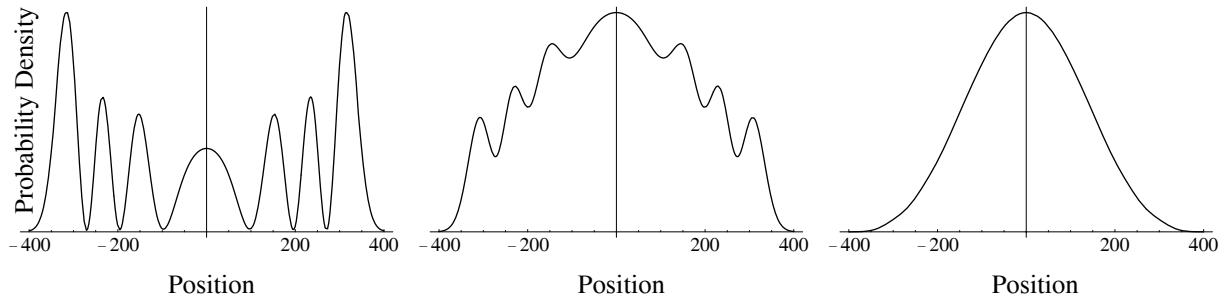


Figure 2.5: Pulsed emission from a quantum source in a linear force field. From left to right we reduce the pulse half-width from $10\Delta T$, $3\Delta T$ to $2\Delta T$, where ΔT denotes the difference in the time of flight along the two trajectories. The interference fringes disappear, since we effectively eliminate a second path.

Example 1 (Non-stationary source in a uniform field) One may ask what happens to the interference pattern if we send out particles only during a short period of time which may become shorter than the difference of the classical times of flight. This question is interesting, because we can study how quantum mechanics reacts to this de-facto elimination of a second path. It seems that the influence of this so-called pulsed emission on the probability density has not been studied before in the literature, only the total emission rate of a pulsed point-source into a linear force field is considered in [WS93, ZDM99]. With the help of the propagator we can determine the density distribution. Equation (2.18) gives the time difference between the two stationary points

$$\Delta T = T_2 - T_1 = 2\frac{\sqrt{m}}{F}\sqrt{2E - F(r - z)}. \quad (2.24)$$

To model the pulsed emission we introduce a quantum source with a time-dependent emission rate. For simplicity we assume a Gaussian time-dependence and thus amend equation (2.16) with an additional real-valued term $-T^2/(2\lambda^2)$ in the exponent:

$$G_{\text{field}}^{\text{pulsed}}(\mathbf{r}, \mathbf{r}'; E) = -\frac{i}{\hbar} \int_0^\infty dT \left(\frac{m}{2\pi i \hbar T} \right)^{3/2} \exp(iET/\hbar) \times \\ \times \exp\left(\frac{im|\mathbf{r} - \mathbf{r}'|^2}{2\hbar T} + \frac{iFT}{2\hbar}(z + z') - \frac{iF^2 T^3}{24m\hbar} - \frac{T^2}{2\lambda^2} \right). \quad (2.25)$$

The parameter λ is related to the length of the emitted pulse. We can proceed in our calculation as before. However, we get new values for the stationary points of the exponent. Because λ is real valued whereas $iS_{\text{cl}}(\mathbf{r}, T, \mathbf{o}, 0)/\hbar$ is purely imaginary, the stationary points are shifted into the complex t -plane. A positive imaginary part reduces the contribution of the corresponding stationary point to the integral. Strongly pronounced interference fringes are only possible if the contributions of both stationary points are approximately equal in magnitude. Since this is no longer the case, the fringes slowly disappear for decreasing pulse time, as Figure 2.5 shows. By changing the pulse length we can effectively control

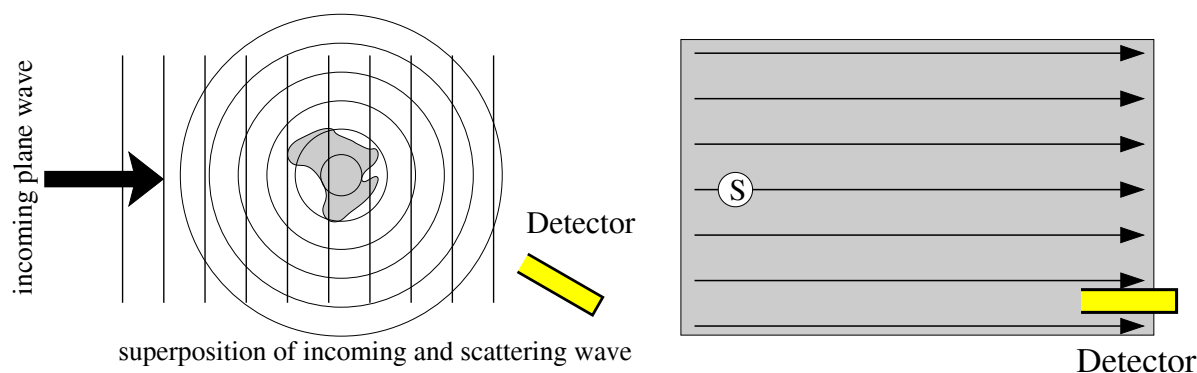


Figure 2.6: Potential scattering and long range forces. Left panel: In the conventional potential scattering situation boundary conditions are imposed by incoming plane waves. Outside an interaction region (shaded area) we observe a superposition of the incoming and the scattering wave. Right panel: In the presence of constant force-fields we have to incorporate the potentials in the Schrödinger equation. Also, the detector is located in the potential. Boundary conditions are specified by describing the originating source S of the particles.

the two-slit experiment and the appearance of interference phenomena.

Up to now we did not consider a specific initial wave function but only the propagator and the Green function of the underlying Hamiltonian. We also frequently used the term “source” for the emission of particles from a localized point in space. To put the presented ideas in the context of a more rigorously defined theory, we will introduce and review a coherent approach to quantum sources based on the formalism of Green functions.

2.2 Currents generated by quantum sources

Scattering theory is treated in a special way in quantum mechanics. Whereas normally the particle number is a conserved quantity, in scattering processes we often assume a reservoir or source which supplies a constant flux of particles. If the particle sources are located far away from the scattering region, they give rise to boundary conditions on the incoming particle flux in the form of incoming plane waves. However, if we deal with long range (or even constant) potentials, a different approach is feasible with the introduction of quantum sources. These sources are located inside the interaction region and emit particles with a well defined energy. A sketch of this situation is shown in Figure 2.6. The concept of sources is also familiar from electrodynamics. Schwinger introduced quantum sources in quantum field theories [Sch73] in order to avoid the use of operator fields. He also considered the non-relativistic limit of such a particle source.

2.2.1 Elastic scattering and quantum sources

In potential scattering theory, the total wave function $\psi(\mathbf{r})$ of the Hamiltonian \mathbf{H} (including the vector potential \mathbf{A})

$$\mathbf{H} = \frac{(\mathbf{p} - e\mathbf{A}(\mathbf{r})/c)^2}{2m} + V(\mathbf{r}) \quad (2.26)$$

is normally written as a superposition of an incident wave function $\psi_{\text{in}}(\mathbf{r})$ and a wave function originating from the scattering region $\psi_{\text{sc}}(\mathbf{r})$:

$$\psi(\mathbf{r}) = \psi_{\text{in}}(\mathbf{r}) + \psi_{\text{sc}}(\mathbf{r}). \quad (2.27)$$

The incident wave $\psi_{\text{in}}(\mathbf{r})$ is an eigenfunction of the modified Hamiltonian $\mathbf{H}_0 = T + U(\mathbf{r})$ that describes a simpler physical system outside the scattering region:

$$\mathbf{H}_0\psi_{\text{in}}(\mathbf{r}) = E\psi_{\text{in}}(\mathbf{r}). \quad (2.28)$$

Often, one sets $U(\mathbf{r}) = 0$ and the incident waves are just plane waves. When long-range forces are present, like in Coulomb scattering [Mes64], this choice is poor and $U(\mathbf{r})$ should account for the interaction potential. The scattering potential $W(\mathbf{r})$ is given by the difference of the full Hamiltonian and the modified one: $W(\mathbf{r}) = \mathbf{H} - \mathbf{H}_0 = V(\mathbf{r}) - U(\mathbf{r})$. The Schrödinger equation we wish to solve is given by $[E - \mathbf{H}]\psi(\mathbf{r}) = 0$. Hence,

$$[E - \mathbf{H}_0 - W(\mathbf{r})][\psi_{\text{in}}(\mathbf{r}) + \psi_{\text{sc}}(\mathbf{r})] = 0. \quad (2.29)$$

Rearranging the terms in the last equation and using $[E - \mathbf{H}_0]\psi_{\text{in}}(\mathbf{r}) = 0$ and $\mathbf{H} = \mathbf{H}_0 + W(\mathbf{r})$ we get

$$[E - \mathbf{H}]\psi_{\text{sc}}(\mathbf{r}) = W(\mathbf{r})\psi_{\text{in}}(\mathbf{r}). \quad (2.30)$$

The scattering wave function $\psi_{\text{sc}}(\mathbf{r})$ is the solution to the inhomogeneous Schrödinger equation of the full Hamiltonian \mathbf{H} , where the inhomogeneity is given by $W(\mathbf{r})\psi_{\text{in}}(\mathbf{r})$. Defining this inhomogeneity as the *source term*

$$\sigma(\mathbf{r}) := W(\mathbf{r})\psi_{\text{in}}(\mathbf{r}) \quad (2.31)$$

suggests the following physical interpretation: The incoming wave $\psi_{\text{in}}(\mathbf{r})$, via the perturbation $W(\mathbf{r})$, feeds particles into the scattering wave $\psi_{\text{sc}}(\mathbf{r})$ that is governed by the Hamiltonian \mathbf{H} . Inhomogeneous partial differential equations are not uncommon in physics. The heat equation and Maxwell's equations are good examples for the introduction of sources. For these systems an adequate mathematical framework in the form of Green functions is available. In a similar spirit, we introduce the energy-dependent Green function $G(\mathbf{r}, \mathbf{r}'; E)$ for the Hamiltonian \mathbf{H} defined via [Eco83]

$$[E - \mathbf{H}_0 - W(\mathbf{r})]G(\mathbf{r}, \mathbf{r}'; E) = \delta(\mathbf{r} - \mathbf{r}'). \quad (2.32)$$

Now the solution to equation (2.30) is given by a convolution integral comprising the source wave-function and the Green function

$$\psi_{\text{sc}}(\mathbf{r}) = \int d^3r' G(\mathbf{r}, \mathbf{r}'; E)\sigma(\mathbf{r}'). \quad (2.33)$$

In general, the Green function is not uniquely defined. Depending on our choice of the Green function we obtain different wave functions $\psi_{\text{sc}}(\mathbf{r})$. However, any two solutions $\psi_{\text{sc}}(\mathbf{r})$ differ only by an eigenfunction $\psi_{\text{hom}}(\mathbf{r})$ of \mathbf{H} : $\mathbf{H}\psi_{\text{hom}}(\mathbf{r}) = E\psi_{\text{hom}}(\mathbf{r})$. The ambiguity in $\psi_{\text{sc}}(\mathbf{r})$ is resolved by the demand that $G(\mathbf{r}, \mathbf{r}'; E)$ presents a retarded solution characterized by an outgoing-wave behavior. Here, we quote one possible definition of the energy-dependent Green function in terms of the propagator:

$$G(\mathbf{r}, \mathbf{r}'; E) = -\frac{i}{\hbar} \lim_{\eta \rightarrow 0^+} \int_0^\infty dT e^{-iET/\hbar - \eta t/\hbar} K(\mathbf{r}, T | \mathbf{r}', 0). \quad (2.34)$$

We will further discuss the correct choice of the Green function and the related appearance of the limiting procedure involving η in Chapter 3. The next step is the definition of a current associated with the scattering wave. Using the Schrödinger equation for the scattering wave

$$\left[\frac{(\mathbf{p} - e\mathbf{A}(\mathbf{r})/c)^2}{2m} + V(\mathbf{r}) \right] \psi_{\text{sc}}(\mathbf{r}, t) = i\hbar \frac{\partial}{\partial t} \psi_{\text{sc}}(\mathbf{r}, t), \quad (2.35)$$

we define the current density in the usual fashion by

$$\mathbf{j}(\mathbf{r}) = \frac{\hbar}{m} \Im[\psi_{\text{sc}}(\mathbf{r})^* \nabla \psi_{\text{sc}}(\mathbf{r})] - \frac{e\mathbf{A}(\mathbf{r})}{m} |\psi_{\text{sc}}(\mathbf{r})|^2. \quad (2.36)$$

As before, $\mathbf{A}(\mathbf{r})$ denotes the vector potential. The inhomogeneous Schrödinger equation (2.30) gives rise to a modified equation of continuity and instead of $\nabla \cdot \mathbf{j}(\mathbf{r}) = 0$, valid in the absence of sources, we now have

$$\nabla \cdot \mathbf{j}(\mathbf{r}) = -\frac{2}{\hbar} \Im[\sigma(\mathbf{r})^* \psi_{\text{sc}}(\mathbf{r})]. \quad (2.37)$$

Thus, the inhomogeneity $\sigma(\mathbf{r})$ acts as a source for the particle current $\mathbf{j}(\mathbf{r})$ and the current is conserved outside the source region. By integration over a surface enclosing the source volume and inserting equation (2.33) for the scattering wave, we obtain a bilinear expression for the total particle current $J(E)$ (or total scattering rate):

$$J(E) = -\frac{2}{\hbar} \Im \left[\int d^3r \int d^3r' \sigma(\mathbf{r})^* G(\mathbf{r}, \mathbf{r}'; E) \sigma(\mathbf{r}') \right]. \quad (2.38)$$

We may note that point sources $\sigma(\mathbf{r}) = C\delta(\mathbf{r} - \mathbf{r}')$ considerably simplify the calculation of the scattering currents. In this case C denotes the source strength, since the source distribution is not normalizable. We obtain for the scattering wave

$$\psi_{\text{sc}}(\mathbf{r}) = C G(\mathbf{r}, \mathbf{r}'; E), \quad (2.39)$$

and the total current becomes

$$J(E) = -\frac{2|C|^2}{\hbar} \lim_{r \rightarrow 0} \Im \{G(\mathbf{r}, \mathbf{o}; E)\}. \quad (2.40)$$

In our discussion of double-slit experiments we used implicitly point sources, since we did not specify a different initial source distribution.

2.2.2 A sum rule for the total current

For non point-like sources we will construct an analogous expression to the optical theorem in conventional scattering theory. Exploiting the time-reversal symmetry relation for the propagator

$$K(\mathbf{r}, t|\mathbf{r}', 0)^\dagger = K(\mathbf{r}, -t|\mathbf{r}', 0), \quad (2.41)$$

the total current $J(E)$ in equation (2.38) can be rewritten using equation (2.34) as

$$J(E) = \frac{1}{\hbar^2} \int_{-\infty}^{\infty} dt e^{iEt/\hbar} \int d^3\mathbf{r} \int d^3\mathbf{r}' \sigma(\mathbf{r})^* K(\mathbf{r}, t|\mathbf{r}', 0) \sigma(\mathbf{r}'). \quad (2.42)$$

Integration with respect to the energy E together with the initial condition $K(\mathbf{r}, 0|\mathbf{r}', 0) = \delta(\mathbf{r} - \mathbf{r}')$ leads to the following sum rule for the total current:

$$\int_{-\infty}^{\infty} dE J(E) = \frac{2\pi}{\hbar} \int d^3\mathbf{r} \int d^3\mathbf{r}' \sigma(\mathbf{r})^* K(\mathbf{r}, 0|\mathbf{r}', 0) \sigma(\mathbf{r}') = \frac{2\pi}{\hbar} \int d^3\mathbf{r} |\sigma(\mathbf{r})|^2. \quad (2.43)$$

This sum-rule is very useful for a cross check of calculations involving extended sources. It also determines the asymptotical behavior of $J(E)$, since the finite value for the integral over the total current with respect to the energy demands a vanishing total current for $E \rightarrow \pm\infty$.

2.3 Feynman's path integral

An alternative description of the propagator rests on a lattice-definition of the Feynman path integral. We sketch briefly the connection between the two formulations. Applying Trotter's formula for the self-adjoint operators \mathbf{A}, \mathbf{B}

$$e^{iT(\mathbf{A}+\mathbf{B})} = \lim_{N \rightarrow \infty} [e^{i\mathbf{A}T/N} e^{i\mathbf{B}T/N}]^N \quad (2.44)$$

to the time evolution operator of the Hamiltonian $\mathbf{H} = \mathbf{H}_0 + V(\mathbf{r})$, where \mathbf{H}_0 denotes the free part, we obtain

$$\begin{aligned} U_{\mathbf{H}}(T) &= \exp\left(\frac{iT[\mathbf{H}_0 + V(\mathbf{r})]}{\hbar}\right) = \lim_{N \rightarrow \infty} \left[\exp\left(\frac{iT\mathbf{H}_0}{\hbar N}\right) \exp\left(\frac{iTV(\mathbf{r})}{\hbar N}\right) \right]^N \\ &= \lim_{N \rightarrow \infty, \epsilon \rightarrow 0} \prod_{j=0}^{N-1} \exp\left(\frac{i\epsilon\mathbf{H}_0}{\hbar}\right) \exp\left(\frac{i\epsilon V(\mathbf{r})}{\hbar}\right). \end{aligned} \quad (2.45)$$

Here, ϵ denotes $T/N \equiv \epsilon$. As stated in equation (2.5) the propagator is merely the position space representation of the time evolution operator: $K(\mathbf{r}, T|\mathbf{r}', 0) \equiv \langle \mathbf{r}' | U_{\mathbf{H}}(T) | \mathbf{r} \rangle$. Using

the composition law for the propagator N -times gives the following relation

$$\begin{aligned} K(\mathbf{r}, T | \mathbf{r}', 0) &= \int d\mathbf{r}_1 \cdots \int d\mathbf{r}_{N-1} \langle \mathbf{r}_N = \mathbf{r}' | U_{\mathbf{H}}(\epsilon) | \mathbf{r}_{N-1} \rangle \langle \mathbf{r}_{N-1} | U_{\mathbf{H}}(\epsilon) | \mathbf{r}_{N-2} \rangle \cdots \\ &\quad \cdots \langle \mathbf{r}_2 | U_{\mathbf{H}}(\epsilon) | \mathbf{r}_1 \rangle \langle \mathbf{r}_1 | U_{\mathbf{H}}(\epsilon) | \mathbf{r}_0 = \mathbf{r} \rangle \\ &= \int d\mathbf{r}_1 \cdots \int d\mathbf{r}_{N-1} \prod_{j=0}^{N-1} \langle \mathbf{r}_{j+1} | U_{\mathbf{H}}(\epsilon) | \mathbf{r}_j \rangle. \end{aligned} \quad (2.46)$$

Together with equation (2.45) the propagator takes the form

$$K(\mathbf{r}, T | \mathbf{r}', 0) = \lim_{N \rightarrow \infty} \int d\mathbf{r}_1 \cdots \int d\mathbf{r}_{N-1} \prod_{j=0}^{N-1} K_{\text{free}}(\mathbf{r}_{j+1}, \epsilon | \mathbf{r}_j, 0) e^{-i\epsilon V(\mathbf{r}_j)/\hbar} \quad (2.47)$$

$$= \lim_{N \rightarrow \infty} \int d\mathbf{r}_1 \cdots \int d\mathbf{r}_{N-1} \left(\frac{m}{2\pi i \hbar \epsilon} \right)^{N/2} e^{\sum_{j=0}^{N-1} \frac{im}{2\hbar\epsilon} (\mathbf{r}_{j+1} - \mathbf{r}_j)^2 - i\epsilon V(\mathbf{r}_j)/\hbar} \quad (2.48)$$

$$\equiv \int_{\mathbf{r}(t)=\mathbf{r}}^{\mathbf{r}(t')=\mathbf{r}'} \mathcal{D}\mathbf{r}(t) \exp \left[\frac{i}{\hbar} \int_t^{t'} d\tilde{t} \left(\frac{m}{2} \dot{\mathbf{r}}^2 - V(\mathbf{r}) \right) \right]. \quad (2.49)$$

In the last line we introduced an integral representation motivated by

$$\int_t^{t+\epsilon} d\tilde{t} \left(\frac{m}{2} \dot{\mathbf{r}}^2 - V(\mathbf{r}) \right) \approx \epsilon \left(\frac{m}{2} \left(\frac{\mathbf{r}(t+\epsilon) - \mathbf{r}(t)}{\epsilon} \right)^2 - V(\mathbf{r}(t)) \right). \quad (2.50)$$

The “measure” $\mathcal{D}\mathbf{r}(t)$ is only a symbolic expression for the process outlined above. The “direct” evaluation of path integrals using this time-slicing technique is possible, see i.e. [Kle90]. The inclusion of the vector potential \mathbf{A} is also possible, but not completely trivial, since only slicing at the midpoints $\frac{1}{2}(\mathbf{r}_{j+1} + \mathbf{r}_j)$ of the potential leads to correct results [Kle90]. For our purposes, the lattice-formulation gives no direct benefits. Instead we employ the basic definition of the propagator in terms of the time-evolution operator. From a conceptual point of view, especially for the interpretation of interferences, the path-integral approach is particularly well suited. The main ingredient of the path integral is the classical action

$$S_{cl}(\mathbf{r}, t; \mathbf{r}', t') = \int_t^{t'} d\tilde{t} \left[\frac{m}{2} \dot{\mathbf{r}}^2 - V(\mathbf{r}) \right] \quad (2.51)$$

which played an important role for the interpretation of the field slit experiment. The action principle provides a bridge for connecting (and contrasting) quantum and classical dynamics [DR01]. In a very symbolic way we can interpret the propagator as a sum over all trajectories connecting \mathbf{r} with \mathbf{r}'

$$K(\mathbf{r}, t | \mathbf{r}', t') \sim \sum_{\text{all trajectories}} \exp \left[\frac{i}{\hbar} S_{cl}(\mathbf{r}, t; \mathbf{r}', t') \right]. \quad (2.52)$$

Often a further simplification is achieved by only considering classically allowed trajectories for a given energy

$$K(\mathbf{r}, t | \mathbf{r}', t') \sim \sum_{\text{stationary trajectories}} \exp \left[\frac{i}{\hbar} S_{cl}(\mathbf{r}, t; \mathbf{r}', t') \right]. \quad (2.53)$$

A more rigorous form of these relations will be given in the next chapter by considering the analytic properties of the propagator in the complex time plane.

Another way to obtain the Green function is the solution of the underlying partial differential equation (2.7). We may note that the approximation of integrals (numerical and analytically) is much more useful and practicable than a numerical evaluation of a higher-dimensional partial differential equation.

Chapter 3

Properties of Green functions

The energy-dependent Green function is one of the cornerstones for the theory of stationary quantum sources. We already noted that commonly the energy of a physical process is fixed and not the observation time (which should be addressed with the propagator). A thorough understanding of the mathematical properties of the energy-dependent Green function is of great value for the interpretation of the behavior of physical systems. By giving a number of examples we want to demonstrate and immediately apply useful mathematical theorems and techniques.

3.1 The energy-dependent Green function

In equation (2.34) we defined the retarded energy-dependent Green function as the Laplace transform of the time evolution operator:

$$G(\mathbf{r}, \mathbf{r}'; E) = -\frac{i}{\hbar} \lim_{\eta \rightarrow 0_+} \int_0^\infty dt \langle \mathbf{r} | U(t, t_0) | \mathbf{r}' \rangle e^{iEt/\hbar - \eta t/\hbar}. \quad (3.1)$$

For time-independent Hamiltonians, the time evolution operator is given by $U(t - t') = \exp(i\mathbf{H}(t - t')/\hbar)$. Using this form, we can integrate equation (3.1) and obtain

$$G(\mathbf{r}, \mathbf{r}'; E) = \lim_{\eta \rightarrow 0_+} \left\langle \mathbf{r} \left| \frac{1}{E - \mathbf{H} + i\eta} \right| \mathbf{r}' \right\rangle. \quad (3.2)$$

Instead of evaluating the kernel in position space, we can choose a representation for the resolvent operator $1/(E - \mathbf{H} + i\eta)$ that is more suitable for the Hamiltonian under consideration.

Example 2 (Propagator in momentum space) We want to calculate the energy dependent Green function for the one-dimensional motion in the presence of a linear force field. The Hamiltonian is given by

$$\mathbf{H}_{\text{field}} = \frac{p^2}{2m} - Fz. \quad (3.3)$$

In momentum space, the Schrödinger equation reads

$$\left[\frac{p^2}{2m} - i\hbar F \frac{d}{dp} - E \right] \phi_E(p) = 0. \quad (3.4)$$

This first order differential equation has the solution

$$\phi_E(p) = \frac{1}{\sqrt{2\pi\hbar F}} \exp\left(\frac{i}{\hbar F}(Ep - p^3/(6m))\right), \quad (3.5)$$

which is normalized by the relation

$$\int_{-\infty}^{\infty} dp \phi_E(p) \phi_{E'}(p) = \delta(E' - E). \quad (3.6)$$

The energy-dependent Green function is given by

$$\begin{aligned} G_{\text{field}}(p, p'; E) &= \Theta(p - p') \int_{-\infty}^{\infty} dE' \frac{\phi_{E'}(p) \phi_{E'}^*(p')}{E - E' + i\eta} \\ &= -2\pi i \phi_E(p) \phi_E^*(p') \Theta(p - p') \\ &= -\frac{i}{F\hbar} \exp\left\{ \frac{i}{\hbar} \left(\frac{(p^3 - p'^3)}{6Fm} + \frac{E}{F}(p - p') \right) \right\} \Theta(p - p'). \end{aligned} \quad (3.7)$$

The step-function $\Theta(p' - p)$ enforces the outgoing-wave boundary condition. In the second line we used the following theorem:

Theorem 1 (Cauchy's integral) *The integral around a closed path of integration of a function $f(z)$ holomorphic in the included domain is given by*

$$\oint dw \frac{f(w)}{w - z} = 2\pi i f(z), \quad (3.8)$$

where the path of integration encloses the singularity at $w = z$ and is mathematically positive oriented.

Of course we can use two Fourier transforms to go back to position space:

$$G_{\text{field}}(z, z'; E) = \frac{1}{2\pi\hbar} \int_{-\infty}^{\infty} dp \int_{-\infty}^{\infty} dp' e^{ipz/\hbar} G_{\text{field}}(p, p'; E) e^{-ip'z'/\hbar}. \quad (3.9)$$

Substituting $p = F(u + v)/2$, and $p' = F(u - v)/2$ we carry out one Gaussian integration over u ; the remaining v -integration becomes:

$$G_{\text{field}}(z, z'; E) = -\frac{i}{\hbar} \int_0^{\infty} dv \sqrt{\frac{m}{2\pi i \hbar v}} \exp\left(\frac{iEv}{\hbar} + \frac{im(z - z')^2}{2\hbar v} + \frac{iFv}{2\hbar}(z + z') - \frac{iF^2v^3}{24m\hbar}\right). \quad (3.10)$$

By replacing v with t we precisely recover the form of the time-dependent kernel in position space given in equation (2.15). The energy Green function can be evaluated with the integrals tabulated in Appendix B and reads

$$G_{\text{field}}(z, z'; E) = -4\pi\beta^2 F \text{Ci}(\alpha_+) \text{Ai}(\alpha_-), \quad (3.11)$$

where $\beta = (m/(4\hbar^2 F^2))^{1/3}$, $\alpha_{\pm} = -\beta(2E + F(z - z') \pm F|z - z'|)$. Also $\text{Ci}(z)$ denotes the complex Airy function $\text{Ci}(z) = \text{Bi}(z) + i\text{Ai}(z)$. We see that the energy-dependent Green function in momentum space is considerably simpler than in position space.

A huge compilation of known time-dependent propagators in different dimensions is given by Grosche [GS98]. The knowledge of time-dependent propagators in lower dimensions can be useful to construct propagators in higher dimensions. If the Hamiltonian of a multidimensional problem can be written as the sum of lower dimensional Hamiltonians, we can form the product of the lower dimensional propagators and thus obtain the propagator for the full problem.

Example 3 (Composition of time-dependent propagators) The three-dimensional propagator for the free-particle with the Hamiltonian

$$\mathbf{H} = \sum_{i=1}^3 \frac{p_i^2}{2m} \quad (3.12)$$

can be written as a product of the one-dimensional propagators

$$K_{\text{free}}^{(3D)}(\mathbf{r}, t; \mathbf{r}'; t') = \prod_{i=1}^3 K_{\text{free}}^{(1D)}(x_i, t; x'_i; t'). \quad (3.13)$$

A non-trivial example is the propagator for the uniform field in one direction and free motion in the other two directions. We can decompose the propagator into

$$\begin{aligned} K_{\text{field}}^{(3D)}(\mathbf{r}, t; \mathbf{r}'; t') &= K_{\text{free}}^{(1D)}(x, t; x'; t') K_{\text{free}}^{(1D)}(y, t; y'; t') K_{\text{field}}^{(1D)}(z, t; z'; t') \\ &= K_{\text{free}}^{(1D)}(z, t; z'; t') \exp\left(\frac{iF(t-t')}{2\hbar}(z+z') - \frac{iF^2(t-t')^3}{24m\hbar}\right) \times \\ &\quad \times \prod_{i=1}^2 K_{\text{free}}^{(1D)}(x_i, t; x'_i; t'). \end{aligned} \quad (3.14)$$

Unfortunately the simple multiplication method for time-dependent kernels of separable systems does not work for the corresponding energy-dependent Green functions. However, at least formally we can connect the respective energy Green functions by a complex

convolution theorem. In the preceding chapter we already used the convolution theorem for the product of time-dependent propagators. Denoting the Laplace transform by \mathcal{L}

$$\mathcal{L}[f_1(t); s] = \int_0^\infty dt e^{-st} f_1(t) = g_1(s), \quad \mathcal{L}[f_2(t); s] = \int_0^\infty dt e^{-st} f_2(t) = g_2(s),$$

we have the following theorem.

Theorem 2 (Complex convolution) *The Laplace transform of the product of two functions is given by*

$$\mathcal{L}[f_1(t)f_2(t); s] = \frac{1}{2\pi i} \int_{c-i\infty}^{c+i\infty} du g_1(u)g_2(s-u), \quad (3.15)$$

or, if $c = 0$

$$\mathcal{L}[f_1(t)f_2(t); s] = \frac{1}{2\pi} \int_{-\infty}^{\infty} du g_1(iu)g_2(s-iu). \quad (3.16)$$

Example 4 (Complex Convolution) Before we can use this theorem we have to adapt it to the case of energy-dependent Green functions. Writing the Laplace transform of the kernel as

$$i\hbar G(\mathbf{r}, \mathbf{r}'; E) = \int_0^\infty dt e^{-st} K(\mathbf{r}, t|\mathbf{r}', 0) \quad (3.17)$$

with $s = -iEt/\hbar$, we can apply the convolution theorem to the product of two time-dependent kernels and obtain

$$\begin{aligned} G_3(\mathbf{r}, \mathbf{r}'; E) &= \frac{1}{i\hbar} \int_0^\infty dt e^{-st} K_1(\mathbf{r}, t|\mathbf{r}', 0) K_2(\mathbf{r}, t|\mathbf{r}', 0) \\ &= \frac{\hbar}{2\pi} \int_{-i\infty}^{i\infty} du G_1(\mathbf{r}, \mathbf{r}'; i\hbar u) G_2(\mathbf{r}, \mathbf{r}'; i\hbar(s-u)) \\ &= \frac{1}{2\pi i} \int_{-\infty}^{\infty} dE' G_1(\mathbf{r}, \mathbf{r}'; E') G_2(\mathbf{r}, \mathbf{r}'; E-E'). \end{aligned} \quad (3.18)$$

Due to the complicated structure of the energy-dependent Green-function it is often not possible to exploit this relation. An actual application is given in Section 4.4.

We have already used an expansion in terms of the eigenfunctions of the Hamiltonian to calculate the energy-Green function in a linear field in momentum space. In Example 2 we encountered a continuous energy spectrum of the Hamiltonian. If the spectrum of the Hamiltonian \mathbf{H} is discrete, we can insert a complete set of orthonormal energy eigenfunctions $|\phi_n\rangle$ in equation (3.2) and obtain

$$G = \lim_{\eta \rightarrow 0} \frac{1}{E - \mathbf{H} + i\eta} = \lim_{\eta \rightarrow 0} \sum_n \frac{|\phi_n\rangle\langle\phi_n|}{E - E_n + i\eta}. \quad (3.19)$$

This expression can be used to calculate the energy-dependent Green function of the harmonic oscillator.

Example 5 (Discrete energy spectrum) For the harmonic oscillator it is very convenient to use the Bargmann representation [Bar61, Bar67]. The creation and annihilation operators in Bargmann space are given by

$$\begin{aligned} Z_j f(z) &= z_j f(z), \\ D_j f(z) &= \frac{\partial}{\partial z_j} f(z). \end{aligned}$$

Bargmann introduces a suitable Hilbert space B of functions for these operators and shows that it yields the correct adjoint properties of the operators Z_j, D_j . The elements of this Hilbert space B (often called Bargmann space) are complex valued analytic functions of complex variables z . The Hamiltonian of the harmonic oscillator $\mathbf{H} = \hbar\omega(a^\dagger a + \frac{1}{2})$ becomes in Bargmann space

$$\mathbf{H} = \hbar\omega(z\partial_z + \frac{1}{2}), \quad (3.20)$$

with eigenstates $\mathbf{H} (z|n) = \hbar\omega[n + 1/2](z|n)$, $(z|n) = z^n/(n!)$. Using this result we get

$$(z|G(E)|z') = \sum_{n=0}^{\infty} \frac{(z|n)(n|z')}{E - \hbar\omega(n + 1/2)} = -\frac{1}{\hbar\omega} \sum_{n=0}^{\infty} \frac{[z\bar{z}']^n}{n!} \frac{1}{n + 1/2 - E/(\hbar\omega)}. \quad (3.21)$$

The last equation can be expressed in terms of the incomplete gamma function γ^* (see [AS65], equation (6.5.29))

$$\gamma^*(a, \zeta) = \frac{1}{\Gamma(a)} \sum_{n=0}^{\infty} \frac{(-\zeta)^n}{(a+n)n!}$$

and the closed form of the energy-dependent Green function reads

$$(z|G(E)|z') = -\frac{1}{\hbar\omega} \Gamma(1/2 - E/(\hbar\omega)) \gamma^*(1/2 - E/\hbar\omega, -z\bar{z}').$$

Again, we can transform this propagator back to coordinate space [Kra00].

3.2 Connection to Fermi's golden rule

In the definition of the energy-dependent Green function in equation (3.1) we introduced a small positive parameter η that ensures the convergence of the integral for $t \rightarrow \infty$. This is necessary, because the integral kernel is not unique in the continuous spectrum of a Hamiltonian. From a physical point of view, this ambiguity of the solution set is required to accommodate different boundary conditions for the resulting Green function. For the following discussion we are interested in outgoing matter waves that enforce the use of

the retarded energy Green function [Eco83]. To establish an alternative expression for the total current, we employ Cauchy's principal value for the integration of the kernel [HS52]:

$$G(\mathbf{r}, \mathbf{r}'; E) = \lim_{\eta \rightarrow 0^+} \left\langle \mathbf{r} \left| \frac{1}{E - \mathbf{H} + i\eta} \right| \mathbf{r}' \right\rangle = \left\langle \mathbf{r} \left| \text{PP} \left(\frac{1}{E - \mathbf{H}} \right) - i\pi\delta(E - \mathbf{H}) \right| \mathbf{r}' \right\rangle. \quad (3.22)$$

The principal value integral (denoted by PP) is real-valued due to the hermiticity of \mathbf{H} and we obtain the total current in the form

$$J(E) = -\frac{2}{\hbar} \Im [\langle \sigma | G | \sigma \rangle] = \frac{2\pi}{\hbar} \langle \sigma | \delta(E - \mathbf{H}) | \sigma \rangle. \quad (3.23)$$

The previously stated sum rule (see equation (2.43)) is regained by integrating the last expression for the total current with respect to the energy

$$\int_{-\infty}^{\infty} dE J(E) = \frac{2\pi}{\hbar} \langle \sigma | \sigma \rangle = \frac{2\pi}{\hbar} \int d^3r |\sigma(\mathbf{r})|^2. \quad (3.24)$$

This relation holds provided that the source wave function $\sigma(\mathbf{r})$ can be normalized. With the help of equation (3.23) we can put forward another interpretation of the total current $J(E)$. By employing a complete orthonormal set of eigenfunctions $|\psi_{\mathfrak{f}}\rangle$ of the Hamiltonian \mathbf{H} , we can rewrite $\delta(E - \mathbf{H})|\psi_{\mathfrak{f}}\rangle$ as $\delta(E - E_{\mathfrak{f}})|\psi_{\mathfrak{f}}\rangle$. Using the interaction operator W introduced in Section 2.2.1, we replace the particle source σ by the perturbed initial state: $|\sigma\rangle = W|\psi_{\text{in}}\rangle$. Inserting these relations into equation (3.23) we obtain the following formal summation:

$$J(E) = \frac{2\pi}{\hbar} \sum_{\mathfrak{f}} \delta(E - E_{\mathfrak{f}}) |\langle \psi_{\mathfrak{f}} | W | \psi_{\text{in}} \rangle|^2. \quad (3.25)$$

This form is actually a variant of Fermi's golden rule. However, some remarks of caution are required. For a continuum of final states the sum is replaced by an integration. The final states $\psi_{\mathfrak{f}}(\mathbf{r})$ are in general not readily available for deriving an analytic expression of the matrix-element $|\langle \psi_{\mathfrak{f}} | W | \psi_{\text{in}} \rangle|$. Also $\psi_{\mathfrak{f}}(\mathbf{r})$ is not the scattering wave function, discussed in Section 2.2.1. Therefore, even after an evaluation of the sum and the matrix elements no expression is available for the emerging scattering wave function $\psi_{\text{sc}}(\mathbf{r})$. But the scattering wave is needed to obtain the spatial current distribution $\mathbf{j}(\mathbf{r})$. Thus, the use of Fermi's golden rule is limited to situations where we are only interested in the total scattering rate.

From a more fundamental point of view equation (3.25) motivates some connections to other fields of physics. In Chapter 7 we demonstrate the close relation of the just presented formulation to the theory of Franck-Condon factors as discussed by Heller [Hel78].

Another noteworthy consequence of equations (2.40) and (3.25) emerges in the limit of point-like sources, $\sigma(\mathbf{r}) = C\delta(\mathbf{r} - \mathbf{R})$. We then find [BRK97]:

$$J(E) = -\frac{2}{\hbar} |C|^2 \Im [G(\mathbf{R}, \mathbf{R}; E)] = \frac{2\pi}{\hbar} |C|^2 n(\mathbf{R}; E), \quad (3.26)$$

where

$$n(\mathbf{R}; E) = \sum_{\mathfrak{f}} \delta(E - E_{\mathfrak{f}}) |\psi_{\mathfrak{f}}(\mathbf{R})|^2 \quad (3.27)$$

is the local density of states of \mathbf{H} at the source position \mathbf{R} . Equation (3.26) forms the theoretical basis of the Tersoff–Hamann description of scanning tunneling microscopy [TH83, BRK97]. In the next chapter we will use equation (3.26) for the calculation of the electronic density of states. The density of states is of considerable interest for solid state physics, since it influences electrical, magnetical and thermal properties of many materials. Chapter 5 contains a detailed analysis of the density of states in crossed electric and magnetic fields in a two-dimensional system and its implication for the electrical conductivity.

3.3 The general quadratic Hamiltonian

The calculation of energy-dependent Green functions remains a difficult task, despite the different available methods. Therefore it is not too surprising, that the number of known energy-dependent Green functions is quite small. Analytic expressions in three-dimensions exist for the free field environment, the harmonic oscillator [BV71], the Coulomb potential [HP64], the static uniform electric field [DS76, LLF90, BBG⁺98], the static uniform magnetic field [BV71, Gou72, DMM75], and combined parallel static electric and magnetic fields [Fab91, Loh92, KBK01]. Five of these potentials are quadratic in the momentum and position operators, but the general energy-dependent Green function for arbitrary quadratic Hamiltonians is not known analytically. Fortunately at least the time-dependent propagator is available for a general quadratic Hamiltonian (see [GS98], 6.2.1 and references therein). A systematic classification of the time-dependent solutions of the Schrödinger equation for quadratic Hamiltonians is given in [MW80].

The approach we pursue for the calculation of the kernel of an quadratic Hamiltonian makes use of the connection between canonical transformations and their representation in Bargmann space. We already discussed the harmonic oscillator in Bargmann space in Example 5. How can we relate the propagator to a canonical transformation? The time-dependent propagator in a given representation is just the matrix element of the time-evolution operator as stated in equation (3.1). For quadratic Hamiltonians, we have the useful property that the time evolution of the canonical operators \mathbf{x}, \mathbf{p} can be viewed as the unitary representation of a linear canonical transformation [MQ71]. To see this, we evaluate the time-evolution of an operator $\mathbf{G}^{(H)}$ in the Heisenberg picture (we will denote operators in the Heisenberg picture by (H) in this section)

$$\begin{aligned} \mathbf{G}^{(H)}(t) &= \mathbf{U}^\dagger(t) \circ \mathbf{G}^{(H)}(0) \circ \mathbf{U}(t) \\ &= \mathbf{G}^{(H)}(0) + (it/\hbar) [\mathbf{H}, \mathbf{G}^{(H)}(0)] + (1/2!)(it/\hbar)^2 [\mathbf{H}, [\mathbf{H}, \mathbf{G}^{(H)}(0)]] + \dots, \end{aligned} \quad (3.28)$$

where we used the Baker-Hausdorff lemma (see i.e. [Mer69], 8.105). Since we are interested in the time evolution of $\mathbf{x}^{(H)}(t)$ and $\mathbf{p}^{(H)}(t)$, we note that for a quadratic Hamiltonian all commutators $[\mathbf{H}, \mathbf{x}^{(H)}(0)]$ and $[\mathbf{H}, \mathbf{p}^{(H)}(0)]$ will just evaluate to either a constant or a multiple of the operator itself. Therefore we can relate the time evolution of the operators $\mathbf{x}^{(H)}(t)$ and $\mathbf{p}^{(H)}(t)$ to a linear canonical transformation. This transformation reads in

block matrix notation

$$\begin{aligned}\mathbf{x}^{(H)}(t) &= \alpha \mathbf{x}^{(H)}(0) + \beta (-\mathbf{p}^{(H)}(0)) + \vec{a}', \\ -\mathbf{p}^{(H)}(t) &= \wp \mathbf{x}^{(H)}(0) + \delta (-\mathbf{p}^{(H)}(0)) + \vec{a}'',\end{aligned}\tag{3.29}$$

with four matrices $\alpha, \beta, \wp, \delta$ of dimension $D \times D$, depending on the number of dimensions D in the system. Combining all $D \times D$ -dimensional block matrices and the D -dimensional shifts into a single matrix, we construct a $(2D + 1) \times (2D + 1)$ matrix \hat{g} :

$$\begin{pmatrix} \mathbf{x}^{(H)}(t) \\ -\mathbf{p}^{(H)}(t) \\ \mathbf{1} \end{pmatrix} = \mathbf{U}^\dagger(t) \circ \begin{pmatrix} \mathbf{x}^{(H)}(0) \\ -\mathbf{p}^{(H)}(0) \\ \mathbf{1} \end{pmatrix} \circ \mathbf{U}(t) = \hat{g}(t) \begin{pmatrix} \mathbf{x}^{(H)}(0) \\ -\mathbf{p}^{(H)}(0) \\ \mathbf{1} \end{pmatrix},\tag{3.30}$$

where

$$\hat{g}(t) = \left(\begin{array}{cc|c} \alpha & \beta & \vec{a}' \\ \wp & \delta & \vec{a}'' \\ \hline 0 & 0 & 1 \end{array} \right).$$

For propagators in three dimensions we have to determine the 7×7 -matrix \hat{g} . The evaluation of \hat{g} for a given Hamiltonian is done by the exponentiation of an auxiliary matrix \hat{k} that contains the commutator of \mathbf{H} with \mathbf{x} and \mathbf{p} :

$$\left[\mathbf{H}, \begin{pmatrix} \mathbf{x}^{(H)}(0) \\ -\mathbf{p}^{(H)}(0) \\ \mathbf{1} \end{pmatrix} \right] = -i\hat{k} \begin{pmatrix} \mathbf{x}^{(H)}(0) \\ -\mathbf{p}^{(H)}(0) \\ \mathbf{1} \end{pmatrix}.\tag{3.31}$$

As a short calculation proves (see equation (A.3)), the matrix \hat{g} then becomes

$$\hat{g}(t) = \exp(\hat{k}t).$$

Since we used the Heisenberg picture for the time evolution of $\mathbf{x}^{(H)}(0)$ and $\mathbf{p}^{(H)}(0)$, we also solved the classical equations of motion. The general form of the time-dependent propagator is given by a transformation of the Bargmann kernel [Bar70] to Hilbert space, which is derived in detail in [Kra00]:

$$\begin{aligned}\langle \mathbf{r} | \mathbf{U}(\hat{g}(t)) | \mathbf{r}' \rangle &= \nu_g(t) \exp \left\{ -i\vec{\alpha}'' \cdot (\mathbf{r} - \vec{\alpha}') - \frac{1}{2} \vec{\alpha}'' \cdot \vec{\alpha}' - i\frac{1}{2} (\mathbf{r} - \vec{\alpha}') \delta \beta^{-1} (\mathbf{r} - \vec{\alpha}') \right. \\ &\quad \left. + i(\mathbf{r} - \vec{\alpha}') (\beta^{-1})^T \mathbf{r}' - i\frac{1}{2} \mathbf{r}' \beta^{-1} \delta \mathbf{r}' \right\}.\end{aligned}\tag{3.32}$$

Here, $\nu_g(t)$ is a factor independent of the coordinates \mathbf{r}, \mathbf{r}' that can be easily found by solving the first order differential equation

$$\left([i\hbar\partial_t - \mathbf{H}] \langle \mathbf{r} | \mathbf{U}(\hat{g}(t)) | \mathbf{r}' \rangle \right) \Big|_{\mathbf{r}=\mathbf{r}'=0} = 0.\tag{3.33}$$

An alternative method to obtain time-dependent kernels of quadratic Hamiltonians is given by Nieto in [Nie92]. Nieto uses the Moyal propagator for his phase-space approach.

3.4 Multipole sources

With the choice of the retarded Green function we enforce the boundary condition of outgoing matter waves. In many applications additional boundary conditions arise in the form of angular-momentum selection rules for the emitted wave. Examples are electrons emitted from a specific orbital state of an atom, or particle waves originating from a Bose-Einstein condensate with quantized vortices. Clearly, a completely isotropic point source $\sigma(\mathbf{r}) \sim \delta(\mathbf{r} - \mathbf{r}')$ can only describe a locally isotropic emission pattern with zero angular momentum. Motivated by the partial-wave expansion used in the case of conventional (localized) scattering potentials, we proceed with the introduction of a multipole source and a corresponding multipole Green function [Bra99, BKK02]. Let us start with a familiar problem from electrostatics. The potential ϕ of a point-charge of unit strength located at \mathbf{r}' is given by

$$\phi(\mathbf{r}) = \frac{-1}{|\mathbf{r} - \mathbf{r}'|}, \quad (3.34)$$

since this choice solves the Poisson equation for the charge distribution

$$\nabla'^2 \frac{1}{|\mathbf{r} - \mathbf{r}'|} = 4\pi\delta(\mathbf{r} - \mathbf{r}'). \quad (3.35)$$

The Green function for the potential of the point-charge reads

$$G(\mathbf{r}, \mathbf{r}') = -\frac{1}{4\pi|\mathbf{r} - \mathbf{r}'|}. \quad (3.36)$$

Similarly, multipole potentials are constructed with the well known spherical harmonics Y_{lm} , or the harmonic polynomials $K_{lm}(\mathbf{r}) = r^l Y_{lm}(\hat{r})$ [Hob31, MF53, Mül66]:

$$\Phi_{lm}(\mathbf{r}, \mathbf{r}') = \frac{Y_{lm}(\hat{\mathbf{e}}_{\mathbf{r}-\mathbf{r}'})}{|\mathbf{r} - \mathbf{r}'|^{l+1}} = \frac{K_{lm}(\mathbf{r} - \mathbf{r}')}{|\mathbf{r} - \mathbf{r}'|^{2l+1}}, \quad (3.37)$$

In electrostatics we would proceed with a multipole expansion of a general potential in terms of the Φ_{lm} . Here, we note that the spherical polynomials can also be used as a differential operator or spherical tensor gradient $K_{lm}(\nabla') = K_{lm}(\partial_{x'}, \partial_{y'}, \partial_{z'})$ that connects the Green function and the multipole potential [Bay78, Row78, WS83]:

$$K_{lm}(\nabla')G(\mathbf{r}, \mathbf{r}') = -\frac{(2l-1)!!}{4\pi}\Phi_{lm}(\mathbf{r}, \mathbf{r}'). \quad (3.38)$$

The spherical tensor gradient selects a potential with the desired multipole structure from $G(\mathbf{r}, \mathbf{r}')$. Since $\Delta G(\mathbf{r}, \mathbf{r}') = \delta(\mathbf{r} - \mathbf{r}')$ holds and ∇ commutes with $K_{lm}(\nabla')$ we formally obtain

$$\Delta\Phi_{lm}(\mathbf{r}, \mathbf{r}') = -\frac{4\pi}{(2l-1)!!}K_{lm}(\nabla')\delta(\mathbf{r} - \mathbf{r}'). \quad (3.39)$$

This relation serves as the basic definition of general multipole point-sources $\delta_{lm}(\mathbf{r} - \mathbf{r}')$ [Bay78, Row78]

$$\delta_{lm}(\mathbf{r} - \mathbf{r}') = K_{lm}(\nabla')\delta(\mathbf{r} - \mathbf{r}'), \quad (3.40)$$

and we denote the corresponding Green function that solves the inhomogeneous Schrödinger equation

$$[E - \mathbf{H}]G_{lm}(\mathbf{r}, \mathbf{r}'; E) = \delta_{lm}(\mathbf{r} - \mathbf{r}') \quad (3.41)$$

by $G_{lm}(\mathbf{r}, \mathbf{r}'; E)$. If \mathbf{H} and $K_{lm}(\nabla')$ commute, $G_{lm}(\mathbf{r}, \mathbf{r}'; E)$ is available from $G(\mathbf{r}, \mathbf{r}'; E)$ by the same differentiation process as before

$$G_{lm}(\mathbf{r}, \mathbf{r}'; E) = K_{lm}(\nabla')G(\mathbf{r}, \mathbf{r}'; E). \quad (3.42)$$

This suggests the following interpretation: G_{lm} is the Green function for a scattering process originating from a source with an internal angular momentum eigenstate given by (l, m) . However, in our example we used a specific Green function of the form $1/|\mathbf{r}-\mathbf{r}'|$. The closest analogue to this form in quantum mechanics is the energy-dependent Green function of the free particle $G^{(\text{free})}(\mathbf{r}, \mathbf{r}'; E)$ without any external potential given in equation (2.12). In fact the actual computation of $G_{lm}^{(\text{free})}(\mathbf{r}, \mathbf{r}'; E) = K_{lm}(\nabla')G^{(\text{free})}(\mathbf{r}, \mathbf{r}'; E)$ gives

$$G_{lm}^{(\text{free})}(\mathbf{r}, \mathbf{r}'; E) = -\frac{Mk^{l+1}}{2\pi\hbar^2}h_l^{(+)}(kR)Y_{lm}(\hat{R}), \quad (3.43)$$

where $E = \hbar^2k^2/2M$, $\mathbf{R} = \mathbf{r} - \mathbf{r}'$ and $h_l^{(+)}(u)$ denotes a spherical Hankel function [Mes64]. Of special interest is the behavior of the Green function in the vicinity of the source $\mathbf{r} \rightarrow \mathbf{r}'$. There, $G_{lm}^{(\text{free})}(\mathbf{r}, \mathbf{r}'; E)$ behaves asymptotically like:

$$G_{lm}(\mathbf{r}, \mathbf{r}'; E) \sim -\frac{M}{2\pi\hbar^2}(2l-1)!!\frac{Y_{lm}(\hat{\mathbf{e}}_{\mathbf{r}-\mathbf{r}'})}{|\mathbf{r}-\mathbf{r}'|^{l+1}}. \quad (3.44)$$

Bracher [Bra99] proved that this asymptotic form is a universal property of multipole Green functions, even in the presence of an external potential $U(\mathbf{r})$, provided only that the external potential $U(\mathbf{r})$ is analytic at the source location \mathbf{r}' . Therefore, the formal definition of the multipole Green function in terms of spherical tensor gradient K_{lm} acquires a clear physical interpretation: Even in a symmetry-breaking environment, the desired (l, m) orbital symmetry locally prevails and justifies the notion of a multipole source with definite angular momentum.

3.4.1 Currents from multipole quantum sources

The generalization of the expressions for the current from isotropic sources to multipole sources is straight forward. For spatially extended sources we define the normalized multipole source by

$$\sigma_{lm}(\mathbf{r}) = N_l K_{lm}(\nabla)\sigma(\mathbf{r}), \quad (3.45)$$

where N_l is determined by $\int d\mathbf{r}^3|\sigma_{lm}(\mathbf{r})|^2 = 1$. The scattering wave is then expressed as

$$\psi_{lm}(\mathbf{r}) = N_l \int d\mathbf{r}' G(\mathbf{r}, \mathbf{r}'; E)\sigma_{lm}(\mathbf{r}'). \quad (3.46)$$

Next, we insert $\psi_{lm}(\mathbf{r})$ and $\sigma_{lm}(\mathbf{r})$ instead of $\psi(\mathbf{r})$ and $\sigma(\mathbf{r})$ in the expressions for $J(E)$ given in equation (2.38) to extract the multipole current

$$J_{lm}(E) = -\frac{2}{\hbar} \Im [\langle \sigma_{lm} | G(\mathbf{r}, \mathbf{r}'; E) | \sigma_{lm} \rangle]. \quad (3.47)$$

A slight complication arises when we treat a superposition of several multipole sources with amplitudes λ_{lm} at a fixed location \mathbf{r}'

$$\sigma(\mathbf{r}) = \sum_{lm} \lambda_{lm} \delta_{lm}(\mathbf{r} - \mathbf{r}'). \quad (3.48)$$

Now the resulting scattering wave reads

$$\psi_{\text{sc}}(\mathbf{r}) = \sum_{lm} \lambda_{lm} G_{lm}(\mathbf{r}, \mathbf{r}'; E), \quad (3.49)$$

and the current density $\mathbf{j}(\mathbf{r})$ due to this wave function may be expressed as a bilinear form in the amplitudes λ_{lm}

$$\mathbf{j}(\mathbf{r}) = \sum_{lm} \sum_{l'm'} \lambda_{lm}^* \mathbf{j}_{lm,l'm'}(\mathbf{r}) \lambda_{l'm'}. \quad (3.50)$$

The elements of the hermitian current density matrix $\mathbf{j}_{lm,l'm'}(\mathbf{r})$ are given by

$$\mathbf{j}_{lm,l'm'}(\mathbf{r}) = -\frac{i\hbar}{2M} \{G_{lm}^*(\mathbf{r}, \mathbf{r}'; E) \nabla G_{l'm'}(\mathbf{r}, \mathbf{r}'; E) - G_{l'm'}(\mathbf{r}, \mathbf{r}'; E) \nabla G_{lm}^*(\mathbf{r}, \mathbf{r}'; E)\}. \quad (3.51)$$

Of particular interest is the total current $J(E)$ carried by the scattering wave in equation (3.49). Using equation (2.38) we integrate by parts to obtain an expression similar to equation (3.51)

$$J(E) = \sum_{lm} \sum_{l'm'} \lambda_{lm}^* J_{lm,l'm'}(E) \lambda_{l'm'}, \quad (3.52)$$

where the components of the hermitian total multipole current matrix $J_{lm,l'm'}(E)$ are extracted from the Green function $G(\mathbf{r}, \mathbf{r}'; E)$ through differentiation operations and a subsequent limiting procedure:

$$J_{lm,l'm'}(E) = \frac{i}{\hbar} \lim_{\mathbf{r} \rightarrow \mathbf{r}'} K_{lm}^*(\nabla) K_{l'm'}(\nabla') \{G(\mathbf{r}, \mathbf{r}'; E) - G(\mathbf{r}', \mathbf{r}; E)^*\}. \quad (3.53)$$

For simplicity, we will denote the (real and positive) diagonal elements of this matrix as the (l, m) multipole currents $J_{lm}(E)$: $J_{lm}(E) = J_{lm,lm}(E)$.

In the case of no external potentials, these currents are readily evaluated [Bra99] and read

$$J_{lm}^{\text{free}}(E) = \frac{M}{4\pi^2 \hbar^3} \left(\frac{2ME}{\hbar^2} \right)^{l+1/2}. \quad (3.54)$$

The characteristic power law dependence of the scattering rate near threshold is known as Wigner's threshold law [Wig48]. In the present case we have $U(\mathbf{r}) = 0$. Thus all off-diagonal elements $J_{lm,l'm'}^{(\text{free})}(E)$ are zero, and the total current in (3.52) becomes a simple sum:

$$J^{(\text{free})}(E) = \sum_{lm} |\lambda_{lm}|^2 J_{lm}^{(\text{free})}(E). \quad (3.55)$$

This simplification is due to the angular symmetry of the Hamiltonian \mathbf{H} : Assume that the generator of a rotation \mathbf{L} commutes with \mathbf{H} ; then, it will also commute with the resolvent operator $G = [E - \mathbf{H} + i\eta]^{-1}$. Consequently, if the source states $|\sigma\rangle$ and $|\sigma'\rangle$ are eigenstates of \mathbf{L} with different eigenvalues, the mixed matrix element $\langle\sigma|G|\sigma'\rangle$, and hence its contribution to the total current $J(E)$ vanishes. If the potential $U(\mathbf{r})$ is invariant merely with respect to rotations around the z -axis orthogonality with respect to different values of m prevails: $J_{lm,l'm'}(E) = 0$ for $m \neq m'$.

3.5 Green functions from complex integration

For practical calculations we will make extensive use of the Laplace integral representation of the energy-dependent Green function given in equation (3.1). Using this form we can take full advantage of the theory of complex functions for the actual evaluation of the Laplace transform. By regarding t as a complex variable we can study the propagator as a complex valued function over the entire t -plane. Once the analytic properties of a specific propagator are known, we can deform the path of integration and choose a path along which the integral converges fast. Of special importance are the singularities of the propagator and the asymptotic behavior for large absolute values of t . In order to get some graphical overview of the properties of a function in the complex plane we will sometimes use contour plots. In these plots we depict lines of constant absolute value and regions of constant phase.

Example 6 (Contour plot) In Figure 3.1 we plot the function $h(\tau) = \exp(f(\tau))$ with

$$f(\tau) = i \left(\tau(\zeta - \epsilon) + \frac{\xi^2 + \nu^2 + \zeta^2}{\tau} - \frac{\tau^3}{12} \right). \quad (3.56)$$

This function is closely related to the uniform field operator given in equation (2.16). We choose $\xi = -10$, $\nu = 10$, $\zeta = 10000$, $\epsilon = -6$ and cover the complex τ -plane in the interval $\tau = [136.5, 146.4] \times [-2.8i, +2.8i]$. The two stationary points defined by $\partial f(\tau)/\partial\tau|_{\tau=\tau_i} = 0$ are denoted by S_1 and S_2 . The black lines are lines of constant absolute value of $|h(\tau)|$. The shading represents the phase of $h(\tau)$: a constant shading indicates a constant phase. Lines of constant absolute value and lines of constant phase are orthogonal. If we decompose the function $f(\tau) = u(x, y) + iv(x, y)$, we see that the lines of constant phase of $\exp(f(\tau))$ are actually lines of constant imaginary values $iv(x, y)$, and the lines of constant magnitude are lines of constant real parts $u(x, y)$.

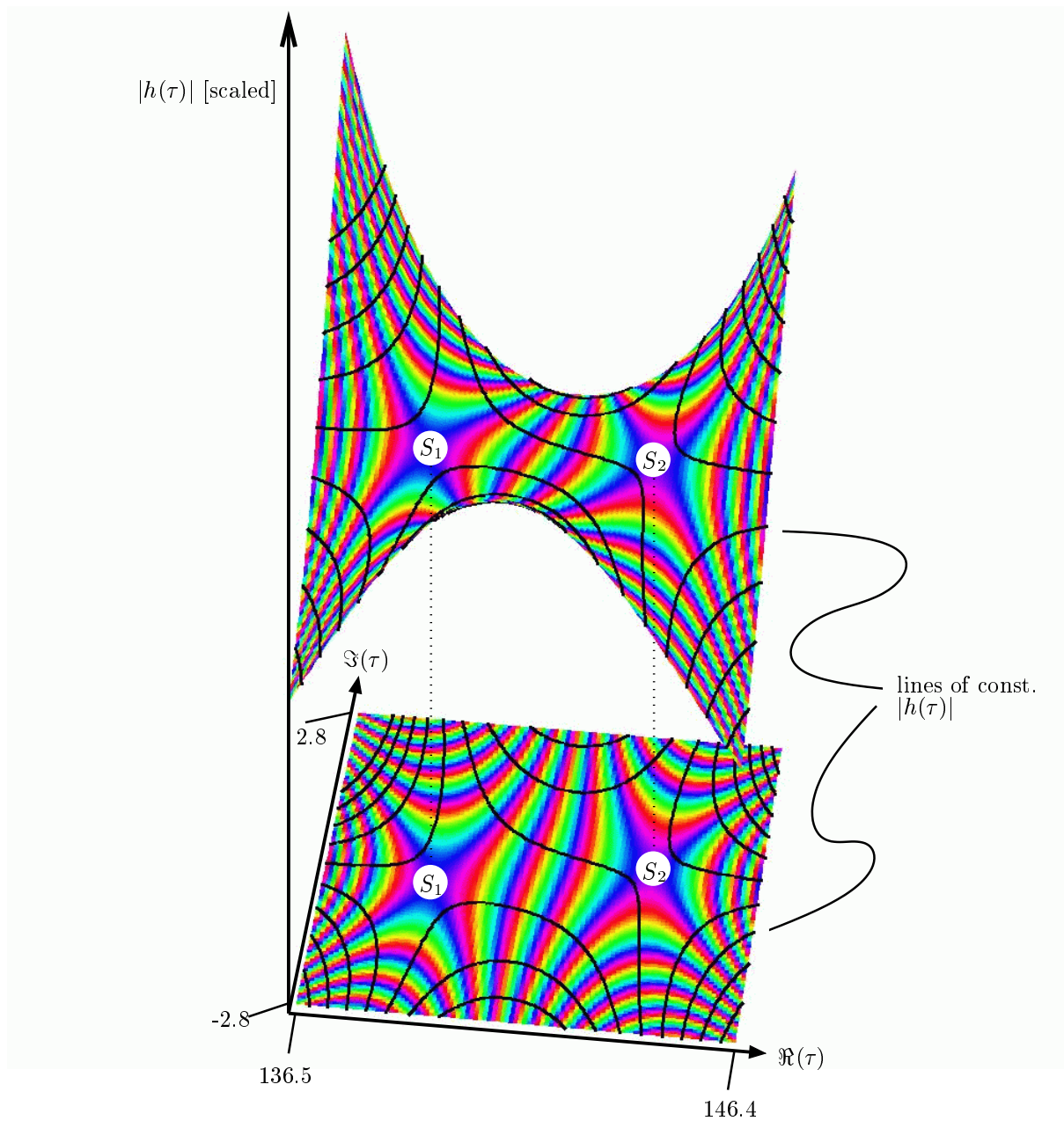


Figure 3.1: Saddle points in the complex plane. We show the function $h(\tau) = \exp(f(\tau))$, discussed in Example 6. Constant shading denotes a constant phase and solid lines indicate a constant absolute value $|h(\tau)|$. The two saddle points of $h(\tau)$ are denoted by S_1 and S_2 . The lower part of the figure is a flattened projection of the upper one.

In general, the propagator has a complicated structure and may exhibit singularities or poles in the complex plane. In this case the following theorem can be employed.

Theorem 3 (Residue theorem) *If the deformed path of integration γ encloses n isolated singularities at points z_k of an otherwise holomorphic function $f(z)$ we can express an integral by the sum of the residues*

$$\int_{\gamma} dz f(z) = 2\pi i \sum_{k=1}^n \text{Res}(f, z_k). \quad (3.57)$$

In Example 2 we used Cauchy's integral theorem, which is a variant of the residue theorem. There, we had a simple singularity in the complex energy plane. Unfortunately the situation can be much more complicated. Essential singularities arise in the propagator of crossed electric and magnetic fields which we will discuss in the next chapter. However, the residues of essential singularities are not easily evaluated and will severely limit the practical use of the residue theorem.

Next, we want to discuss two approximation schemes that are applicable to oscillatory integrals. In the saddle point approximation we deform the path of integration to follow a path of constant phase through the stationary points. These regions give rise to large contributions to the integral, since the oscillatory parts along the remaining regions tend to cancel out. We already discussed a special case, the theory of stationary phase, in the context of the uniform field double-slit in Chapter 2. Here, we give a more general formulation that is based on [Arf70, JS72].

Example 7 (Saddle point approximation) We consider an integral from A to B in the form

$$I = \int_A^B d\tau g(\tau) \exp(sf(\tau)). \quad (3.58)$$

We decompose $f(\tau) = u(x, y) + iv(x, y)$ into the real and imaginary part. In the saddle point approximation, we deform the path of integration in a region between A and B where the real part $u(x, y)$ takes on a positive maximum. Also we will follow a path of constant phase $v(x, y) = v_0 = \text{const}$. Therefore we have

$$I \approx e^{isv_0} \int_A^B d\tau g(\tau) \exp(su(x, y)). \quad (3.59)$$

The maximum of $u(x, y)$ is determined from the condition $\partial u/\partial x = \partial u/\partial y = 0$, or in complex notation $df(\tau)/d\tau = 0$. The name saddle point approximation comes from the fact that a maximum of the real part of $f(\tau)$ implies a minimum of the imaginary part. If we assume that we can form the second derivatives of $u(x, y)$ and $v(x, y)$ the Cauchy-Riemann conditions

$$\frac{\partial u(x, y)}{\partial x} = \frac{\partial v(x, y)}{\partial y}, \quad \frac{\partial u(x, y)}{\partial y} = -\frac{\partial v(x, y)}{\partial x} \quad (3.60)$$

imply that $\partial^2 u / \partial x^2 = -\partial^2 u / \partial y^2$. In Figure 3.1, we see the saddles of the holomorphic function clearly. Next we expand $f(\tau)$ to second order around the stationary point τ_0 :

$$f(\tau) = f(\tau_0) + \frac{1}{2}(\tau - \tau_0)^2 f''(\tau_0) + \dots \quad (3.61)$$

The path we choose is one of real and negative values of $(\tau - \tau_0)^2 f''(\tau_0)$. Writing $\tau - \tau_0 = r e^{i\alpha}$ we define $\zeta^2 = -f''(\tau_0) r^2 e^{2i\alpha} \in \mathbf{R}_+$. Therefore $\zeta = \pm r |f''(\tau_0)|^{1/2}$. Now we substitute the integration variable $d\zeta/d\tau = (d\zeta/dr)(dr/d\tau) = \pm e^{-i\alpha} |f''(\tau_0)|^{1/2}$

$$I \approx \frac{g(\tau_0) e^{s f(\tau_0) + i\alpha}}{|s f''(\tau_0)|^{1/2}} \int_{-\infty}^{\infty} d\zeta e^{-s\zeta^2/2} = \frac{\sqrt{2\pi} g(\tau_0) e^{s f(\tau_0) + i\alpha}}{|s f''(\tau_0)|^{1/2}}, \quad (3.62)$$

and assume a constant $g(\tau)$ in the region $\tau \approx \tau_0$. Also we expanded the range of integration to infinity, since we are only interested in an asymptotic evaluation.

An important special case is the occurrence of a purely imaginary exponent $f(\tau) \equiv i v(x, y)$ with stationary points on the real axis. In that case we have

$$f(\tau - \tau_0) = i v(x_0) + i \frac{1}{2} v''(x_0) (z - z_0)^2 + \dots \quad (3.63)$$

Therefore $\zeta^2 = -i v''(x_0) r^2 e^{2i\alpha}$ and we set $\alpha = (\pi/4) \operatorname{sgn}(v''(x_0))$ in order to satisfy $\zeta^2 \in \mathbf{R}_+$. The final result reads

$$I \approx \frac{\sqrt{2\pi} g(x_0) e^{s i v(x_0) + i\pi/4 \operatorname{sgn}(v''(x_0))}}{|s f''(x_0)|^{1/2}}. \quad (3.64)$$

This form was already used in equation (2.19). Let us briefly comment on a few features of the saddle-point approximation. For a fast convergence we want $s \gg 1$. In some physical problems we have $s = 1/\hbar$. Then the limit $s \rightarrow \infty$ is identical to the so-called semiclassical limit $\hbar \rightarrow 0$. We further assume, that the only contribution along the stationary contour originates from the vicinity of one saddle-point. If for example two stationary points coalesce, this assumption is no longer valid. Sometimes we can save the situation by applying a uniform approximation, see also Example 8. If we have multiple stationary points x_i of an analytic function $f(x)$ on the real axis, the second derivatives (curvatures) of neighboring stationary points $v''(x_i)$ differ by a sign. Therefore we pick up a relative phase factor of $i\pi/2$. Some authors omit this factor in their treatment of the saddle-points and later re-introduce this “phase-jump” somewhat artificially as a consequence of a turning surface or caustic (which separates the two points with different curvature).

The connection between the stationary points of the quantum propagator and the trajectories in classical physics has to be examined carefully. As mentioned before in the context of equation (2.21), at least for quadratic Hamiltonians, we can identify stationary points t_i on the real time axis with classical allowed motion:

$$E + \left. \frac{\partial S_{\text{cl}}(\mathbf{r}, t; \mathbf{r}', 0)}{\partial t} \right|_{t=t_i} = 0. \quad (3.65)$$

Even for stationary points with an imaginary “time” a trajectory analysis can be useful for the semiclassical description of tunneling phenomena [BKK02]. However, in this case no classical trajectories exist. A common complication of the method of stationary points arises if the distance between two stationary points becomes the order of the half width of the Gaussian used in the second order approximation. In this case we have to adapt a more sophisticated approximation scheme. One useful method is the uniform Airy approximation, which uses third order terms. Following [Bri85] we briefly present this method.

Example 8 (Uniform Airy approximation: theory) This methods uses a cubic form of the integrand in order to account for two-saddle points. As before in Example 7 we consider an integral from A to B in the form

$$I = \int_A^B d\tau g(\tau) \exp(sf(\tau)). \quad (3.66)$$

We will introduce a new coordinate $y = y(\tau)$, which maps the function in the exponent $f(\tau)$ to a new form $\phi(y(\tau)) = f(\tau)$, or $\phi(y) = f(\tau(y))$. This new form must have the same structure of stationary points as the original function. The integral reads now

$$I = \int_{y(A)}^{y(B)} dy \tau'(y) g(\tau(y)) \exp(s\phi(y)). \quad (3.67)$$

Now we make two simplifications. First we introduce a new function $h(y)$ for the combination $\tau'(y)g(\tau(y))$. At the stationary points τ_i we require

$$h(y_i) = \tau'(y_i)g(\tau_i). \quad (3.68)$$

The second derivative of the integrand in the new coordinates is given by

$$\phi''(y) = \frac{d\phi'(y)}{dy} = \frac{d}{dy} [f'(\tau(y))\tau'(y)] = \tau''(y)f'(\tau(y)) + (\tau'(y))^2 f''(\tau(y)), \quad (3.69)$$

where all derivatives of τ are taken with respect to y and derivatives of f are with respect to τ . At the stationary points $f'(\tau_i)$ is zero and consequently the first term vanishes. Also at the stationary points the following relation holds:

$$h(y_i) = g(\tau_i) \sqrt{\phi''(y_i)/f''(\tau_i)}. \quad (3.70)$$

The main idea is to use a mapping function ϕ , that has some parameters. These parameters are restricted due to the requirements of equation (3.70), which also connects the mapping function in the exponent $\phi(y)$ with the function $h(y)$.

Let us now specify a form of $\phi(y)$ that is suitable for two stationary points. The simplest approach is to use a cubic polynomial that can accommodate the two stationary points at $y_{1,2} = \pm\sqrt{b}$:

$$\phi(y) = i\eta + iby - iy^3/3. \quad (3.71)$$

For $h(y)$ we use a linear function in y with two parameters $g_{1,2}$

$$h(y) = g_1 + g_2 y. \quad (3.72)$$

Since we have to map $f(\tau_{1,2})$ at the two stationary points $\tau_{1,2}$ onto $\phi(y_{1,2})$, η and b are given by

$$\eta = \frac{f(\tau_1) + f(\tau_2)}{2i}, \quad b = \left[\frac{3}{4} i (f(\tau_2) - f(\tau_1)) \right]^{2/3}. \quad (3.73)$$

Also from equation (3.70) we get

$$g_1 + g_2 \sqrt{b} = g(\tau_1) \sqrt{\frac{+2\sqrt{b}}{f''(\tau_1)/i}}, \quad (3.74)$$

$$g_1 - g_2 \sqrt{b} = g(\tau_2) \sqrt{\frac{-2\sqrt{b}}{f''(\tau_2)/i}}. \quad (3.75)$$

The important case $f(\tau) = iv(\tau)$ yields the following set of equations:

$$\eta = \frac{v(\tau_1) - v(\tau_2)}{2} \quad (3.76)$$

$$b = \left[\frac{3}{4} (v(\tau_1) - v(\tau_2)) \right]^{2/3} \quad (3.77)$$

$$g_1 + g_2 \sqrt{b} = g(\tau_1) \sqrt{\frac{+2\sqrt{b}}{v''(\tau_1)}} \quad (3.78)$$

$$g_1 - g_2 \sqrt{b} = g(\tau_2) \sqrt{\frac{-2\sqrt{b}}{v''(\tau_2)}} \quad (3.79)$$

Now we have equations for all parameters η, b, g_1, g_2 and can evaluate the integral

$$I \approx \int_{-\infty}^{\infty} dy (y g_2 + g_1) e^{i\eta + iby - iy^3/3} = 2\pi [g_1 \text{Ai}(-b) + i g_2 \text{Ai}'(-b)] e^{i\eta}, \quad (3.80)$$

where we used the integral formula for $\text{Qi}_{-1/2}(z)$ given in Appendix B.

Example 9 (Uniform Airy approximation: application) We apply the uniform Airy approximation to the propagator in the linear force field. The stationary points are given in equation (2.18). In Figure 3.2 we compare the saddle-point approximation with the uniform Airy approximation. In general the agreement between the uniform approximation and the exact result is excellent. One reason for the astonishing agreement is that the uniform field propagator is a very good candidate for this type of approximation. The prefactor $T^{-3/2}$ in a Taylor expansion around the stationary points is accurately

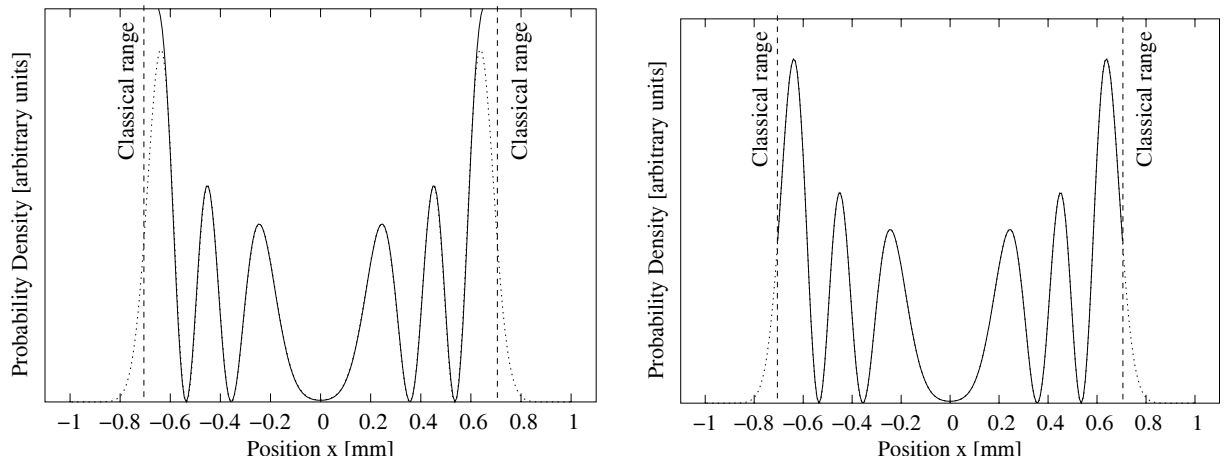


Figure 3.2: Probability density for an electron emitted in a uniform electric field to hit a distant detector plane. The parameters are given in Figure 2.3. Left panel: Saddle point approximation of the energy-dependent Green function. Right panel: Uniform Airy approximation of the same Green function. The dotted line shows the analytical result (see equation (4.21)) and the vertical dashed lines denote the classically accessible range. Note that the uniform Airy approximation correctly describes the decay of the probability density close to the classical range whereas the saddle point solution diverges much earlier.

given by a linear function $T^{-3/2} \approx A + BT$. Exactly this form is assumed in the derivation of the uniform Airy approximation. There is a clear divergence of the saddle-point approximation for lateral distances close to the maximum distance that is classically accessible. This is due to the fact, that the two saddle-points converge to a single point at $R_{\max}^2 = (z + 2E/F)^2 - z^2$. Therefore the assumption of two independent saddle-points is no longer valid and we have to use the uniform approximation. Outside the classically allowed region, the density decays rapidly and none of the approximations can be readily applied.

A last resort is the numerical evaluation of the integral. However, it is easy to get lost in the complex landscape of the quantum propagator. A good understanding of the analytic properties of the function under consideration is crucial for choosing a practicable integration path.

Chapter 4

Uniform magnetic and electric fields

Whereas the propagator for the linear field was derived as early as 1927 [Ken27], at the beginning of quantum mechanics, the case of a static magnetic field and a crossed (possibly time dependent) electric field is much more involved and it took much longer to find the correct result. Nieto [Nie92] considers arbitrary time-dependent electric fields and calculates the corresponding kernel. The case of static fields is somewhat simpler and considered more frequently [Nie92, HCF86, dSdSD88], however sometimes with not quite correct results (comments on this subject appear periodically in the literature, see [JP71, Nie92]). Interestingly, Schwinger derived the relativistic propagator much earlier [Sch51], but there is no simple transition to the non-relativistic case. Therefore, let us outline our procedure to obtain the time-dependent propagator for static fields.

4.1 Gauge properties of the Green function

The Hamiltonian in the presence of magnetic and electric fields may be written as

$$\mathbf{H} = \frac{\left(\mathbf{p} - \frac{q}{c}\mathbf{A}(\mathbf{r}, t)\right)^2}{2m} + q\phi(\mathbf{r}, t) = \frac{\boldsymbol{\pi}^2}{2m} + q\phi(\mathbf{r}, t), \quad (4.1)$$

where

$$\boldsymbol{\pi} = \mathbf{p} - \frac{q}{c}\mathbf{A}(\mathbf{r}, t) \quad (4.2)$$

defines the kinematic momentum. The magnetic field \mathbf{B} is given by the curl of the vector potential \mathbf{A} :

$$\mathbf{B}(\mathbf{r}, t) = \nabla \times \mathbf{A}(\mathbf{r}, t). \quad (4.3)$$

Likewise, the electric field is the gradient of the potential $\phi(\mathbf{r}, t)$:

$$\mathbf{E}(\mathbf{r}, t) = -\frac{1}{c}\frac{\partial\mathbf{A}(\mathbf{r}, t)}{\partial t} - \nabla\phi(\mathbf{r}, t). \quad (4.4)$$

No spin-dependent part of the Hamiltonian is included, since in general we will decouple the spin from the Hamiltonian. The spin will effect the energy of the system, since it shifts

the energy by $\pm\frac{1}{2}g\mu_{\text{Bohr}}B$. For actual applications of the Green function we will have to keep this shift of energy in mind. Also, since we want to construct the Green function, which in turn is closely related to the spectrum of \mathbf{H} , we have to think about the gauge-invariance of the result. It is well known that the Hamiltonian itself is not gauge-invariant. Of course, then the following question arises: How can we assign a useful meaning to the resolvent operator $1/(E - \mathbf{H})$? Horing [Hor65] considers some of the consequences of gauge invariance in the context of the Green function in a uniform magnetic field. We will follow his considerations and extend them to the case of uniform electric and magnetic fields. Since we consider only static fields, we can choose the vector potential and the electric potential to be time-independent. However, the potentials $\mathbf{A}(\mathbf{r})$ and $\phi(\mathbf{r})$ are not uniquely defined. Introducing an arbitrary scalar function $\chi(\mathbf{r}, t)$ we get new potentials

$$\phi'(\mathbf{r}) = \phi(\mathbf{r}) - \frac{1}{c} \frac{\partial \chi(\mathbf{r}, t)}{\partial t}, \quad A'(\mathbf{r}) = A(\mathbf{r}) + \nabla \chi(\mathbf{r}, t), \quad (4.5)$$

connected by the gauge transformation χ . For static, uniform magnetic and electric fields, one choice of the electromagnetic potentials is specified by setting

$$\mathbf{A}(\mathbf{r}) = \frac{1}{2} \mathbf{B} \times \mathbf{r}, \quad \phi(\mathbf{r}) = -\mathbf{r} \cdot \mathbf{E}. \quad (4.6)$$

Possible alternative potentials are given by

$$\mathbf{A}'(\mathbf{r}) = \frac{1}{2} \mathbf{B} \times (\mathbf{r} - \mathbf{r}'), \quad \phi'(\mathbf{r}) = -(\mathbf{r} - \mathbf{r}') \cdot \mathbf{E}. \quad (4.7)$$

The gauge function related to these potentials is found by simply integrating $\nabla \chi = \mathbf{A}' - \mathbf{A}$ and $\partial \chi / \partial t = c(\phi - \phi')$:

$$\chi(\mathbf{r}, t) = \frac{1}{2} \mathbf{B}(\mathbf{r} \times \mathbf{r}') - c \mathbf{r}' \cdot \mathbf{E} t. \quad (4.8)$$

The principle of gauge invariance requires that \mathbf{r} and $\boldsymbol{\pi}$ are independent of the chosen gauge [GP91]. Therefore we introduce a unitary operator \mathbf{T}_χ that has to satisfy the relations

$$\mathbf{r} = \mathbf{T}_\chi \mathbf{r} \mathbf{T}_\chi^\dagger, \quad \boldsymbol{\pi} = \mathbf{T}_\chi \boldsymbol{\pi} \mathbf{T}_\chi^\dagger. \quad (4.9)$$

From these expressions we find that the unitary operator must be

$$\mathbf{T}_\chi = \exp \left(\frac{i q}{\hbar c} \chi(\mathbf{r}, t) \right). \quad (4.10)$$

The Hamiltonian \mathbf{H} is not gauge invariant, but acquires an additional term

$$\mathbf{T}_\chi \mathbf{H} \mathbf{T}_\chi^\dagger = \mathbf{T}_\chi \left(\frac{\boldsymbol{\pi}^2}{2m} + q\phi(\mathbf{r}) \right) \mathbf{T}_\chi^\dagger = \left(\frac{\boldsymbol{\pi}^2}{2m} + q\phi'(\mathbf{r}) \right) + \frac{q}{c} \frac{\partial \chi(\mathbf{r}, t)}{\partial t}. \quad (4.11)$$

This is relevant for the gauge-transformation properties of the energy-dependent Green function. Since we want to keep the form $E - \mathbf{H}$ invariant, we have to introduce a shifted energy in order to compensate the additional term:

$$E - \mathbf{H}(\mathbf{A}, \phi) \rightarrow E - \mathbf{T}_\chi \mathbf{H} \mathbf{T}_\chi^\dagger = E' - \mathbf{H}'(\mathbf{A}', \phi'), \quad (4.12)$$

The regauged energy reads: $E' = E - \frac{q}{c} \frac{\partial \chi}{\partial t}$. Using these results we finally apply the gauge transformation to the Green function. The Green function is defined as the solution of the inhomogeneous Schrödinger equation

$$[E - \mathbf{H}]G(\mathbf{r}, \mathbf{r}'; E) = \delta(\mathbf{r} - \mathbf{r}'). \quad (4.13)$$

The gauge-transformed Hamiltonian \mathbf{H}' appears in the same equation (which we require to be gauge invariant), but all quantities are taken in the new gauge:

$$[E' - \mathbf{H}']G'(\mathbf{r}, \mathbf{r}'; E') = \delta(\mathbf{r} - \mathbf{r}'). \quad (4.14)$$

Looking at the potentials \mathbf{A}' , ϕ' for the Hamilton \mathbf{H}' we note, that they only depend on the relative distance $\mathbf{r} - \mathbf{r}'$. Therefore $G'(\mathbf{r}, \mathbf{r}'; E')$ also depends only on $\mathbf{r} - \mathbf{r}'$. G' is obtained from G with the specified gauge transformation

$$\begin{aligned} \langle \mathbf{r} | G'(E') | \mathbf{r}' \rangle &= \langle \mathbf{r} | \mathbf{T}_\chi G(E) \mathbf{T}_\chi^\dagger | \mathbf{r}' \rangle \\ &= \exp \left[\frac{iq}{\hbar c} (\chi(\mathbf{r}, t) - \chi(\mathbf{r}', t)) \right] \langle \mathbf{r} | G(E) | \mathbf{r}' \rangle \\ &= \exp \left[\frac{iq}{2\hbar c} \mathbf{B}(\mathbf{r} \times \mathbf{r}') \right] \langle \mathbf{r} | G(E) | \mathbf{r}' \rangle. \end{aligned}$$

If we set $\mathbf{r}' = 0$, the gauge term vanishes. This offers another interpretation of the gauge-transformation. Switching from the potentials (\mathbf{A}, ϕ) to the new ones (\mathbf{A}', ϕ') is actually a coordinate transformation according to a shift $\mathbf{r} \rightarrow \mathbf{r} - \mathbf{r}'$. Thus, we have a second relation between the Green functions in the different gauges

$$G'(\mathbf{r}, \mathbf{r}'; E') = G(\mathbf{r} - \mathbf{r}', \mathbf{o}; E'). \quad (4.15)$$

Together with the previous equation we obtain the final result

$$\exp \left[\frac{iq}{2\hbar c} \mathbf{B}(\mathbf{r}' \times \mathbf{r}) \right] G(\mathbf{r} - \mathbf{r}', \mathbf{o}; E + \mathbf{r}' \cdot \mathbf{F}) = G(\mathbf{r}, \mathbf{r}'; E). \quad (4.16)$$

One important application of this expression is the extension of a Green function obtained for $\mathbf{r}' = 0$ to the full coordinate set $(\mathbf{r}, \mathbf{r}')$. We will use this later for the derivation of the energy-dependent Green function. We also note that the gauge terms are time-independent and the same translation property applies to the time-dependent Green function.

4.2 Propagator in crossed magnetic and electric fields

Before we actually address the calculation of the energy-dependent Green function, we will discuss the time-dependent kernel. For this task we use the linear canonical transformation

method described in Section 3.3. In Appendix A.1 we give the details of the straightforward calculation. The final result is rather long and reads:

$$\begin{aligned}
K_{\mathbf{EB}}(\mathbf{r}, t | \mathbf{r}', 0) &= e^{-3i\pi/4} \frac{m\omega_L}{2\pi\hbar \sin(\omega_L t)} \sqrt{\frac{m}{2\pi\hbar t}} \times \\
&\times \exp \left\{ \frac{i}{\hbar} \left(\frac{m}{2t} (\mathbf{r}_{\parallel} - \mathbf{r}'_{\parallel})^2 + \frac{m\omega_L}{4} (\mathbf{r}_{\perp} - \mathbf{r}'_{\perp})^2 \cot(\omega_L t) + \frac{e}{2} [\mathbf{r}_{\perp}, \mathbf{B}, \mathbf{r}'_{\perp}] \right. \right. \\
&\quad + \left(\frac{e}{m\omega_L^2} - \frac{et}{2m\omega_L} \cot(\omega_L t) \right) [\mathbf{r}_{\perp} - \mathbf{r}'_{\perp}, \mathbf{F}_{\perp}, \mathbf{B}] + \frac{t}{2} (\mathbf{r} + \mathbf{r}') \mathbf{F} \\
&\quad \left. \left. - F_{\parallel}^2 \frac{t^3}{24m} + F_{\perp}^2 \left[-\frac{t}{8m\omega_L^2} + \frac{t^2}{8m\omega_L} \cot(\omega_L t) \right] \right) \right\}. \quad (4.17)
\end{aligned}$$

The Larmor frequency ω_L is defined by

$$\omega_L = \frac{eB}{2m}. \quad (4.18)$$

We introduced the subscript \parallel for vector components parallel to the magnetic field \mathbf{B} and \perp for the perpendicular component. The triple product $[a, b, c]$ is understood as

$$[a, b, c] = (a \times b) \cdot c. \quad (4.19)$$

As a cross-check we can investigate the transformation properties under spatial translations. The two terms related to the gauge-transformation are readily identified and we see that this kernel indeed satisfies equation (4.16):

$$e^{iEt/\hbar} K_{\mathbf{EB}}(\mathbf{r}, t | \mathbf{r}', 0) = e^{i(E+\mathbf{r}'\mathbf{F})t/\hbar} K_{\mathbf{EB}}(\mathbf{r} - \mathbf{r}', t | \mathbf{o}, 0) \exp \left\{ \frac{ie}{2\hbar} [\mathbf{r}_{\perp}, \mathbf{B}, \mathbf{r}'_{\perp}] \right\}. \quad (4.20)$$

Next we will discuss four important special cases of the general propagator.

4.3 Purely electric field

The case of a multipole source in a purely electric field is treated in great detail by Bracher [Bra99]. A closed analytic expression for the underlying Green function was derived independently by several authors [DS76, LLF90, GKK91]

$$G(\mathbf{r}, \mathbf{r}'; E) = \frac{m}{2\hbar^2} \frac{1}{|\mathbf{r} - \mathbf{r}'|} [\text{Ci}(\alpha_+) \text{Ai}'(\alpha_-) - \text{Ci}'(\alpha_+) \text{Ai}(\alpha_-)], \quad (4.21)$$

where the arguments α_{\pm} of the Airy functions $\text{Ai}(u)$, $\text{Ci}(u) = \text{Bi}(u) + i\text{Ai}(u)$ [AS65] are given by

$$\alpha_{\pm} = -\beta [2E + F(z + z') \pm F|\mathbf{r} - \mathbf{r}'|]. \quad (4.22)$$

Again, β denotes an inverse energy scale of the system that varies with the force strength F

$$\beta = (m/4\hbar^2 F^2)^{1/3}. \quad (4.23)$$

The current density for a point-like source is readily evaluated and reads for s-wave scattering $l = 0$

$$\mathbf{j}_{00,z}(\mathbf{r}, E) = |C|^2 \frac{m\beta F}{8\pi^2 \hbar^3 r^3} \left\{ z [\text{Ai}'(\alpha_-)]^2 + \beta [z(2E + Fz) + Fr^2] [\text{Ai}(\alpha_-)]^2 \right\}. \quad (4.24)$$

Similarly, the total current according to equation (2.38) becomes

$$\begin{aligned} J_{00}(E) &= -\frac{|C|^2}{2\pi\hbar} \lim_{r \rightarrow 0} \text{Im} \{G_{\text{field}}(\mathbf{r}, \mathbf{o}; E)\} \\ &= \frac{|C|^2 m\beta F}{2\pi\hbar^3} \left\{ [\text{Ai}'(-2\beta E)]^2 + 2\beta E [\text{Ai}(-2\beta E)]^2 \right\}. \end{aligned} \quad (4.25)$$

In a different context, these expressions are implicitly contained also in [LLF90, Fab91]. A general method to express the higher multipole Green-functions is given in [Bra99, BKK02].

4.4 Parallel magnetic and electric fields

For the case of parallel fields ($B \neq 0$, $F_{\perp} = 0$) the general propagator stated in equation (4.17) is written in the much simpler form ($\rho^2 = x^2 + y^2$)

$$K_{\mathbf{B}\parallel\mathbf{E}}(\mathbf{r}, t|\mathbf{o}, 0) = K_{\mathbf{B}}^{(2D)}(\boldsymbol{\rho}, t|\mathbf{o}, 0) K_{\text{field}}^{(1D)}(z, t|\mathbf{o}, 0), \quad (4.26)$$

with

$$K_{\mathbf{B}}^{(2D)}(\boldsymbol{\rho}, t|\mathbf{o}, 0) = \frac{m\omega_L}{2\pi i \hbar \sin(\omega_L t)} \exp\left(i \frac{m\omega_L}{2\hbar} \rho^2 \cot(\omega_L t)\right), \quad (4.27)$$

and $K_{\text{field}}^{(1D)}(z, t|0, 0)$ given already in equation (3.14). We proceed to calculate the energy-dependent Green function. Transforming both propagators separately we can use the already given Laplace transform of $K_{\text{field}}^{(1D)}$ (see equation (3.11)). For the magnetic part we take advantage of the close connection of the propagator to the generating function of the Laguerre polynomials.

Theorem 4 (Laguerre polynomials) *The generating function of the Laguerre polynomials is ([AS65], (22.9.15))*

$$\exp\left(-\frac{xt}{1-t}\right) (1-t)^{-1} = \sum_{n=0}^{\infty} L_n^{(0)}(x) t^n. \quad (4.28)$$

This form can be transformed to hyperbolic or trigonometric functions

$$\frac{1}{\sinh(z)} \exp[-\alpha \coth(z)] = 2e^{-\alpha} \sum_{n=0}^{\infty} L_n^{(0)}(2\alpha) e^{-2z(n+1/2)}, \quad (4.29)$$

where we introduce $t = e^{-z}$ in the generating function.

Setting $z = i\omega_L t$ and $\alpha = \frac{m\omega_L}{2\hbar}\rho^2$ we carry out the time-integration in

$$\begin{aligned} G_{\mathbf{B}}^{(2D)}(\boldsymbol{\rho}, \mathbf{o}; E) &= -\frac{i}{\hbar} \frac{2m\omega_L}{2\pi\hbar} \sum_{n=0}^{\infty} e^{-\alpha} L_n^{(0)}(2\alpha) \lim_{\eta \rightarrow 0} \int_0^{\infty} dt e^{-i\omega_L(2n+1)t + i(E+i\eta)t/\hbar} \quad (4.30) \\ &= -\frac{m\omega_L}{\pi\hbar} \sum_{n=0}^{\infty} \lim_{\eta \rightarrow 0} \frac{e^{-\alpha} L_n^{(0)}(2\alpha)}{E - \hbar\omega_L(2n+1) + i\eta}. \end{aligned}$$

In the last step we apply the complex convolution theorem (see Example 4, equation (3.18)) and use Cauchy's integral theorem:

$$\begin{aligned} G_{\mathbf{B}\|\mathbf{E}}(\mathbf{r}, \mathbf{o}; E) &= \frac{1}{2\pi i} \exp\left(-\frac{m\omega_L}{2\hbar}\rho^2\right) \sum_{n=0}^{\infty} L_n^{(0)}\left(\frac{m\omega_L}{\hbar}\rho^2\right) \int_{-\infty}^{\infty} dE' \frac{\frac{m\omega_L}{\pi\hbar} G_{\text{field}}(z, 0; E')}{E' - E + \hbar\omega_L(2n+1)} \\ &= \frac{\hbar\omega_L m^2}{F\beta \hbar^4} \exp\left(-\frac{m\omega_L}{2\hbar}\rho^2\right) \sum_{n=0}^{\infty} L_n^{(0)}\left(\frac{m\omega_L}{\hbar}\rho^2\right) \times \\ &\quad \times \text{Ci}\{2\beta[F(z+|z|)/2 - E + \hbar\omega_L(2n+1)]\} \times \\ &\quad \times \text{Ai}\{2\beta[F(z-|z|)/2 - E + \hbar\omega_L(2n+1)]\}. \end{aligned} \quad (4.31)$$

The parameter $\beta = [m/(4\hbar^2 F^2)]^{1/3}$ has the dimension of an inverse energy. A similar result is obtained by Fabrikant ([Fab91], equation (11)) in the context of a calculation for $l = 1$ photodetachment. Using the gauge transformation (4.16) we relocate the origin from \mathbf{o} to \mathbf{r}' :

$$\begin{aligned} G_{\mathbf{B}\|\mathbf{E}}(\mathbf{r}, \mathbf{r}'; E) &= \frac{\omega_L m^2}{F\beta \hbar^3} e^{\frac{m\omega_L}{\hbar} \left[i(xy' - yx') - \frac{(x-x')^2 + (y-y')^2}{2} \right]} \sum_{n=0}^{\infty} L_n^{(0)}\left(\frac{m\omega_L}{\hbar}((x-x')^2 + (y-y')^2)\right) \times \\ &\quad \times \text{Ci}\{2\beta[(F(z-z') + F|z-z'|)/2 - E + \hbar\omega_L(2n+1)]\} \times \\ &\quad \times \text{Ai}\{2\beta[(F(z-z') - F|z-z'|)/2 - E + \hbar\omega_L(2n+1)]\}. \end{aligned} \quad (4.32)$$

Having an analytic expression for the energy-dependent Green function, we continue with the derivation of the currents generated by a point source of electrons embedded into the electromagnetic fields.

4.4.1 Total current in parallel fields

Following Section 3.4, a systematic approach to the total current of a multipole source in parallel fields is feasible. In the literature exist some articles on the total current with angular momentum $l = 1$ in parallel fields [DD89, Fab91, PJGD97]. These papers deal with the specific problem of the calculation of the photodetachment cross-section from H^- . Since the energy-dependent Green function is available in analytic form, we can readily

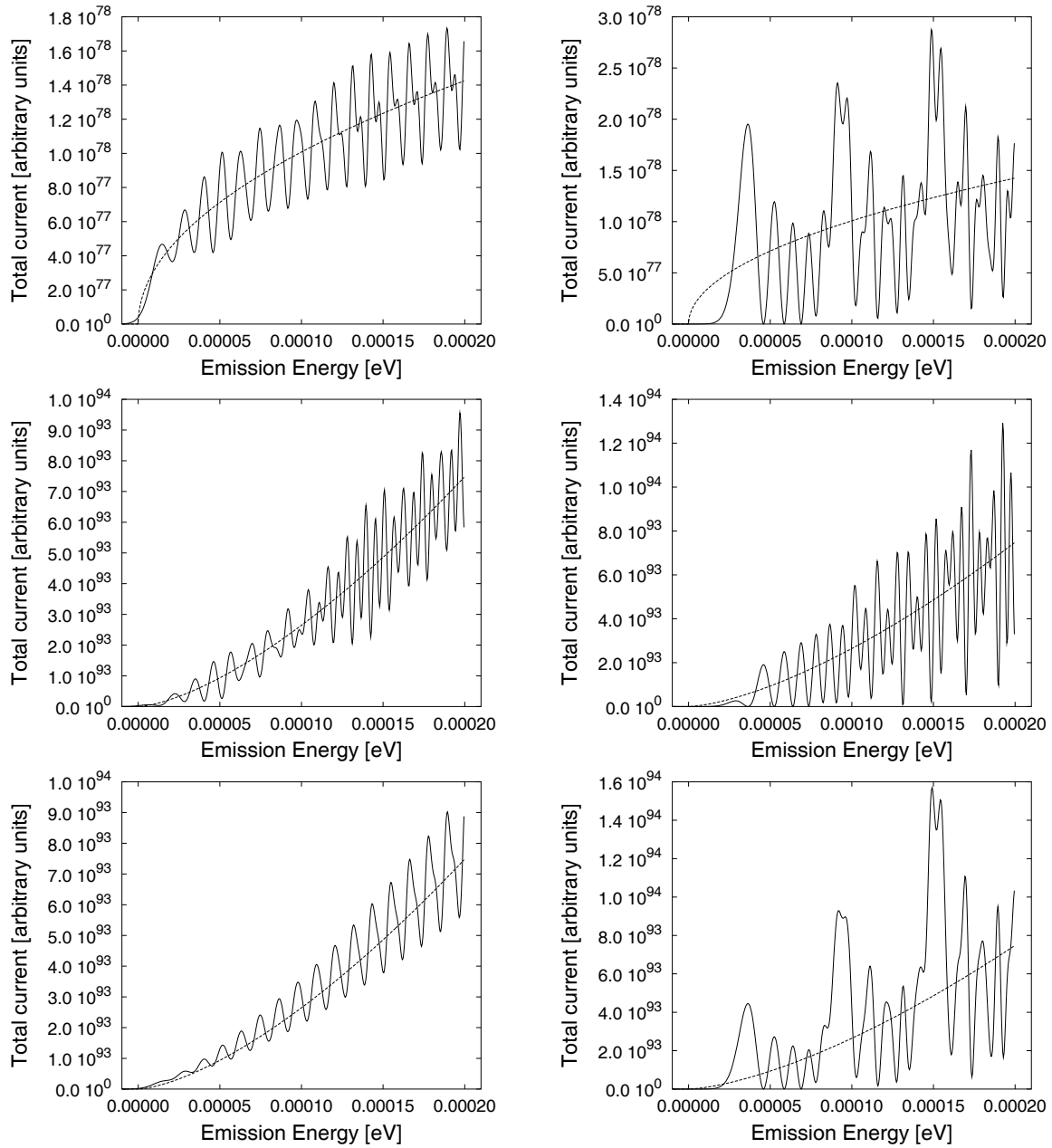


Figure 4.1: Total current for different multipole sources in parallel magnetic and electric fields. Electric field: $F = 100$ eV/m, magnetic field: $B = 0.1$ T (left column) and $B = 0.5$ T (right column). Upper row: $l = m = 0$, middle row: $l = 1, m = 0$, lower row: $l = 1, m = -1$. The dashed line denotes Wigner's threshold law given in equation (3.54).

derive all higher multipole currents. Here, we merely list the expressions for $l = 0, 1$:

$$J_{00}(E) = \sum_{n=0}^{\infty} \frac{m^2 \omega_L}{2\pi\beta F \hbar^4} [\text{Ai}(2\beta\{-E + \hbar\omega_L(2n+1)\})]^2 \quad (4.33)$$

$$J_{1-1}(E) = \sum_{n=0}^{\infty} \frac{3m^3 \omega_L^2 (n+1)}{\pi\beta F \hbar^5} [\text{Ai}(2\beta\{-E + \hbar\omega_L(2n+1)\})]^2 \quad (4.34)$$

$$J_{10}(E) = \sum_{n=0}^{\infty} \frac{6\beta F m^2 \omega_L}{\pi \hbar^4} [\text{Ai}'(2\beta\{-E + \hbar\omega_L(2n+1)\})]^2 \quad (4.35)$$

$$J_{11}(E) = \sum_{n=0}^{\infty} \frac{3m^3 \omega_L^2 n}{\pi\beta F \hbar^5} [\text{Ai}(2\beta\{-E + \hbar\omega_L(2n+1)\})]^2 \quad (4.36)$$

In Figure 4.1 we show plots of these currents and compare them to the ones generated by a multipole source without external fields.

4.4.2 Current Density

Another quantity of interest is the spatial distribution of the current. No experimental measurements on the current density have been performed yet. Surprisingly, even very weak magnetical fields are of great importance for the range of electric field parameters typically used in photodetachment experiments [BDD96].

From the Green function we can derive the current density, which becomes in the case of s-wave detachment (see equation (2.36), for our choice of the vector potential $\mathbf{A}_z = 0$)

$$\mathbf{j}_{\mathbf{B}\parallel\mathbf{E},00,z}(\mathbf{r}) = \frac{\hbar|C|^2}{4\pi m} \Im \left[G_{\mathbf{B}\parallel\mathbf{E}}^*(\mathbf{r}, \mathbf{o}; E) \frac{\partial}{\partial z} G_{\mathbf{B}\parallel\mathbf{E}}(\mathbf{r}, \mathbf{o}; E) \right]. \quad (4.37)$$

A plot of the current density distribution for $B = 0.001$ T and $F = 116$ eV/m is given in Figure 4.2. The differences to the electric case are striking. The propagation in the lateral direction is confined due to the magnetic field. At some regions a very narrow constriction region exists, but the current density survives the passage through this area and regains its lateral spread. In Figure 4.3 we zoom into the constriction region and see that the current distribution gives a rather long filament surrounded by a region with spot like structures.

Semiclassical Approximation The current profile can be approximated semiclassically by applying the method of stationary phase to the Green function. Since we know that the stationary points of the classical action are related to the classical trajectories, we also write down the classical equation of motion. For fixed E , all classical trajectories start with initial kinematic momentum $p = \sqrt{2mE}$. If we denote the angle between the z -axis and the direction of emission by θ , the classical equation of motion becomes

$$\rho(t, \theta) = p \sin \theta \frac{|\sin(\omega_L t)|}{m\omega_L}, \quad z(t, \theta) = p \cos \theta \frac{t}{m} - \frac{Ft^2}{2m}. \quad (4.38)$$

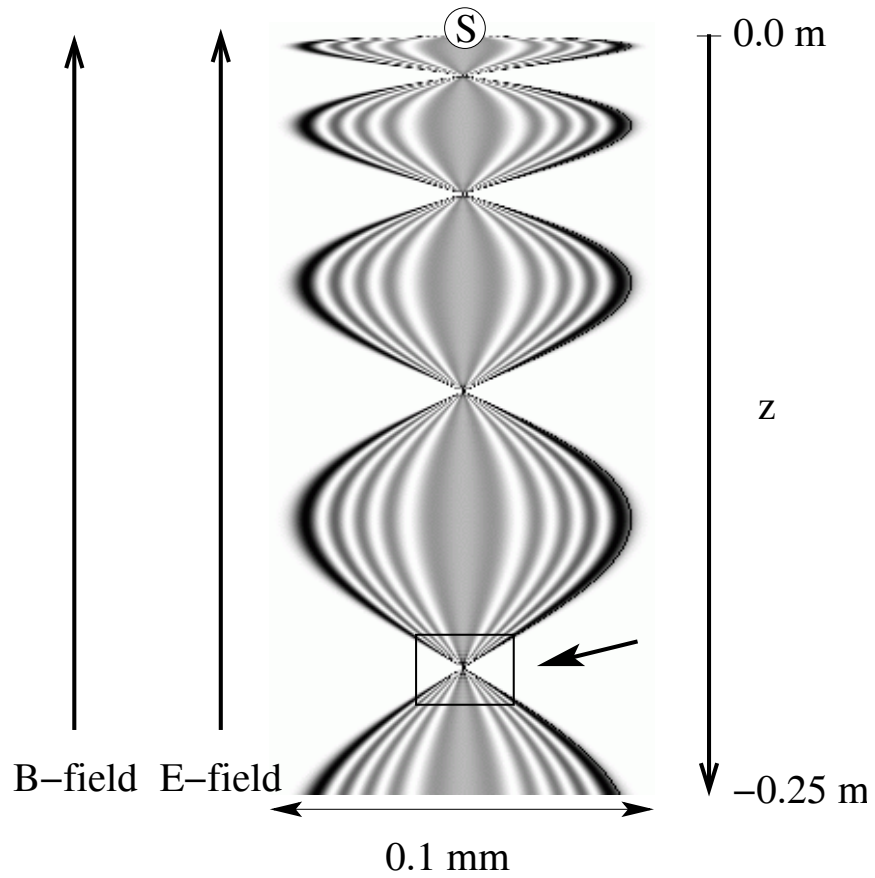


Figure 4.2: Plot of the current density distribution obtained from equation (4.37) for parallel fields. The fourth resonance (arrow) is plotted in detail in Figure 4.3. Parameters: Emission energy: $E = 60.8 \mu\text{eV}$, electric field: $F = 116 \text{ eV/m}$, magnetic field: $B = 0.001 \text{ T}$. There is rotational symmetry about the z -axis.

These relations can be used to determine the shape of the envelope of the current profile. According to equation (4.38), the maximum lateral extension is given by the cyclotron radius $\rho_{\max} = p/(m\omega_L)$ for $\theta = \pi/2$, and $\omega_L t = \pi/2$. To obtain the minimum lateral extension we observe that $\rho(t)$ will periodically vanish at $t = T_k$. However, due to the initial momentum, at these instances the trajectories will cover a range of z -coordinates from $z(T_k, 0)$ to $z(T_k, \pi)$. Thus, we have to keep the z -coordinate fixed and then search for the maximum value of ρ . This can be done by parameterizing all quantities by the emission angle θ close to a the center of the resonance given by $z(T_k, \theta)$:

$$\rho(\theta) \approx \frac{p}{m} \sin(\theta) \delta t(\theta) \quad (4.39)$$

$$z(\theta) \approx p \cos(\theta) \frac{T_k}{m} - \frac{FT_k^2}{2m} - \frac{F}{m} \delta t(\theta) T_k \quad (4.40)$$

Since we seek the maximum value, we have to fulfill the conditions

$$\frac{\partial \rho(\theta)}{\partial \theta} = 0 = \cos(\theta) \delta t + \sin(\theta) \frac{\partial \delta t}{\partial \theta} \quad (4.41)$$

$$\frac{\partial z(\theta)}{\partial \theta} = 0 = p \sin(\theta) \frac{T_k}{m} - \frac{F}{m} T_k \frac{\partial \delta t}{\partial \theta} \quad (4.42)$$

Using these equations to eliminate δt and $\partial \delta t / \partial \theta$ we obtain:

$$\begin{aligned} \rho(\theta) &\approx \frac{2E}{F} \left| \frac{\sin^3 \theta}{\cos \theta} \right|, \\ z(\theta) &\approx z_k - \frac{p}{m} T_k \frac{\cos(2\theta)}{\cos \theta}. \end{aligned}$$

Thus, the constriction is narrowest at z_k , where the width \overline{AC} of the focal spot is independent of \mathbf{B} : $\overline{AC} \approx E/F$. Interestingly, the elongation of the resonance region $\overline{BD} = (2k\pi p)/(\omega_L m)$ does not involve the electric field \mathbf{F} . A further analysis shows, that in this region each point is connected by four classical trajectories with the source. Outside the constriction region the twofold degeneracy familiar from the purely electric case persists. For the semiclassical saddle-point approximation of the Green function

$$G_{\mathbf{F} \parallel \mathbf{B}}(\mathbf{r}, \mathbf{o}; E) = \frac{1}{i\hbar} \int_0^\infty dt \sqrt{\frac{m}{2\pi i \hbar t}} \frac{m\omega_L}{2\pi i \hbar \sin(\omega_L t)} e^{\frac{i}{\hbar} \left(Et + \frac{m\omega_L}{2} \rho^2 \cot(\omega_L t) + \frac{m}{2t} z^2 - \frac{Ft}{2} z - \frac{F^2 t^3}{24m} \right)}, \quad (4.43)$$

we must therefore include up to four contributions from stationary points. In Figure 4.3, the encircled numbers denote the count of classical trajectories in each sector. The semiclassical result (left hand side), obtained by summing over all classical paths in equation (4.43), faithfully reproduces the exact quantum solution available from equations (4.37) and (4.31) (shown to the right).

Also, we should point out that the resonances will overlap ($z(T_k, \pi) < z(T_{k+1}, 0)$) for $F/(pB) < e/(\pi m)$. In this instance, the number of classical paths may exceed four.

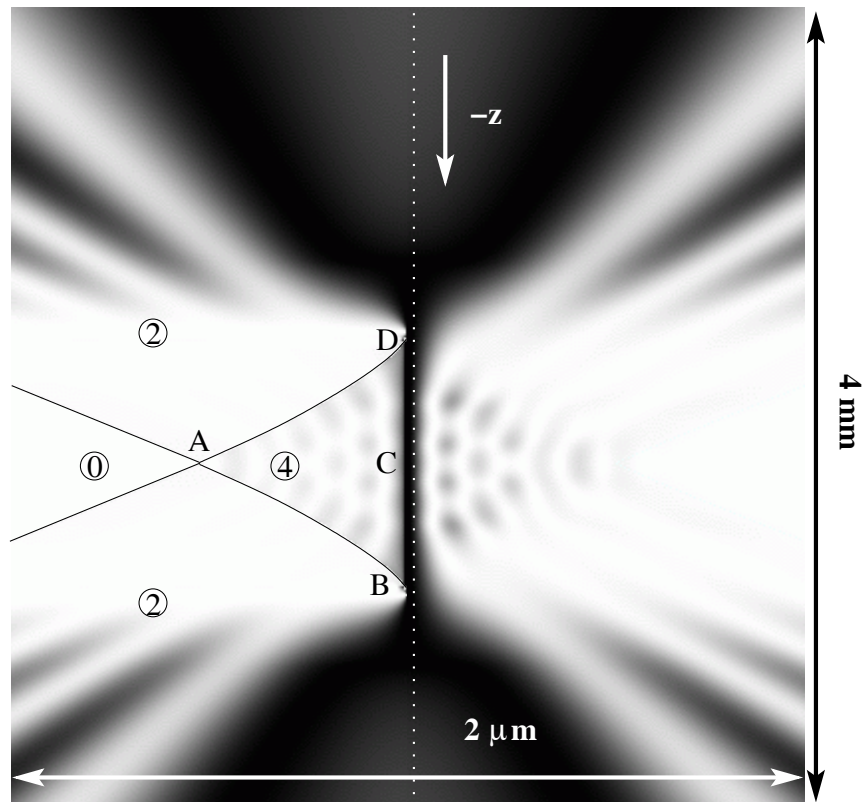


Figure 4.3: Anatomy of the fourth resonance in Figure 4.2. Circled numbers: number of classically allowed trajectories. Left hand side: semiclassical approximation. Right hand side: quantum solution. Scale: height 4 mm, width $2 \mu\text{m}$. Same parameters as in Figure 4.2.

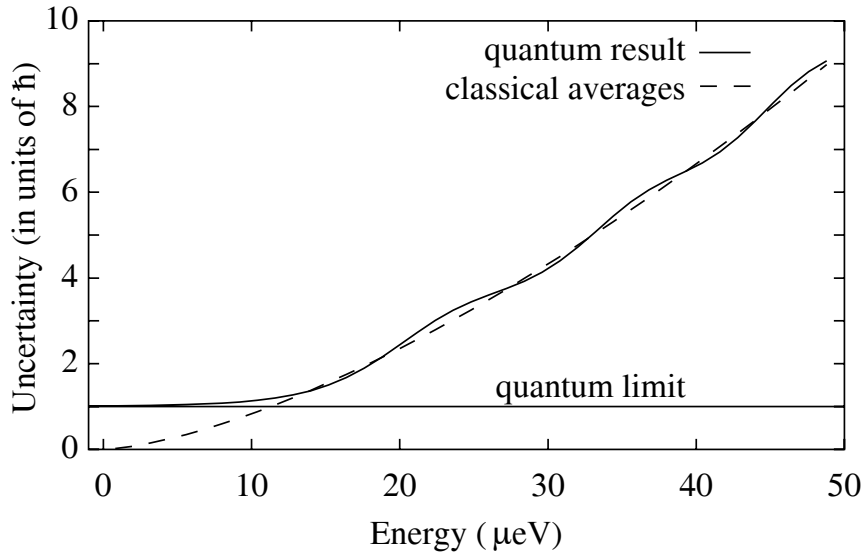


Figure 4.4: Uncertainty product $\Delta r_{\perp} \Delta p_{\perp}$ and classical averages, equation (4.44), as a function of emission energy in units of \hbar , fourth resonance, $F = 116$ eV/m, $B = 0.001$ T.

4.4.3 Minimum Uncertainty

At the photodetachment threshold ($E \rightarrow 0$), the classical width of the current filament, $\overline{AC} \approx E/F$, approaches zero. However, the uncertainty principle will put some constraints on the lateral current density distribution. Let us first elaborate on the classical picture: Since the emission is isotropic, the average value of p_{\perp}^2 is $\langle p_{\perp}^2 \rangle_{\text{av}} = \frac{2}{3} p^2 = \frac{4}{3} mE$. For the mean square width $\langle r_{\perp}^2 \rangle_{\text{av}}$ of the distribution, we integrate over all trajectories $\rho(\theta)$ (Equation 4.38) that arrive at z_k . For non-overlapping resonances, this procedure yields approximately:

$$\sqrt{\langle r_{\perp}^2 \rangle_{\text{av}} \langle p_{\perp}^2 \rangle_{\text{av}}} \approx \frac{E}{F} \sqrt{\frac{32}{45} mE}. \quad (4.44)$$

In a quantal treatment the relevant operators are the canonical momentum operator and the position operator:

$$p_{\perp}^2 = p_x^2 + p_y^2, \quad r_{\perp}^2 = x^2 + y^2.$$

For these operators the relation

$$\sqrt{\langle r_{\perp}^2 \rangle \langle p_{\perp}^2 \rangle} \geq \hbar \quad (4.45)$$

must hold. The evaluation of the expectation value of $r_{\perp}^2 = \rho^2$ and p_{\perp} with respect to the scattered wave function (which is proportional to the Green function) is carried out by

calculating the expectation values

$$\langle r_{\perp}^2 \rangle = \int_0^{\infty} d\rho \rho G_{\mathbf{F}\parallel\mathbf{B}}(\mathbf{r}, \mathbf{o}; E)^* \rho^2 G_{\mathbf{F}\parallel\mathbf{B}}(\mathbf{r}, \mathbf{o}; E), \quad (4.46)$$

$$\langle p_{\perp}^2 \rangle = \int_0^{\infty} d\rho \rho G_{\mathbf{F}\parallel\mathbf{B}}(\mathbf{r}, \mathbf{o}; E)^* \left[-\frac{1}{\rho} \frac{\partial}{\partial \rho} \rho \frac{\partial}{\partial \rho} \right] G_{\mathbf{F}\parallel\mathbf{B}}(\mathbf{r}, \mathbf{o}; E), \quad (4.47)$$

separately and normalizing them by

$$N_{\text{lat}} = \int_0^{\infty} d\rho \rho G_{\mathbf{F}\parallel\mathbf{B}}(\mathbf{r}, \mathbf{o}; E)^* G_{\mathbf{F}\parallel\mathbf{B}}(\mathbf{r}, \mathbf{o}; E). \quad (4.48)$$

In Figure 4.4 we compare the expectation value $\Delta r_{\perp} \Delta p_{\perp} = \sqrt{\langle r_{\perp}^2 \rangle \langle p_{\perp}^2 \rangle}$ as calculated from the last set of equations with the corresponding classical average $\sqrt{\langle r_{\perp}^2 \rangle_{\text{av}} \langle p_{\perp}^2 \rangle_{\text{av}}}$ as a function of energy. Once the classical average exceeds the quantum limit \hbar , the semiclassical theory provides a good estimate for the uncertainty product (and the current profile in general). For sufficiently small energies E , however, a quantal regime prevails: The uncertainty quickly approaches its lower boundary, and consequently, the current distribution becomes Gaussian in shape. Typically, this behavior becomes prevalent at energies of order $E \approx 1/\beta$; the resulting minimum uncertainty wave function is considerably extended in space, as an estimate of the focal spot radius $\Delta r_{\perp} \approx 1/(\beta F)$ shows: For the field strengths used experimentally [BDD96, BDDV99], a resolution of order $\Delta r_{\perp} \approx 100$ nm is achieved.

4.5 Purely magnetic field

The limit of a strong magnetic field is of considerable importance in solid state physics. We already mentioned that the density of states (DOS) is just a multiple of the total current (see equation (3.26)). In solid state physics the DOS of a free (degenerate) electron gas (DEG) in two and three dimensions (2-DEG, 3-DEG) is used to calculate properties of materials like conductivity, heat capacity, magnetization, etc.

First, we derive the density of states in the presence of a magnetic field for a two dimensional source. The energy-dependent Green function $G_{\mathbf{B}}(\boldsymbol{\rho} = \mathbf{o}, \boldsymbol{\rho}' = \mathbf{o}; E)$ is given in equation (4.30). We get the total current by taking the imaginary part of this expression. Employing the relation (see also equation (3.22))

$$\lim_{\eta \rightarrow 0} \frac{1}{E - E' + i\eta} = \text{PP} \left(\frac{1}{E - E'} \right) + i\pi \delta(E - E' + i\eta), \quad (4.49)$$

we obtain the density of states

$$n_{\mathbf{B}}^{(2D)}(E) = -\frac{1}{\pi} \Im \{ G_{\mathbf{B}}^{(2D)}(\mathbf{o}, \mathbf{o}, E) \} = \frac{m\omega_L}{\pi\hbar} \sum_{n=0}^{\infty} \delta(E - \hbar\omega_L[2n + 1]). \quad (4.50)$$

The spiked δ -array is the expected result for the DOS. This configuration is relevant for the study of the quantum Hall effect, see i.e. [GP00]. We will further comment on the

quantum Hall DOS in the next chapter. Some authors define the degeneracy $N_L(B)$ of an individual Landau level by the relation

$$N_L(B) = n_{\text{free}}^{(2D)} 2\hbar\omega_L. \quad (4.51)$$

The DOS in the absence of external fields follows immediately from the free energy-dependent Green function in two dimensions and reads

$$n_{\text{free}}^{(2D)} = \Theta(E) \frac{m}{2\pi\hbar^2}. \quad (4.52)$$

Combining both results gives another expression for the degeneracy

$$N_L(B) = \frac{eB}{2\pi\hbar}. \quad (4.53)$$

In three dimensions, we have a completely different behavior. For the imaginary part of the Green function we must evaluate the convolution integral of the combined propagator for a one-dimensional free motion

$$K_{\text{free}}^{(1D)}(z, t|z', 0) = \sqrt{\frac{m}{2\pi i\hbar t}} e^{im(z-z')^2/(2\hbar t)}, \quad (4.54)$$

and the two-dimensional magnetic field contribution (stated in equations (4.27) and (4.30)). This procedure yields the following expression

$$G_{\mathbf{B}}^{(3D)}(\mathbf{o}, \mathbf{o}, E) = -\frac{i}{\hbar} \frac{m\omega}{\pi\hbar} \sum_{n=0}^{\infty} \int_0^{\infty} dt \sqrt{\frac{m}{2\pi i\hbar t}} e^{iEt/\hbar} e^{-i\omega_L(2n+1)t}, \quad (4.55)$$

that is again closely related to the energy-dependent Green function of a one-dimensional free particle:

$$G_{\text{free}}^{(1D)}(z, z'; E) = -\frac{i}{\hbar} \int_0^{\infty} dt e^{iEt/\hbar} K_{\text{free}}^{(1D)}(z, t|z', 0) \quad (4.56)$$

$$= \frac{1}{\hbar} \sqrt{-\frac{m}{2E}} e^{-|z-z'|\sqrt{-2mE}/\hbar} \quad (4.57)$$

The only effect of the magnetic field (besides a constant factor), is to cause a superposition of shifted one-dimensional free Green functions. Thus, the density of states becomes

$$n_{\mathbf{B}}^{3D}(E) = -\frac{1}{\pi} \Im\{G_{\mathbf{B}}^{3D}(\mathbf{o}, \mathbf{o}, E)\} = \frac{m^{3/2}\omega_L}{2^{1/2}\pi^2\hbar^2} \sum_{n=0}^{\infty} \frac{\Theta(E - \hbar\omega_L[2n+1])}{\sqrt{E - \hbar\omega_L[2n+1]}}. \quad (4.58)$$

In Figure 4.5 we plot the resulting curve and see that it has indeed the familiar form of the DOS for a three-dimensional electron gas [GP00], p. 552.

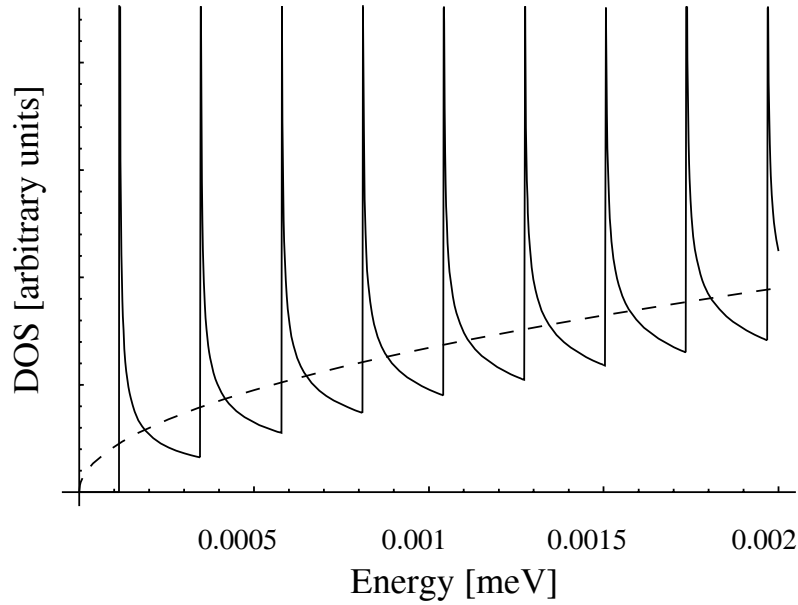


Figure 4.5: Electronic density of states in three dimensions and a strong magnetic field ($B = 1$ T). The dashed line denotes Wigner's threshold law given in equation (3.54).

4.6 Crossed magnetic and electric fields

The case of crossed fields is much more difficult to handle and no closed form or single sum representation of the energy-dependent Green function is known. Therefore we have to establish another practicable method to evaluate the Laplace transform of the time-dependent kernel. What makes this problem so different from the case of parallel fields?

Even for $\mathbf{r} = \mathbf{r}' = \mathbf{0}$, the exponent has terms involving $t \cot(\omega_L t)$ and $t^2 \cot(\omega_L t)$ which give rise to essential singularities of the propagator at times $t = n\pi/\omega_L$, where $n \in \mathbf{N}_+$. We will restrict our discussion mainly to the total current, which is given (up to a constant factor) by the imaginary part of the Green function at $\mathbf{r} = \mathbf{r}' = \mathbf{0}$. For exactly orthogonal fields, the $t^3 F_{\parallel}$ term in the exponent vanishes and the asymptotic behavior changes. This is of great importance for choosing a quickly converging path of integration. For orthogonal fields the integrand of the Laplace transform reads

$$e^{iEt/\hbar} G_{\mathbf{E} \times \mathbf{B}}(\mathbf{r} = \mathbf{0}, t; \mathbf{r}' = \mathbf{0}, 0) = -\frac{ie^{-i3\pi/4} m \omega_L}{2\pi \hbar^2 \sin(\omega_L t)} \sqrt{\frac{m}{2\pi \hbar t}} \times \\ \times \exp \left\{ \frac{i}{\hbar} \left(Et - \frac{t F_{\perp}^2}{8m\omega_L^2} + \frac{t^2 F_{\perp}^2}{8m\omega_L} \cot(\omega_L t) \right) \right\}. \quad (4.59)$$

In Figure 4.6 we show a plot of this Green function in the complex t -plane for $B = 0.5$ T and three different electric field strengths. The black lines mark a suitable path of integration. Let us further analyze equation (4.59). The second term in the exponent is linear in it and

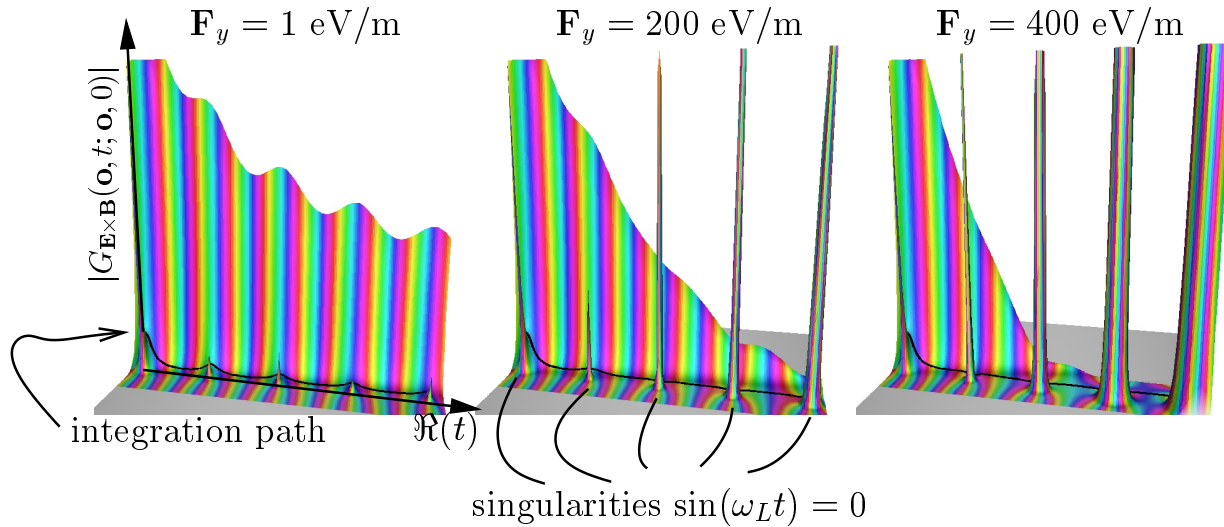


Figure 4.6: Propagator landscape for crossed fields. The phase is encoded in the shading, the height is a measure of the absolute value (highly compressed logarithmic scale). The black line shows a suitable path of integration. Magnetic field: $B = 0.5$ T, electric fields: $\mathbf{F}_z = 0$, $\mathbf{F}_y = 1, 200, 400$ eV/m.

therefore just causes a shift of the energy. The third term is not easily handled, since it is responsible for the essential singularities of the propagator. A naive integration along the real axis is bound to fail. The large-scale asymptotic behavior is determined by the it^2 -term in the exponent. To see this, we replace t by $t = u + iv$ and now have the following structure of the exponent:

$$e^{i(u+iv)^2} = e^{i(u^2-v^2)} e^{-2uv}. \quad (4.60)$$

Along the real axis ($u > 0$) the kernel becomes suppressed, whereas for a negative imaginary part ($v < 0$) the kernel becomes large. Since we have to start our integration at $t = 0$, the limit $t \rightarrow 0$ is of special importance. First let us note that the singularity in the exponent is absent for $t \rightarrow 0$, since $\lim_{t \rightarrow 0} t^2 \cot(\omega_L t) = 0$. For purely imaginary times ($u = 0$), the exponent is real-valued ($\cot(i\omega_L v) = -i \coth(\omega_L v)$) and the integrand becomes

$$e^{Ev/\hbar} G_{\mathbf{E} \times \mathbf{B}}(\mathbf{r} = \mathbf{o}, t = iv; \mathbf{r}' = \mathbf{o}, 0) = \frac{im\omega_L}{2\pi\hbar^2 \sinh(\omega_L v)} \sqrt{\frac{m}{2\pi\hbar(-v)}} \times \\ \times \exp \left\{ \frac{1}{\hbar} \left(-Ev + \frac{vF_{\perp}^2}{8m\omega_L^2} - \frac{v^2 F_{\perp}^2}{8m\omega_L} \coth(\omega_L v) \right) \right\}. \quad (4.61)$$

Since the total current is given by the imaginary part of the Green function, we can conclude that a path along the negative imaginary axis does not affect the final result, since it yields only real-valued contributions. Therefore we can shift the starting point of the integration from $(u = 0, v = 0)$ to the negative imaginary axis to $(0, v_{\text{start}})$. To determine a good value for v_{start} we notice that for $v \rightarrow 0$ the integrand goes to $+\infty$. On

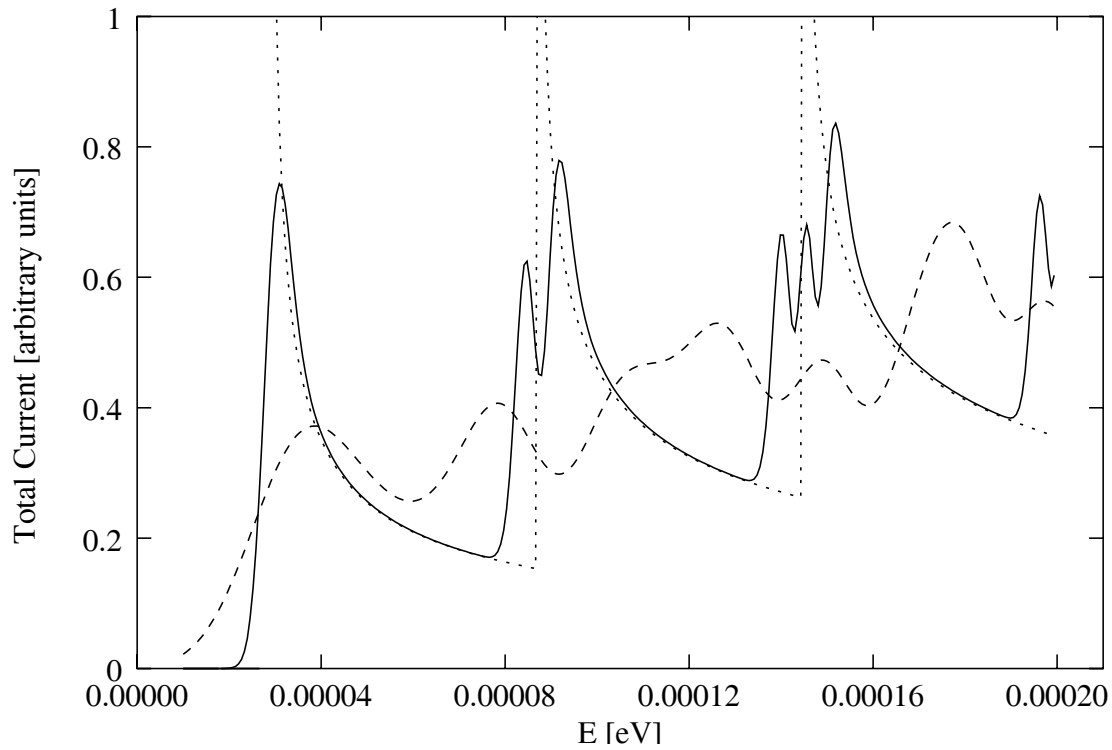


Figure 4.7: The transition from a weak electric field to a stronger electric field is shown. Parameter: Magnetic field; $B = 0.5$ T, parallel electric field: $\mathbf{F}_z = 0$, perpendicular electric field: $\mathbf{F}_y = (1, 100, 400)$ eV/m (dotted, solid, and dashed line respectively).

the other hand for $v \rightarrow -\infty$ the function increases without bounds. No further poles are present along the imaginary axis and therefore the function must become minimal for some value of $v \in]0, -\infty[$. In Figure 4.6 we can see this behavior quite clearly. Therefore the condition

$$\left. \frac{\partial G_{\mathbf{E} \times \mathbf{B}}(\mathbf{o}, t = iv; \mathbf{o}, 0)}{\partial v} \right|_{v=v_{\text{start}}} = 0 \quad (4.62)$$

determines the starting point of the integration path. From this point the path goes parallel to the real axis, until the absolute value of the kernel drops several orders of magnitude. In Figure 4.7 we plot the resulting current distribution for different values of the electric field. These plots illustrate the transition from a purely magnetic field dominated behavior to a electric field regime. The magnetic-field regime was discussed before in Section 4.5. For the electric field, the stair-case structure of the current is related to the interference phenomena in the linear force field discussed in Chapter 2. In [BKK02] we discuss these features in more detail and comment on their connection to closed orbit theory [PD93].

Chapter 5

Currents in electric and magnetic fields for two-dimensional systems

This chapter is devoted to a detailed analysis of the two-dimensional Green function in the presence of static magnetic and electric fields. Exact analytic results are obtained for the total current in perpendicular electric and magnetic fields. The two-dimensional current is directly proportional to the electronic density of states (DOS). Considerable interest exists in the DOS, since thermal, magnetic and electrical properties of two-dimensional electron gases can be calculated with the help of the DOS. Based on our new results for the DOS, a simple single-electron model for the conductivity in a two-dimensional degenerate electron gas is established. We directly apply this model to the quantum Hall effect and point out connections to experimental results, which can be explained within this model.

5.1 Two-dimensional Green function for crossed magnetic and electric fields

The electronic density of states in a purely magnetic field is given in the last chapter and reads

$$n_{\mathbf{B}}^{(2D)}(E) = \frac{eB}{2\pi\hbar} \sum_{k=0}^{\infty} \delta(E - \hbar\omega_L[2k + 1]). \quad (5.1)$$

We already related the density of states to the imaginary part of the Green function at the origin via equation (3.26),

$$n(E) = -\frac{1}{\pi} \Im [G(\mathbf{r} = \mathbf{o}, \mathbf{r}' = \mathbf{o}; E)]. \quad (5.2)$$

In the presence of an additional electric field, the divergence of the current at the Landau levels with energy $E = (2n + 1)\hbar\omega_L$, $n \in \mathbf{N}_0$ is lifted. The number of newly formed peaks is related to the Landau level: One peak for the first level ($k = 0$), two peaks for the second level ($k = 1$) and so on. Fabrikant sees a similar splitting in a three dimensional

system (see [Fab91], Figure 5), but does not investigate this issue further. We will show in this chapter that the elimination of the degeneracy and the broadening of the δ -array given in equation (5.1) is already present in a two dimensional system (see Figure 5.1). The next two sections cover different ways to obtain the DOS from the corresponding two-dimensional Green function for crossed fields.

5.1.1 Total current (generating function method)

We start with the time-dependent Green function for orthogonal fields at the origin $\mathbf{r} = \mathbf{r}' = \mathbf{o}$ given by equation (4.17) after removing the one dimensional parallel-field propagator:

$$e^{iEt/\hbar} G_{\mathbf{E} \times \mathbf{B}}^{(2D)}(\mathbf{o}, t; \mathbf{o}, 0) = -\frac{m\omega_L \Theta(t)}{2\pi\hbar^2 \sin(\omega_L t)} \exp \left\{ \frac{i}{\hbar} \left(\left[E - \frac{F_{\perp}^2}{8m\omega_L^2} \right] t + \frac{t^2 F_{\perp}^2}{8m\omega_L} \cot(\omega_L t) \right) \right\}. \quad (5.3)$$

Again, we transform this expression into a sum over Laguerre polynomials using Theorem 4, page 39, and obtain

$$e^{iEt/\hbar} G_{\mathbf{E} \times \mathbf{B}}^{(2D)}(\mathbf{o}, t; \mathbf{o}, 0) = -\frac{im\omega_L}{\pi\hbar^2} \sum_{k=0}^{\infty} e^{-\gamma^2 t^2 / (2\hbar^2)} L_k^{(0)}(\gamma^2 t^2 / \hbar^2) \times \\ \times \exp \left\{ \frac{it}{\hbar} \left[E - \gamma^2 / (2\hbar\omega_L) - (2l + 1)\hbar\omega_L \right] \right\} \Theta(t), \quad (5.4)$$

with

$$\gamma^2 = \frac{F_{\perp}^2 \hbar}{4m\omega_L} = \frac{F_{\perp}^2 \hbar}{2eB}. \quad (5.5)$$

Next we switch to the energy-dependent Green function by integrating over t . Since we are only interested in the imaginary part of the energy-dependent Green function, we can use the identity

$$\Im \left[\int_0^{\infty} dt f(t) \right] = \frac{1}{2i} \int_{-\infty}^{\infty} dt f(t), \quad (5.6)$$

which holds provided that $f(-t) = -f(t)^*$. Two integral formulae involving Laguerre and Hermite polynomials are useful in this context. The first formula is given in [Buc53], page 149, equation (15b):

$$\int_{-\infty}^{\infty} dx e^{-x^2/2+ixy} L_k^{(0)}(x^2) = [\text{He}_k(y)]^2 \frac{\sqrt{2\pi}}{k!} e^{-y^2/2}. \quad (5.7)$$

We will also use the orthogonality of the Hermite-polynomials $\text{He}_k(x)$, [Buc53], page 149, equation (15c)

$$\int_{-\infty}^{\infty} dx e^{-x^2/2} \text{He}_m(x) \text{He}_l(x) = \sqrt{2\pi} n! \delta_{m,l}. \quad (5.8)$$

(Remark: $H_k(x) = 2^{k/2} \text{He}_k(x\sqrt{2})$, see also [AS65], (22.5.58-59)). The imaginary part of the Green function is therefore given by

$$\Im \left[G_{\mathbf{E} \times \mathbf{B}}^{(2D)}(\mathbf{o}, \mathbf{o}; E) \right] = -\frac{m\omega_L}{2\pi\hbar^2} \sum_{k=0}^{\infty} \int_{-\infty}^{\infty} dt e^{-\gamma^2 t^2 / (2\hbar^2) - itE_k / \hbar} L_k^{(0)}(\gamma^2 t^2 / \hbar^2) \quad (5.9)$$

$$= -\frac{m\omega_L}{\sqrt{2\pi}\hbar\gamma} \sum_{n=0}^{\infty} \frac{1}{k!} e^{-E_k^2 / (2\gamma^2)} [\text{He}_k(E_k / \gamma)]^2 \quad (5.10)$$

$$= \sum_{k=0}^{\infty} \Im \left[G_{\mathbf{E} \times \mathbf{B}, k}^{(2D)}(\mathbf{o}, \mathbf{o}; E) \right], \quad (5.11)$$

where

$$E_k = [E - \gamma^2 / (2\hbar\omega_L) - (2k + 1)\hbar\omega_L]. \quad (5.12)$$

The contribution of each Landau level integrated over energy-space is also readily available. Noting that

$$\int_{-\infty}^{\infty} dx \int_{-\infty}^{\infty} dy e^{-x^2/2 + ixy} L_n^{(0)}(x^2) = 2\pi, \quad (5.13)$$

we get for each Landau level

$$\int_{-\infty}^{\infty} dE \Im \left[G_{\mathbf{E} \times \mathbf{B}, k}^{(2D)}(\mathbf{o}, \mathbf{o}; E) \right] = -\frac{m\omega_L}{\hbar} = -\frac{eB}{2\hbar}. \quad (5.14)$$

The density of states becomes:

$$n_{\mathbf{E} \times \mathbf{B}}^{(2D)}(E) = \sum_{k=0}^{\infty} n_{\mathbf{E} \times \mathbf{B}, k}^{(2D)}(E) = \frac{m\omega_L}{\sqrt{2\pi}\pi\hbar\gamma} \sum_{k=0}^{\infty} \frac{e^{-E_k^2 / (2\gamma^2)}}{k!} [\text{He}_k(E_k / \gamma)]^2. \quad (5.15)$$

Also, the energy-integrated DOS of the k th Landau level is given by

$$\int_{-\infty}^{\infty} dE n_{\mathbf{E} \times \mathbf{B}, k}^{(2D)}(E) = \frac{eB}{h}, \quad (5.16)$$

where $h = 2\pi\hbar$ denotes Planck's constant. The explicit expressions for the first two Landau levels read

$$n_{\mathbf{E} \times \mathbf{B}, k=0}^{(2D)}(E) = \frac{m\omega_L}{\pi\hbar\gamma\sqrt{2\pi}} \exp\left(-\left[E - \frac{\gamma^2}{2\hbar\omega_L} - \hbar\omega_L\right]^2 / (2\gamma^2)\right) \quad (5.17)$$

$$n_{\mathbf{E} \times \mathbf{B}, k=1}^{(2D)}(E) = \frac{m\omega_L \left[E - \frac{\gamma^2}{2\hbar\omega_L} - 3\hbar\omega_L\right]^2}{\pi\hbar\gamma^3\sqrt{2\pi}} \exp\left(-\left[E - \frac{\gamma^2}{2\hbar\omega_L} - 3\hbar\omega_L\right]^2 / (2\gamma^2)\right). \quad (5.18)$$

The reader may have noticed a close similarity between the expressions for the electronic DOS and the one-dimensional harmonic oscillator eigenfunctions. Indeed, the introduction of harmonic oscillator eigenstates $u_k(\xi)$ and their absolute value squared $|u_k(\xi)|^2$ given by

$$u_k(\xi) = \frac{1}{\pi^{1/4}\sqrt{k!}} e^{-\xi^2/2} \text{He}_k(\sqrt{2}\xi), \quad \text{and} \quad |u_k(\xi)|^2 = \frac{1}{\sqrt{\pi}k!} e^{-\xi^2} [\text{He}_k(\sqrt{2}\xi)]^2, \quad (5.19)$$

simplifies the expression of the DOS for the k th Landau level to

$$n_{\mathbf{E} \times \mathbf{B}, k}(E) = \frac{eB}{\sqrt{2}h\gamma} |u_k(\xi)|^2, \quad (5.20)$$

where

$$\xi = \frac{E_k}{\sqrt{2}\gamma} = \frac{E - \gamma^2/(2\hbar\omega_L) - (2k+1)\hbar\omega_L}{\sqrt{2}\gamma}. \quad (5.21)$$

The oscillator eigenfunctions are “visible” as a function of energy and not in position space. Next we discuss another method to evaluate the DOS (or total current). This second method employs linear canonical transformations that shed light on the underlying structure and the appearance of harmonic oscillator functions.

5.1.2 Total current (canonical transformation method)

For an elegant approach to the Green function we use the concept of linear canonical transformations. A linear canonical transformation (LCT) maps the position and momentum operators (\mathbf{x}, \mathbf{p}) into new operators $(\tilde{\mathbf{x}}, \tilde{\mathbf{p}})$ that also fulfill the canonical commutation relation $[\mathbf{x}_i, \mathbf{p}_j] = [\tilde{\mathbf{x}}_i, \tilde{\mathbf{p}}_j] = i\hbar\delta_{i,j}$. We want to find a LCT \mathbf{U} that splits the original Hamiltonian \mathbf{H} into several parts $\mathbf{H} \rightarrow \mathbf{H}' = \mathbf{U}^\dagger \circ \mathbf{H} \circ \mathbf{U} = \mathbf{H}_1 + \mathbf{H}_2$ which commute: $[\mathbf{H}_1, \mathbf{H}_2] = 0$. This procedure provides more insight into the structure and solution of the problem. The spectrum of the Hamiltonian is not affected by the LCT, since the transformation is unitary. We then construct the propagators of the Hamiltonians $\mathbf{H}_1, \mathbf{H}_2$ and get the propagator of the total Hamiltonian \mathbf{H}' by multiplying both propagators. Eventually we transform the propagator back to the original representation.

Linear canonical transformation of the Hamiltonian

For the case of crossed fields the Hamiltonian in two dimensions reads (as always $\omega_L = \frac{eB}{2m}$)

$$\mathbf{H} = \frac{\mathbf{p}_x^2 + \mathbf{p}_y^2}{2m} + \frac{1}{2}m\omega_L^2(x^2 + y^2) + x\mathbf{F}_x + y\mathbf{F}_y - \mathbf{p}_y x\omega_L + \mathbf{p}_x y\omega_L. \quad (5.22)$$

The first LCT maps $(\mathbf{r}_i, \mathbf{p}_i)$ to $(\tilde{\mathbf{r}}_i = \sqrt{m\omega_L}\mathbf{r}_i, \tilde{\mathbf{p}}_i = \frac{1}{\sqrt{m\omega_L}}\mathbf{p}_i)$. The transformed Hamiltonian \mathbf{H}_{LCT1} has the form

$$\mathbf{H}_{LCT1} = (\tilde{\mathbf{p}}_x^2 + \tilde{\mathbf{p}}_y^2 + \tilde{x}^2 + \tilde{y}^2)\frac{\omega_L}{2} - \tilde{\mathbf{p}}_y\tilde{x}\omega_L + \tilde{\mathbf{p}}_x\tilde{y}\omega_L + \frac{\tilde{x}\mathbf{F}_x + \tilde{y}\mathbf{F}_y}{\sqrt{m\omega_L}}. \quad (5.23)$$

The second LCT is given in matrix notation by

$$\begin{pmatrix} \tilde{\tilde{x}} \\ \tilde{\tilde{y}} \\ -\tilde{\tilde{\mathbf{p}}}_x \\ -\tilde{\tilde{\mathbf{p}}}_y \end{pmatrix} = \frac{1}{\sqrt{2}} \begin{pmatrix} 1 & 0 & 0 & -1 \\ 1 & 0 & 0 & 1 \\ 0 & 1 & 1 & 0 \\ 0 & -1 & 1 & 0 \end{pmatrix} \begin{pmatrix} \tilde{x} \\ \tilde{y} \\ -\tilde{\mathbf{p}}_x \\ -\tilde{\mathbf{p}}_y \end{pmatrix}, \quad (5.24)$$

and the transformed Hamiltonian becomes

$$\mathbf{H}_{LCT2} = (\tilde{\mathbf{p}}_y^2 + \tilde{y}^2)\omega_L + \frac{(\tilde{x} + \tilde{y})\mathbf{F}_x + (\tilde{\mathbf{p}}_y - \tilde{\mathbf{p}}_x)\mathbf{F}_y}{\sqrt{2m\omega_L}}. \quad (5.25)$$

Setting $\mathbf{F}_y = 0$ (this can be achieved by rotating the coordinate system, alternatively we could use a third LCT) and introducing

$$c = -\mathbf{F}_x / (2\omega_L \sqrt{2m\omega_L}), \quad (5.26)$$

we can further simplify the expression for \mathbf{H}_{LCT2} to

$$\mathbf{H}_{LCT2} = \omega_L(\tilde{\mathbf{p}}_y^2 + (\tilde{y} - c)^2) - 2c\omega_L\tilde{x} - \omega_L c^2. \quad (5.27)$$

We have reached our goal to have two commuting Hamiltonians, which are given by

$$\mathbf{H}_{LCT2,1} = \omega_L(\tilde{\mathbf{p}}_y^2 + (\tilde{y} - c)^2) - \omega_L c^2, \quad \text{and} \quad (5.28)$$

$$\mathbf{H}_{LCT2,2} = -2c\omega_L\tilde{x}. \quad (5.29)$$

The transformed propagator

It is obvious that the Hamiltonian $\mathbf{H}_{LCT2,1}$ is closely related to the harmonic oscillator. The propagator of a harmonic oscillator

$$\mathbf{H}_{SHO} = \frac{p^2}{2m} + \frac{1}{2}m\omega^2 x^2 \quad (5.30)$$

is conveniently expressed in terms of the energy eigenfunctions $u_k(\xi)$ (see equation (5.19)):

$$K_{SHO}(x, t|x', 0) = \sum_{k=0}^{\infty} \psi_{SHO,k}^*(x) \psi_{SHO,k}(x') e^{iE_k t/\hbar} \quad (5.31)$$

$$= \sqrt{\frac{m\omega}{\hbar}} \sum_{k=0}^{\infty} u_k\left(x\sqrt{\frac{m\omega}{\hbar}}\right) u_k^*\left(x'\sqrt{\frac{m\omega}{\hbar}}\right) e^{i(k+1/2)\omega t}. \quad (5.32)$$

For the slightly modified harmonic oscillator $\mathbf{H}_{LCT2,1}$ we obtain for the unshifted case ($c = 0$)

$$K_{1,c=0}(y, t|y', 0) = \frac{1}{\sqrt{\hbar}} \sum_{k=0}^{\infty} u_k\left(\frac{y}{\sqrt{\hbar}}\right) u_k^*\left(\frac{y'}{\sqrt{\hbar}}\right) e^{i(2k+1)\omega_L t}. \quad (5.33)$$

For $c \neq 0$, we have to shift the energy and the y -coordinate:

$$K_1(y, t|y', 0) = \frac{1}{\sqrt{\hbar}} \sum_{k=0}^{\infty} u_k\left(\frac{y-c}{\sqrt{\hbar}}\right) u_k^*\left(\frac{y'-c}{\sqrt{\hbar}}\right) e^{-i(2k+1)\omega_L t + i\omega_L c^2 t/\hbar}. \quad (5.34)$$

The propagator assigned to $\mathbf{H}_{LCT2,2}$ is given by (see also equation (3.32) or [Kra00])

$$K_2(x, t|x', 0) = \exp\left\{\frac{2ic\omega_L x t}{\hbar}\right\} \delta(x - x'). \quad (5.35)$$

Thus the combined propagator assigned to \mathbf{H}_{LCT2} in the $(\tilde{\mathbf{r}}, \tilde{\mathbf{p}})$ system becomes

$$\tilde{K}(\tilde{x}, \tilde{y}, t|\tilde{x}', \tilde{y}', 0) = K_1(\tilde{y}, t|\tilde{y}', 0) K_2(\tilde{x}, t|\tilde{x}', 0). \quad (5.36)$$

Transform back to the original representation

Now we have to reverse the two LCTs in order to switch back from $(\tilde{\mathbf{r}}, \tilde{\mathbf{p}})$ -coordinates to the original (\mathbf{r}, \mathbf{p}) -representation. The integral kernel for the second LCT is derived in ([Kra00]) and reads

$$\begin{aligned} \tilde{K}(\tilde{x}, \tilde{y}, t | \tilde{x}', \tilde{y}', 0) &= \frac{1}{2\pi\hbar} \iint dq_2 dw_2 \exp\left(i \frac{-\tilde{y}q_2 + \tilde{y}'w_2}{\hbar}\right) \times \\ &\times \tilde{K}\left(\frac{1}{\sqrt{2}}(\tilde{x} - q_2), \frac{1}{\sqrt{2}}(\tilde{x} + q_2), t \middle| \frac{1}{\sqrt{2}}(\tilde{x}' - w_2), \frac{1}{\sqrt{2}}(\tilde{x}' + w_2), 0\right) \end{aligned} \quad (5.37)$$

For the first LCT we get

$$K(x, y, t | x', y', 0) = m\omega_L \tilde{K}(\sqrt{m\omega_L}x, \sqrt{m\omega_L}y, t | \sqrt{m\omega_L}x', \sqrt{m\omega_L}y', 0). \quad (5.38)$$

Imaginary part of the Green function at the origin

We set $(x, y) = (x', y') = (0, 0)$, since we are only interested in the total current. This also implies $(\tilde{x}, \tilde{y}) = (\tilde{x}', \tilde{y}') = (0, 0)$ and therefore we have

$$K(0, 0, t | 0, 0, 0) = \sqrt{2}m\omega_L \int_{-\infty}^{\infty} dw_2 K_1\left(\frac{-w_2}{\sqrt{2}}, t \middle| \frac{-w_2}{\sqrt{2}}, 0\right) K_2\left(\frac{w_2}{\sqrt{2}}, t \middle| \frac{w_2}{\sqrt{2}}, 0\right). \quad (5.39)$$

We also took advantage of the delta function in K_2 which enforces $(w_2 - q_2)\sqrt{2} = 0$. The imaginary part of the energy-dependent Green function is given by

$$\begin{aligned} \Im[G(0, 0; 0, 0; E)] &= \frac{1}{2\pi\hbar} \frac{1}{2i} \frac{i}{\hbar} \frac{\sqrt{2}}{\sqrt{\hbar}} m\omega_L \int_{-\infty}^{\infty} dw_2 \int_{-\infty}^{\infty} dt \times \\ &\times \sum_{k=0}^{\infty} \left| u_k \left(\frac{-w_2 - \sqrt{2}c}{\sqrt{2}\hbar} \right) \right|^2 e^{it[-(2k+1)\hbar\omega_L + \omega_L c^2 + \sqrt{2}c\omega_L w_2 + E]/\hbar} \end{aligned} \quad (5.40)$$

The integration over t gives another delta function, since

$$2\pi\hbar\delta(x) = \int_{-\infty}^{\infty} dt e^{ixt/\hbar}. \quad (5.41)$$

Thus we get rid of the time integration

$$\begin{aligned} \Im[G(0, 0; 0, 0; E)] &= \frac{m\omega_L 2\sqrt{2}\pi\hbar}{4\pi\hbar\sqrt{\hbar}\hbar} \int_{-\infty}^{\infty} dw_2 \times \\ &\times \sum_{k=0}^{\infty} \left| u_k \left(\frac{-w_2 - \sqrt{2}c}{\sqrt{2}\hbar} \right) \right|^2 \delta[-(2k+1)\hbar\omega_L + \omega_L c^2 + \sqrt{2}c\omega_L w_2 + E]. \end{aligned} \quad (5.42)$$

Now we can perform the remaining integration over w_2

$$\Im[G(0, 0; 0, 0; E)] = \frac{m\omega_L}{2\sqrt{\hbar}\hbar} \frac{1}{c\omega_L} \sum_{k=0}^{\infty} \left| u_k \left(\frac{E - (2k+1)\hbar\omega_L + \omega_L c^2 - 2\omega_L c^2}{2\sqrt{\hbar}\omega_L c} \right) \right|^2. \quad (5.43)$$

Eliminating c in favor of γ yields

$$\Im[G(0, 0; 0, 0; E)] = -\frac{m\omega_L}{\sqrt{2}\gamma\hbar} \sum_{k=0}^{\infty} \left| u_k \left(\frac{E - (2k+1)\hbar\omega_L - \frac{\gamma^2}{2\hbar\omega_L}}{-\sqrt{2}\gamma} \right) \right|^2. \quad (5.44)$$

We have obtained the same expression as before by using the generating function method (equation (5.20)). However, the underlying harmonic oscillator and the transformation of the conventional energy-eigenfunctions in coordinate-space to functions of the energy are shown quite clearly. The same transformations may be applied to the operators $\mathbf{x}(t), \mathbf{p}(t)$. The Ehrenfest theorem states, that the classical equation of motion gives the same time evolution as the expectation values of the quantum mechanical operators. However, we have to be careful in interpreting results in different coordinate frames because they are related to different Green functions.

5.2 Properties of the two-dimensional density of states

Since $\text{He}_k(z)$ has k simple zeroes on the real z -axis (including $z = 0$ for n odd), each Landau level is split into $k + 1$ levels. From the normalization of the harmonic oscillator eigenfunctions we immediately obtain the sum rule for each Landau level (see equation (5.20)). The envelope of each Landau level is given by a Gaussian with half-width γ defined in equation (5.5). The parameter γ is independent of the electron mass. However, for the same electric field strength (and therefore γ) higher Landau levels will have a larger effective width since the exponential term $e^{-E^2/(2\gamma^2)}$ is multiplied with a polynomial of degree k . The spacing of the Landau levels is given by $2\hbar\omega_L$ and is independent of the electric field. For weak electric fields and strong magnetic fields ($\gamma \ll 2\hbar\omega_L$) almost no overlap between adjacent Landau levels exists and the energy integrated contribution over a single Landau level gives the same quantization as the purely magnetic field of equation (5.1). Between two Landau levels the DOS drops off very fast due to the exponential decay. However, there is a critical electric field, where the DOS of two Landau levels begin to overlap and the DOS does not vanish any more between the levels. The decay constant γ depends linearly on the electric field $F_{\perp} = eE_{\perp}$ and is proportional to $B^{-1/2}$ as a function of the magnetic field. Sometimes it is useful to normalize the level width to the Landau level spacing. In this case we get

$$\frac{\text{level width } \gamma}{\text{Landau level spacing } 2\hbar\omega_L} = \frac{E_{\perp} m}{\sqrt{2}\sqrt{\hbar} e B^{3/2}} \propto E_{\perp} B^{-3/2}. \quad (5.45)$$

Plots of the density of states are shown in Figure 5.1. We will comment on the experimental evidence for such a dependence on the external fields in Section 5.4.3.

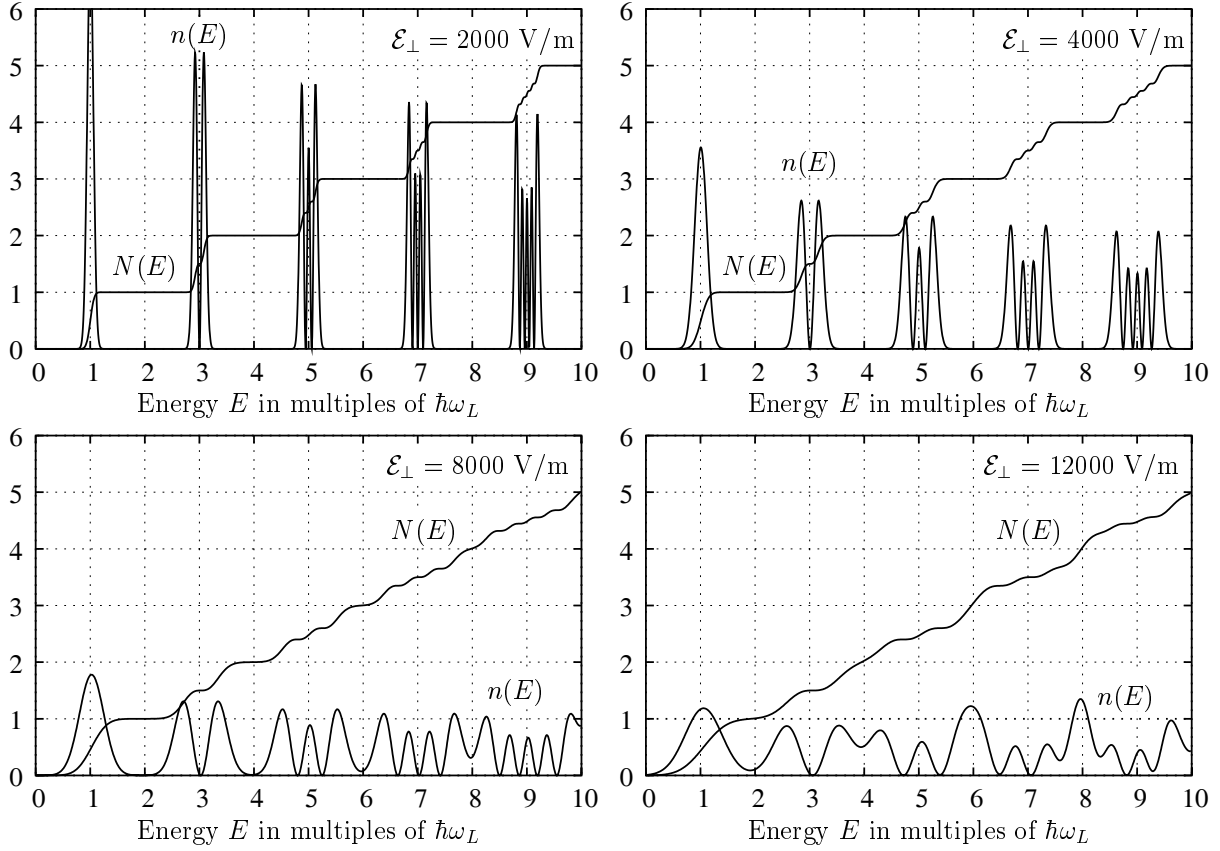


Figure 5.1: Two-dimensional density of states (DOS) $n(E)$ (in units of $eB/(2\pi\hbar^2\omega_L)$) and integrated DOS $N(E)$ (in units of $eB/(2\pi\hbar)$) at four different electric fields $\mathbf{E} = 2000, 4000, 8000, 12000$ V/m and for a magnetic field $B = 5$ T as a function of the scaled energy $E/(\hbar\omega_L)$ according to eq. (5.15). Near the k th Landau level at $E = (2k + 1)\hbar\omega_L$, the DOS renders the probability distribution of a one-dimensional harmonic oscillator in the k th eigenstate.

5.2.1 The energy integrated DOS

Another useful quantity is the integrated density of states up to a certain energy E . We will assign the symbol $N(E)$ to the integrated DOS (or shorter IDOS):

$$N(E) = \int_{-\infty}^E dE' n(E'). \quad (5.46)$$

We can express the integral analytically with the help of the auxiliary function

$$\mathcal{N}_k(\epsilon) = \frac{1}{k!} \int_{-\infty}^{\epsilon} d\xi e^{-\xi^2/2} [\text{He}_k(\xi)]^2 \quad (5.47)$$

$$= \sqrt{\frac{\pi}{2}} \left[1 + \text{erf} \left(\frac{\epsilon}{\sqrt{2}} \right) \right] - \sum_{n=0}^{k-1} \frac{1}{(n+1)!} \text{He}_n(\epsilon) \text{He}_{n+1}(\epsilon) e^{-\epsilon^2/2}. \quad (5.48)$$

A proof of this relation is given in Appendix C. Using this function we obtain for the integrated DOS

$$N(E) = \int_{-\infty}^E dE' n(E') = \frac{m\omega_L}{\sqrt{2\pi\pi\hbar}} \sum_{k=0}^{\infty} \mathcal{N}_k[E_k/\gamma], \quad (5.49)$$

where $E_k = E - \gamma^2/(2\hbar\omega_L) - (2k+1)\hbar\omega_L$ as before. A plot of the integrated DOS $N(E)$ and the DOS $n(E)$ for fixed magnetic field $B = 5$ T and four different electric field strengths is given in Figure 5.1. The broadening of the Landau levels due to the increasing electric field is clearly displayed. The zeroes of the Hermite polynomials are also prominently visible. The integrated DOS shows an extended plateau structure connected to the almost completely vanishing DOS between the Landau levels. At higher electric fields the plateau width shrinks considerably as expected from the discussion of the electric field dependence of the DOS.

To investigate the step height due to the Landau level structure further we compute the integrated DOS for each Landau level independently and split the integration into k intervals given by the distance between adjacent zeroes ξ_j ($j = 1, \dots, k$) of the k th Hermite polynomial. The first interval extends from $]-\infty, \xi_1]$ and the last one from $[\xi_k, +\infty[$. This prescription actually yields the probability to find a particle in the k th harmonic oscillator eigenstate between two nodes of the wave function. For the first Landau level ($k = 0$) we obtain, of course, a value of 1 (normalized by eB/h) for the integrated DOS in the interval from $-\infty$ to $+\infty$:

$$\int_{-\infty}^{+\infty} d\xi |u_0(\xi)|^2 = 1. \quad (5.50)$$

Therefore, no steps in the integrated DOS are present. For the $k = 1$ oscillator eigenstate with one zero at $\xi_1 = 0$, due to parity, both areas are equal to $1/2$:

$$\int_{-\infty}^0 d\xi |u_1(\xi)|^2 = \int_0^{+\infty} d\xi |u_1(\xi)|^2 = \frac{1}{2}. \quad (5.51)$$

The $k = 2$ level is more involved, since it has two nodes in the wave function at $\xi_1 = -1/\sqrt{2}$, $\xi_2 = +1/\sqrt{2}$ and consequently we get three contributions. An analytic evaluation yields (note: e denotes Euler's number, not the electron charge e)

$$\int_{-\infty}^{-1/\sqrt{2}} d\xi |u_2(\xi)|^2 = \frac{1}{\sqrt{2\pi e}} + \frac{1}{2} \operatorname{erfc}(1/\sqrt{2}) = 0.400626 \dots \approx 2/5, \quad (5.52)$$

$$\int_{-1/\sqrt{2}}^{+1/\sqrt{2}} d\xi |u_2(\xi)|^2 = -\frac{2}{\sqrt{2\pi e}} + \operatorname{erf}(1/\sqrt{2}) = 0.198748 \dots \approx 1/5, \quad (5.53)$$

$$\int_{+1/\sqrt{2}}^{+\infty} d\xi |u_2(\xi)|^2 = \int_{-\infty}^{-1/\sqrt{2}} d\xi |u_2(\xi)|^2 = \text{see above.} \quad (5.54)$$

Interestingly, the exact expressions which are represented in terms of error functions and Euler's number, are quite well approximated by very simple fractions. Similar consideration give for $k = 3$ four contributions with weights $0.349992\dots$, $0.150007\dots$, $0.150007\dots$, $0.349992\dots$, that can be approximated by the fractions $7/20$, $3/20$, $3/20$, $7/20$. The influence of these fractions can be seen in all figures. We stop here (however, a further evaluation for higher Landau levels presents no difficulties), since the main structure is already obvious.

5.3 Spin and effective mass

As an example for the application of the density of states we want to study the conductivity in a two-dimensional electron gas in the presence of a magnetic and a perpendicular electric field. In order to connect our results to experiments, we have to include the spin of the electrons. Also we have to take into account that experiments in semiconductors may require the use of an effective mass m^* and even an effective magnetic g -factor, denoted by g^* . We include the spin by considering the density of states for spin up $n_{\uparrow}(E)$ and spin down $n_{\downarrow}(E)$ separately. The Hamiltonian acquires an additional term $\pm g^*/2\mu_B B$, which includes the interaction of the spin with the magnetic field. The effective g^* -factor is by some authors considered to be dependent on B [WTSS92]. However, in our calculations we will assume a constant g^* . The complete effect of the spin is therefore absorbed in a shift of the energy

$$n_{\uparrow}(E) = n(E + g^*/2\mu_B B), \quad (5.55)$$

$$n_{\downarrow}(E) = n(E - g^*/2\mu_B B), \quad (5.56)$$

and the DOS including both spin components reads

$$n_{\uparrow\downarrow}(E) = n(E + g^*/2\mu_B B) + n(E - g^*/2\mu_B B). \quad (5.57)$$

The Landau level spacing is also affected by the introduction of an effective mass m^* , since the (effective) mass enters into the definition of $\omega_L^* = eB/(2m^*)$. The integrated DOS including spin is given (as before) by integrating $n_{\uparrow\downarrow}(E)$ up to the energy E

$$N_{\uparrow\downarrow}(E) = \int_{-\infty}^E dE' n_{\uparrow\downarrow}(E'). \quad (5.58)$$

5.4 Conductivity in the quantum Hall regime

A very interesting system is given by a two-dimensional electron gas in the presence of a strong magnetic field (directed along the z -axis) through which a constant current flows in the x -direction. Under vacuum conditions the current would be deflected in the y -direction by the magnetic field. However, in a solid sample an electric field (or voltage) builds up that is directed perpendicular to the current and the magnetic field. This so-called Hall field exactly counterbalances the deflection due to the magnetic field. The currents and the electric fields are related by the conductivity tensor

$$\begin{pmatrix} \mathbf{j}_x \\ \mathbf{j}_y \end{pmatrix} = \begin{pmatrix} \sigma_{xx} & \sigma_{xy} \\ \sigma_{yx} & \sigma_{yy} \end{pmatrix} \begin{pmatrix} \mathbf{E}_x \\ \mathbf{E}_y \end{pmatrix}. \quad (5.59)$$

Only two matrix elements are independent, since

$$\sigma_{xx} = \sigma_{yy}, \quad \text{and} \quad \sigma_{xy} = -\sigma_{yx} \quad (5.60)$$

holds [GP00]. Next, we will set up a simple model for the conductivity, that relies on the density of states. The density of states and the number of carriers given by the integrated DOS are already ingredients of the standard Drude model for the conductivity in metals. For the extension to a two-dimensional system we follow [GP00] page 566. We use an isotropic one-band model for the conductivity tensor

$$\tilde{\sigma}(E) = \frac{e^2 n_{\uparrow\downarrow}(E) \tau(E)}{m^*} \frac{1}{1 + (\omega_c^* \tau(E))^2} \begin{pmatrix} 1 & -\omega_c^* \tau(E) \\ \omega_c^* \tau(E) & 1 \end{pmatrix}, \quad (5.61)$$

with $\omega_c^* = 2\omega_L^* = eB/(m^*)$. The parameter $\tau(E)$ denotes the relaxation time. However, we still have to integrate this expression over the energy range $] -\infty, E_F]$, where E_F denotes the Fermi energy:

$$\sigma(E_F) = \int_{-\infty}^{E_F} dE \tilde{\sigma}(E). \quad (5.62)$$

The conductivity in the perpendicular field direction is given for $\omega_c^* \tau(E) \gg 1$ by

$$\sigma_{xy}(E_F) = \frac{e}{B} \int_{-\infty}^{E_F} dE \frac{n_{\uparrow\downarrow}(E)}{1 + 1/(\omega_c^* \tau(E))^2} = \frac{e}{B} N_{\uparrow\downarrow}(E_F), \quad (5.63)$$

which involves the integrated DOS $N_{\uparrow\downarrow}(E_F)$. The material-dependent parameters m^* and $\tau(E)$ are not present in the last expression. This situation is completely different in the longitudinal x -direction. Here, we assume a significant contribution to the electronic conductivity only from scattering events near the Fermi energy ($E \approx [E_F - k_B T/2, E_F + k_B T/2]$) and thus obtain

$$\sigma_{xx}(E_F) = \frac{e}{B} \int_{-\infty}^{E_F} dE n_{\uparrow\downarrow}(E) \frac{\omega_c^* \tau(E)}{1 + (\omega_c^* \tau(E))^2} \approx k_B T n_{\uparrow\downarrow}(E_F) \frac{\omega_c^* \tau(E_F)}{1 + (\omega_c^* \tau(E_F))^2} \frac{e}{B}. \quad (5.64)$$

The longitudinal conductivity is proportional to the (non-integrated) DOS $n_{\uparrow\downarrow}(E_F)$ and contains all material-dependent parameters. The (commonly experimentally measured) resistivity is obtained by inverting the conductivity matrix:

$$\rho_{xy}(E_F) = \frac{\sigma_{xy}(E_F)}{\sigma_{xx}(E_F)^2 + \sigma_{xy}(E_F)^2}, \quad \rho_{xx}(E_F) = \frac{\sigma_{xx}(E_F)}{\sigma_{xx}(E_F)^2 + \sigma_{xy}(E_F)^2}. \quad (5.65)$$

If the longitudinal component σ_{xx} vanishes, the simpler relation

$$\rho_{xy}(E_F) = \frac{1}{\sigma_{xy}(E_F)} \quad \text{if } \sigma_{xx}(E_F) = 0 \quad (5.66)$$

holds. Since the density of states vanishes between Landau levels almost completely for $\gamma \ll 2\hbar\omega_L$, the integrated DOS becomes constant in this energy interval and develops plateaus. From this consideration, it is clear that ρ_{xy} is quantized at these plateaus. The unit of quantization is obtained by taking the case, where the Fermi energy E_F lies between the $(k-1)$ th and k th Landau level. Not considering the spin degeneracy for the moment, we have $N(E_F) = keB/h$, $n(E_F) \approx 0$ and therefore

$$\rho_{xy} = \frac{B}{eN(E_F)} = \frac{h}{ke^2}, \quad \text{where } k \in \mathbf{N}_+ \quad (5.67)$$

However, note that in all Landau levels besides the first one the DOS also vanishes at the zeroes of the Hermite-polynomial. Therefore we get additional structures inside the Landau levels at the values given in Section 5.2.1.

5.4.1 Electric field

In our theory the DOS has an explicit dependency on the electric field strength. Experiments are usually carried out in a constant current mode, where the current \mathbf{j}_x along the longitudinal x -direction is kept constant. By inverting the conductivity matrix and setting $\mathbf{j}_y = 0$ (static Hall case), we get

$$\mathbf{E}_x = \rho_{xx}(E_F, B, \mathbf{E}_y) \mathbf{j}_x \quad (5.68)$$

$$\mathbf{E}_y = \rho_{yx}(E_F, B, \mathbf{E}_y) \mathbf{j}_x, \quad (5.69)$$

for given magnetic field B , current density \mathbf{j}_x and Fermi energy E_F . Since the electric Hall field is proportional to the Hall resistivity ρ_{xy} , we have a varying electric field strength outside quantized plateaus. The actual value of the Hall field \mathbf{E}_y may be extracted from the implicit representation in the last equation

$$\mathbf{E}_y = \rho_{yx}(E_F, B, \mathbf{E}_y) \mathbf{j}_x. \quad (5.70)$$

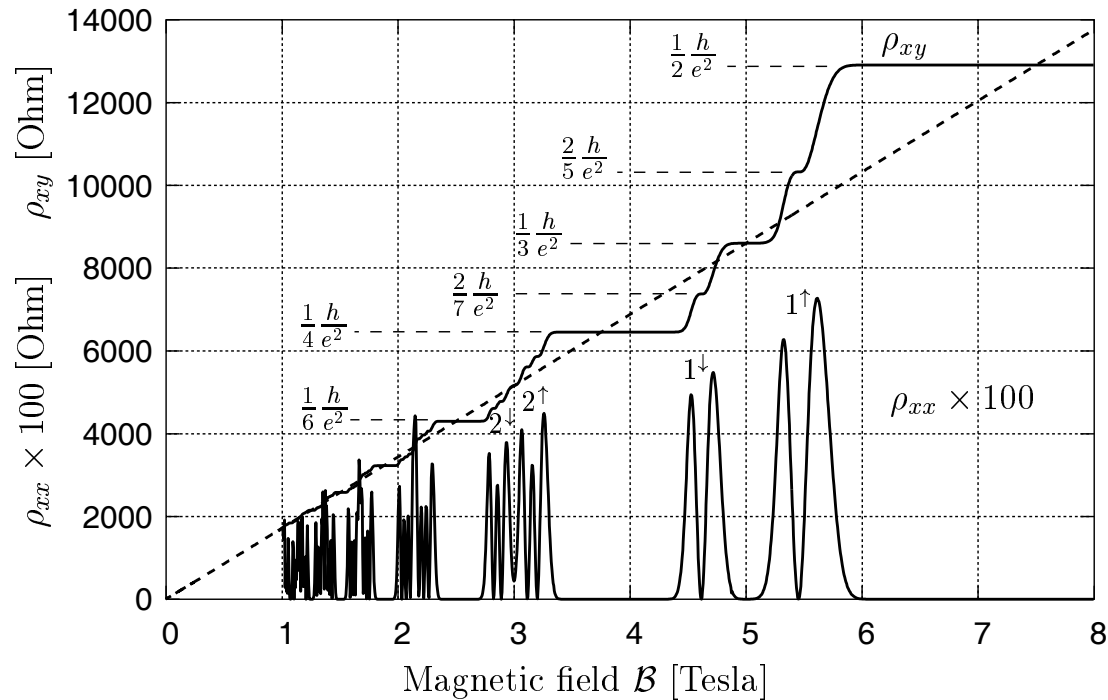


Figure 5.2: Quantum Hall effect at strong magnetic fields ($B > 1$ Tesla) for a non-interacting two-dimensional electron gas. Hall resistance ρ_{xy} and longitudinal resistance ρ_{xx} as a function of the magnetic field B for fixed Fermi energy ($E_F = 0.868$ meV). Effective mass $m^* = 1$, effective g -factor $g^* = \frac{1}{2}$, current density $j_x = 0.2$ A/m, $\tau(E_F) = 10^{-11}$ s, $T = 0.1$ K. The dashed line represents the classical Hall resistance ρ_{xy} with a constant level density. The agreement with experimental results [PTG82] is remarkable.

5.4.2 Prototype calculations of the resistivity

Actual measurements of the Hall resistivity are performed in different materials [PG87]. The original plateaus were seen in Si-MOSFETs [KDP80]. In these materials an applied gate voltage is used to adjust the Fermi energy (and therefore the number of carriers given by the integrated DOS). Klitzing obtained measurements of both resistivity components ρ_{xx} , and ρ_{xy} , as a function of the gate voltage for fixed magnetic field.

Another commonly used type of device is a GaAs-AlGaAs heterostructure. For this material measurements are performed at fixed Fermi energy E_F but varying magnetic field. This makes the interpretation of the curves somewhat more difficult, since a varying magnetic field also implies varying spin shifts and Landau level broadening. A typical plot is shown in Figure 5.2.

5.4.3 Electric field induced breakdown of the quantum Hall effect

For small $\gamma \ll \hbar\omega_L$, the overlap between adjacent Landau levels is negligible, since the DOS drops off exponentially between Landau levels. With increasing electric field, the Landau

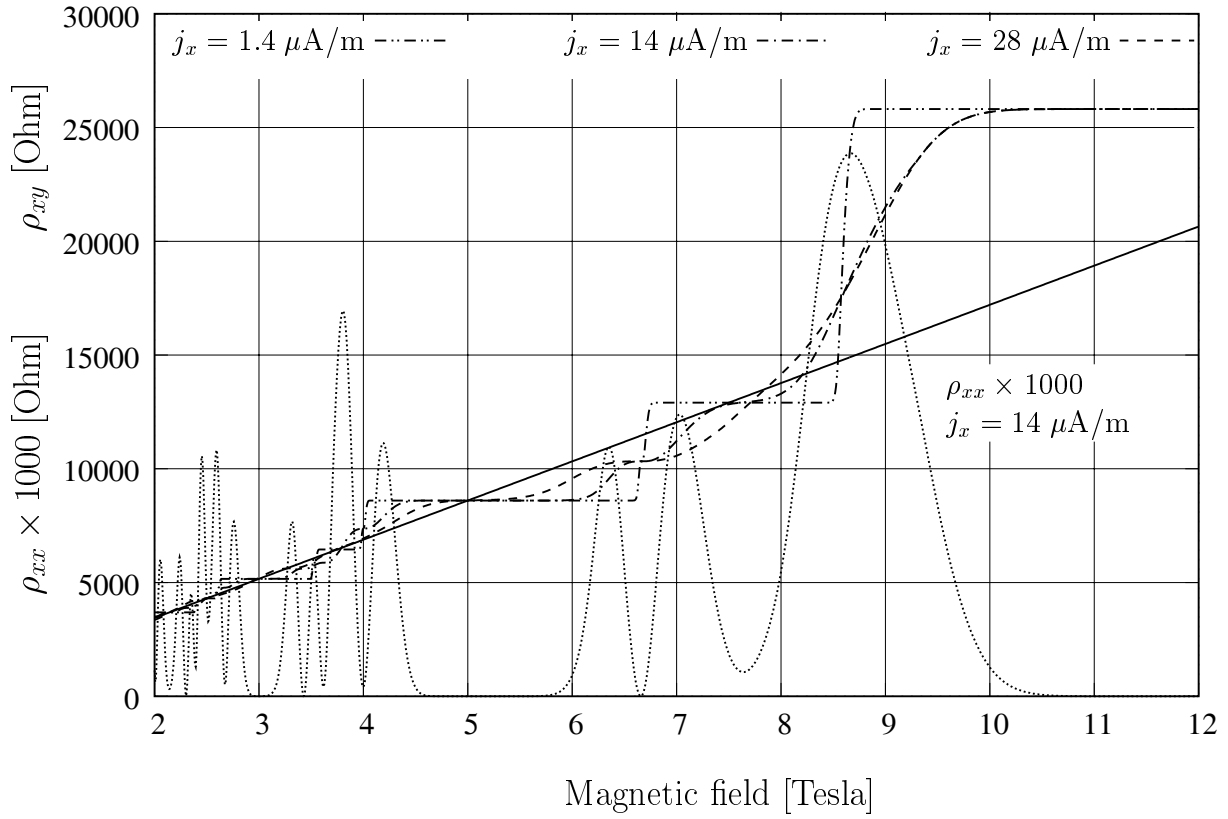


Figure 5.3: Hall resistance ρ_{xy} and longitudinal resistance ρ_{xx} as a function of the magnetic field for a fixed Fermi energy. Curves for three different current densities are shown: $\mathbf{j}_x = (1.4, 14, 28) \mu\text{A}$. Effective mass $m^* = 1$, effective $g = 1.5$, $\tau(E) = 300 \cdot 10^{-12} \text{ s}$, $T = 1.2 \text{ K}$. These values were chosen to match the experimental results reported in [KHN93].

levels become broader and finally coalesce. The classical turning point in the oscillator in equation (5.19) $\xi_k^{\text{tp}} = \sqrt{2k+1}$ provides a practical measure for the width of the DOS. The classically allowed region in energy between two Landau levels $k-1$, k is then given by the ratio

$$\frac{\text{half widths of two levels } \sqrt{2}\gamma(\xi_{k-1}^{\text{tp}} + \xi_k^{\text{tp}})}{\text{level spacing } 2\hbar\omega_L^*} = \frac{m^*}{\sqrt{e\hbar}} \left(\sqrt{2k-1} + \sqrt{2k+1} \right) \frac{E_{\perp}}{B^{3/2}}. \quad (5.71)$$

The overall width of the modulated Landau levels increases with $k^{1/2}$. Note, that the Landau level spacing is also influenced by the effective g^* -factor that shifts the level centers. The half width γ is independent of any mass parameter, whereas m^* enters the definition of the effective Larmor frequency $\omega_L^* = eB/(2m^*)$. Commonly a critical value for the Hall field is experimentally determined by the condition that the longitudinal resistivity σ_{xx} doesn't drop any more below a threshold of about 0.1 Ohm [KHN93]. In [SOK98] Shimada et al. measure a dependence of the critical electric field that is well represented by their

equation (3)

$$E_{\perp,\text{crit}} = \frac{\hbar\omega_c/2 - \gamma_0}{ael_B}, \quad (5.72)$$

where $l_B = (\hbar/(eB))^{1/2}$ denotes the magnetic length and a is a fit parameter $a \approx 38$. This is exactly the result we expect from equation (5.45) for the condition that the DOS should not drop below α times its peak value:

$$E_{\perp,\alpha} = \frac{1}{\sqrt{-\ln(\alpha/2)}} \frac{\hbar\omega_L^*}{el_B}. \quad (5.73)$$

In this derivation we only considered the Gaussian envelope of the DOS and did not take into account the modification due to the Hermite polynomials, which will affect the parameter α and also causes a shift due to different effective width of the two adjacent levels. Calculations including all these effects are, of course, easily possible with the analytic form of the DOS. In Figure 5.3 we show calculations for the resistivity at different current densities \mathbf{j}_x corresponding to different electric field strengths. Note that even and odd indexed plateaus are affected quite differently by the increasing field. This is due to the choice of the effective mass m^* and effective g^* values. Here we show the breakdown of the $i = 2, 4, 6$ levels. Another interesting effect visible in these curves is the emergence of the sublevels in the Landau levels at higher currents due to the broadening of the regions around the zeroes of the DOS.

Chapter 6

Source model for photodetachment in strong electric and magnetic fields

After having discussed the two-dimensional Green function in the previous chapter we return now to three dimensions. There, photodetachment experiments with electrons coming from negative ions are good candidates for the use of the quantum source formalism. Normally, the source region is reasonably localized in position space (the de Broglie wavelength of the emitted particle is considerably larger than the source region which is determined by the size of the electron emitting ion). By shining a laser beam on negative ions, the surplus electrons get detached with a rate determined by the external fields and the initial energy given by the laser energy minus the binding energy of the electron. In principle, a measurement of this rate is directly related to the total current given by the imaginary part of the energy-dependent Green function. From Sections 4.4 and 4.6 we anticipate a non-trivial structure in these currents due to the interplay between the magnetic field singularities of the Landau levels and the smoothing out caused by an electric field (see also Figure 4.7). Unfortunately a direct experimental observation of these features is obscured by several effects. In this chapter we show how to address some of these difficulties within the quantum source approach and we obtain specific predictions for the detachment rate of negatively charged ions.

The two-dimensional electron system treated in the last chapter is also connected to the theoretical description underneath the photodetachment process. Features like substructure inside Landau levels and level broadening due to electric fields are actually observable in three dimensional systems, too.

6.1 Connection to experiments

A description of photodetachment measurements in magnetic and electric fields is given in [BJL78, BIL79]. These authors consider the case of applying a purely magnetic field to a cloud of trapped ions. Sulfur ions are confined in a Penning-type trap, where they move under the influence of the external magnetic field. A laser beam with known frequency

and polarization illuminates the ions and leads to photodetachment of the extra electron. The number of ions before and after the illumination is compared in order to deduce the detachment rate. Two major complications arise in real-world experiments: First, a magnetic field influences the energy levels of the ions and atoms due to the Zeeman splitting. Therefore we have to deal with a superposition of many allowed transitions. The second effect comes from the finite temperature of the ions. Since the ions move in a strong magnetic field ($B \approx 1$ T), they experience in their rest frame an additional electric field perpendicular to the velocity vector and the magnetic field. A first theoretical description combined with a comparison of the theory with experimental data for the case of an external magnetic field is given in [BIL79]. Here, we present a different method to obtain similar (theoretical) results for a purely external magnetic field. We also extend the theory to include additional external electric fields. The influence of additional electric field is under active study and a first preliminary comparison between experimental data and the theory below is given in [YKB03].

6.1.1 Total current at zero temperature

Our starting point is the energy-dependent Green function given by the Laplace transform of equation (4.17). The total current (also referred to as total cross section) of a isotropic point source of unit strength $\sigma_{00}(\mathbf{r}) = \frac{1}{4\pi}\delta(\mathbf{r} - \mathbf{r}')$ at the origin \mathbf{o} reads according to equations (2.40) and (3.40)

$$J(E) = -\frac{1}{2\pi\hbar}\Im[G(\mathbf{o}, \mathbf{o}; E)]. \quad (6.1)$$

We introduce the following notation for the expression we want to calculate:

$$J(E) = -\frac{1}{2\pi\hbar}\Im\left[\int_0^\infty dt f(t, E, \mathbf{F}_\perp, F_\parallel, \mathbf{B})\right], \quad (6.2)$$

where

$$f(t, E, \mathbf{F}_\perp, F_\parallel, \mathbf{B}) = -\frac{m\omega_L e^{-i\pi/4}}{2\pi\hbar^2 \sin(\omega_L t)} \sqrt{\frac{m}{2\pi\hbar t}} \times \\ \times \exp\left\{\frac{i}{\hbar}\left(Et - F_\parallel^2 \frac{t^3}{24m} + F_\perp^2 \left[-\frac{t}{8m\omega_L^2} + \frac{t^2}{8m\omega_L} \cot(\omega_L t)\right]\right)\right\}. \quad (6.3)$$

The electric field component parallel to the magnetic field B is labelled F_\parallel and the perpendicular component F_\perp .

6.1.2 Thermal motion of the ions

Next, we consider the thermal motion of the ions. We will assume a Boltzmann distribution of the ions. The normalized thermal distribution of the momentum of the ions $P(\mathbf{p})$ is

given by

$$P(\mathbf{p}) = \frac{1}{(2\pi M k_B T)^{3/2}} \exp(-p^2/(2M k_B T)), \quad (6.4)$$

where k_B denotes Boltzmann's constant, and M is the mass of the ion. The detachment rate is influenced by the electric and magnetic fields that are present in the rest-frame of the ion. The transformation of the external (laboratory) fields to the rest-frame gives rise to additional fields, i.e. a purely magnetic laboratory field produces an additional electric field in the rest-frame [Jac75]. This field is perpendicular to the momentum of the ions and the magnetic field,

$$\mathbf{F}_\perp(\mathbf{p}) = \mathbf{F}_\perp + \frac{e}{M} \mathbf{p} \times \mathbf{B}. \quad (6.5)$$

The change of the magnetic field is very small in magnitude and therefore neglected. Taking the thermal average over the Boltzmann distributed ion momenta we get

$$J_{\text{average}}(E) = -\frac{1}{2\pi\hbar} \Im \left[\int d^3\mathbf{p} P(\mathbf{p}) \int_0^\infty dt f(t, E, \mathbf{F}_\perp(\mathbf{p}), F_\parallel, \mathbf{B}) \right]. \quad (6.6)$$

6.1.3 Doppler shift of the laser frequency

Another effect of the motion of the ions is the Doppler shift of the laser energy. The energy parameter in the Green function is the difference between the laser energy $\hbar\Omega$ and the binding energy or electron affinity E_A of the extra electron. The Doppler corrected energy difference $\hbar\Omega - E_A$ in the rest frame of the ion is given in leading order by

$$E(\mathbf{p}) = \hbar\Omega \left(1 - \frac{1}{c} \mathbf{v} \cdot \hat{\mathbf{n}} \right) - E_A = [\hbar\Omega - E_A] - \frac{\hbar\Omega}{Mc} \hat{\mathbf{n}} \cdot \mathbf{p}, \quad (6.7)$$

where $\hat{\mathbf{n}}$ denotes the normalized direction of the laser beam. Thus we obtain a further dependency on the momentum of the ions $f(t, E(\mathbf{p}), \mathbf{F}_\perp(\mathbf{p}), F_\parallel, \mathbf{B})$.

6.1.4 Additional electric ac-field

Recent experiments are conducted in the presence of an additional external electric field that is slowly time-varying and oriented parallel to the magnetic field [YKB03]. The detachment-rate measurements extend over many periods of the electric field amplitude and thus we have to average over all parallel electric strengths $F_\parallel(\alpha)$. Using the explicit expression $F_\parallel(\alpha) = F_{\parallel,\text{peak}} \cos(\alpha)$, we have to integrate over the phase-angle α :

$$\begin{aligned} f_{\text{ac}}(t, E(\mathbf{p}), \mathbf{F}_\perp(\mathbf{p}), F_{\parallel,\text{peak}}, \mathbf{B}) &= \frac{1}{2\pi} \int_0^{2\pi} d\alpha f(t, E(\mathbf{p}), \mathbf{F}_\perp(\mathbf{p}), F_\parallel(\alpha), \mathbf{B}) \\ &= J_0 \left\{ F_{\parallel,\text{peak}}^2 \frac{t^3}{48m\hbar} \right\} \exp \left\{ \frac{i}{\hbar} \left(\frac{F_{\parallel,\text{peak}}^2 t^3}{48m} \right) \right\} f(t, E(\mathbf{p}), \mathbf{F}_\perp(\mathbf{p}), F_{\parallel,\text{peak}}, \mathbf{B}). \end{aligned} \quad (6.8)$$

Here, $J_0(x)$ denotes the Bessel function of the first kind and order 0 as defined by [AS65].

6.1.5 Evaluation of the remaining integrals

After collecting all effects that are caused by the motion of the ions, we proceed to actually evaluate the integration over the Boltzmann distributed ion momenta $P(\mathbf{p})$ and obtain a function independent of \mathbf{p} :

$$g(t, E, F_{\perp}, F_{\parallel}, B) = \int d^3\mathbf{p} P(\mathbf{p}) f(t, E(\mathbf{p}), \mathbf{F}_{\perp}(\mathbf{p}), F_{\parallel}, \mathbf{B}). \quad (6.9)$$

Alternatively, the case of the time-varying external electric field yields

$$g_{ac}(t, E, F_{\perp}, F_{\parallel}, B) = \int d^3\mathbf{p} P(\mathbf{p}) f_{ac}(t, E(\mathbf{p}), \mathbf{F}_{\perp}(\mathbf{p}), F_{\parallel, \text{peak}}, \mathbf{B}). \quad (6.10)$$

The explicit form of $g(t, E, F_{\perp}, F_{\parallel}, B)$ is given by

$$g(t, E, F_{\perp}, F_{\parallel}, B) = -e^x e^{-i\pi/4} \frac{m\omega_L}{2\pi\hbar \sin(\omega_L t)} \sqrt{\frac{m}{2\pi\hbar t}} \frac{i\hbar M}{i\hbar M - k_B T m (1 - \omega_L t \cot(\omega_L t))}, \quad (6.11)$$

and the exponent x reads

$$x = -\frac{k_B n_z^2 t^2 T \Omega^2}{2c^2 M} + \frac{i}{\hbar} \left(Et - F_{\parallel}^2 \frac{t^3}{24m} - F_{\perp}^2 \frac{t}{8m\omega_L^2} (1 - \omega_L t \cot(\omega_L t)) - \frac{k_B T t^2 (4\hbar^2 n_y^2 \omega_L^2 \Omega^2 + [2\hbar n_x \omega_L \Omega - cF_{\perp} (1 - \omega_L t \cot(\omega_L t))]^2)}{8c^2 \omega_L^2 (i\hbar M - k_B T m (1 - \omega_L t \cot(\omega_L t)))} \right). \quad (6.12)$$

At a temperature of $T = 0$ the expression for g reduces to the original propagator denoted by f in equation (6.3). At this stage we have only one remaining integration over the time variable t

$$J_{average}(E) = -\frac{1}{2\pi\hbar} \Im \left[\int_0^{\infty} dt g(t) \right]. \quad (6.13)$$

The evaluation of this integral is possible by choosing a suitable path of integration. We can deform the integration path into the complex plane (if we carefully avoid to cross any singularities) and perform the integration numerically. In Figure 6.1 we show typical results for different temperatures of the ions. For one curve we used the same parameter set as in [BIL79], Figure 2. Both curves are in excellent agreement, although they are obtained by quite different methods. Blumberg et al. uses a sum over Landau levels to represent the averaged current, whereas we reduced the calculation to a single integration. The not averaged plots in Figure 4.7 on page 51 show much more details in the substructure of the Landau levels. In the last chapter we saw that these features are directly related to the zeroes of the Hermite polynomials. Even after the averaging the division of the first level due to the zero of the first Hermite polynomial prevails in Figure 6.1. For the second level, the linear dependence of the location of the zeroes on the field strengths tends to wash out the substructure originally visible in the not-averaged plot in Figure 4.7.

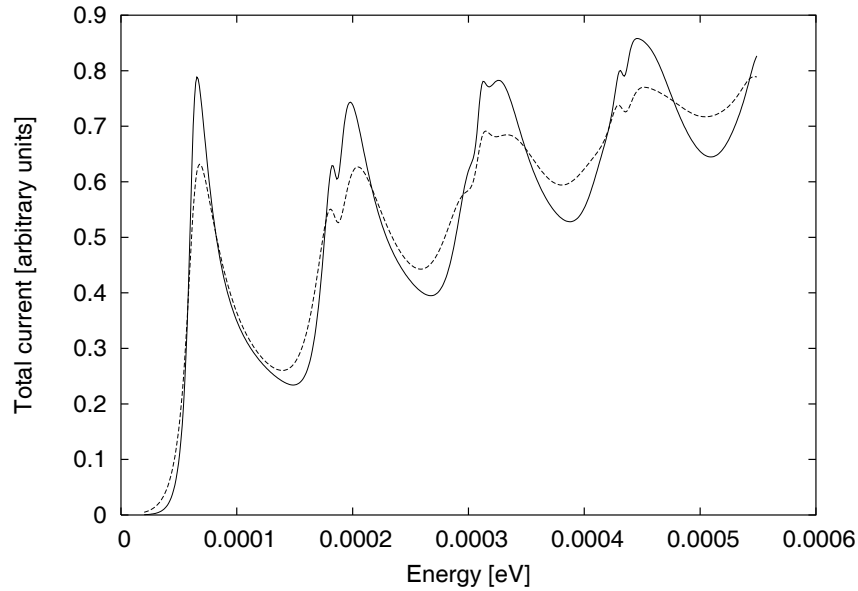


Figure 6.1: Thermal averaged curve for the total current as a function of energy. Magnetic field: $B = 1.07$ T, ion mass: $M = 32$ u. Solid line: $T = 400$ K, dashed line $T = 950$ K (see also [BIL79], Figure 2). The substructure and broadening of the Landau levels due to the perpendicular electric field is visible. However, the features are washed out (compared to Figure 4.7 on page 51) due to the averaging over a wide range of electric field values.

6.1.6 Zeeman level shifts

Unfortunately it is not possible to measure the (averaged) total current depicted in Figure 6.1 directly. The remaining major obstacle is the presence of a strong Zeeman splitting in the energy levels of the ion and atom. Let us examine a specific ionic system. Typical experiments [BJL78, BIL79, YKB03] are carried out with sulfur ions. An initial state of the ion commonly chosen in experiments is $|J, L, S\rangle = |3/2, 1, 1/2\rangle$. The final state (of the atom) is given by $|j, l, s\rangle = |2, 1, 1\rangle$ together with the detached electron in the state $|S = 1/2, m_s\rangle$. First we give the corresponding Lande factors for the electron, the ion, and the atom:

$$g_s = 2.002319\dots, \quad (6.14)$$

$$G = 1 + (g_s - 1)(J(J + 1) + S(S + 1) - L(L + 1))/(2J(J + 1)), \quad (6.15)$$

$$g = 1 + (g_s - 1)(j(j + 1) + s(s + 1) - l(l + 1))/(2j(j + 1)). \quad (6.16)$$

These Lande factors describe the Zeeman shift in the energy levels, which will influence the energy we have to plug in into the expression for the cross section ($M = -J \dots J$, $m_j = -j \dots j$, $m_s = \pm 1/2$)

$$E_{\text{zm}}(M, m, m_s) = (MG - mg - m_s g_s) \hbar \omega_L. \quad (6.17)$$

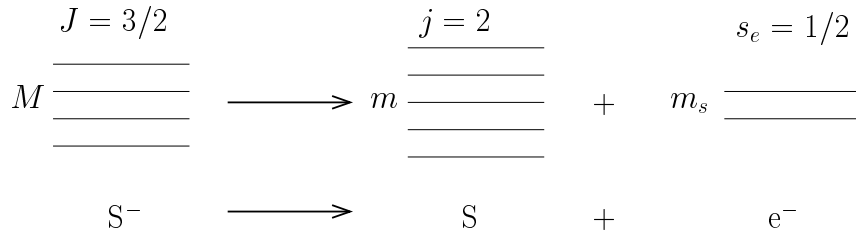


Figure 6.2: Energy levels for the ${}^2P_{3/2} \rightarrow {}^3P_2$ photodetachment transition in sulfur $S^- \rightarrow S + e^-$ in the presence of an magnetic field B . On the left hand side the ionic Zeeman levels are sketched. After the detachment, the neutral atom and the electron remain (right hand side).

In Figure 6.2 we show the level structure in the presence of a magnetic field. The allowed transitions are restricted by selection rules, that can be expressed in terms of Wigner $6j$ and Wigner $3j$ symbols. Following [BIL79], equation (35), we get the following expression for the angular momentum weighting factors

$$\begin{aligned}
\alpha(J, j, M, m, m_s) = & \sum_{J'=J-1}^{J+1} \sqrt{2(2j+1)(2J+1)} (-1)^{j+J-1/2} (2J'+1) \times \\
& \times \lambda(m+m_s-M) \langle f || P || i \rangle \begin{pmatrix} J' & 1 & J \\ -m-m_s & m+m_s-M & M \end{pmatrix} \times \\
& \times \begin{pmatrix} j & \frac{1}{2} & J' \\ m & m_s & -m-m_s \end{pmatrix} \begin{Bmatrix} 1 & 1 & 1 \\ J & \frac{1}{2} & J' \end{Bmatrix} \begin{Bmatrix} 1 & 1 & j \\ \frac{1}{2} & J' & \frac{1}{2} \end{Bmatrix}. \quad (6.18)
\end{aligned}$$

The polarization of the laser is characterized by $\lambda(m+m_s-M)$. I.e. $\lambda(0)$ is the component of the polarization vector parallel to the magnetic field, $\lambda(\pm 1)$ are the corresponding left and right circular polarized components. The total cross section now becomes

$$J_M(E) = \sum_{m=-j}^j \sum_{m_s=-1/2}^{1/2} |\alpha(J, j, M, m, m_s)|^2 J_{average}(E + E_{zm}(M, m, m_s)), \quad (6.19)$$

where J_M denotes the dependence of the total current on the magnetic quantum number M of the initial ionic state.

6.1.7 Rate calculation

In order to connect the total current or cross section to the number of ions $N(t_{\text{illu}})$ after a certain time of illumination t_{illu} , we have to sum over all initially populated states:

$$N(E, t_{\text{illu}}) = \sum_{M=-J}^J N_M \exp(-J_M(E)t_{\text{illu}}), \quad (6.20)$$

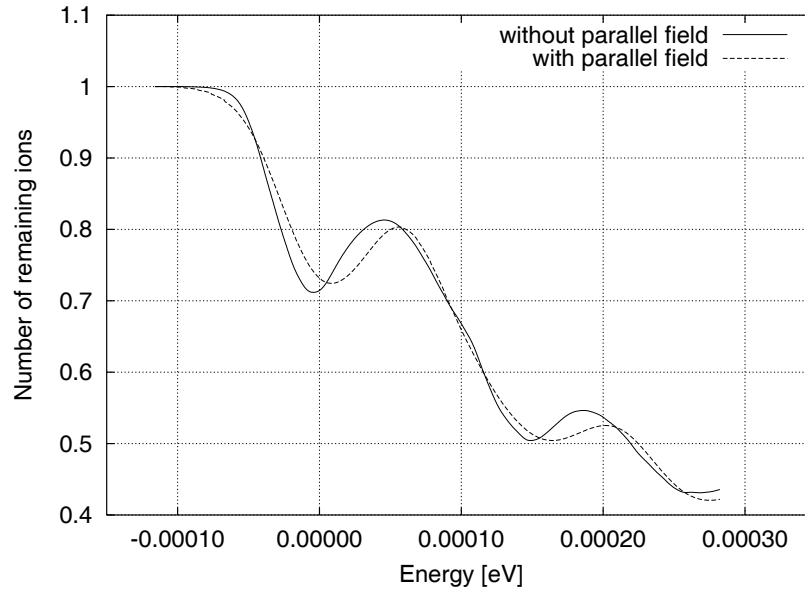


Figure 6.3: Rate with (dashed line) and without (solid line) applied external electric field parallel to the magnetic field. $B = 1$ T, ion mass $M = 32$ u, $T = 900$ K, $F_{\parallel, \text{peak}} = 1400$ eV/m.

where the temperature dependent weighting factor N_M is given by

$$N_M = \frac{e^{-MGk_B T}}{\sum_{M=-J}^J e^{-MGk_B T}}. \quad (6.21)$$

In the last line we assumed a Boltzmann distribution for the population of the initial occupied levels.

6.2 Predictions for the photodetachment rate

Figure 6.3 is a typical plot of the resulting current and rate. Depending on the presence of an additional electric field, the structure of the curves changes slightly. However, due to the large number of possible transitions the main features seen in Figure 6.1 are not easily recognized. In newer experiments [YKB03] an additional electric field is applied parallel to the magnetic field. In Figure 6.3 we show a comparison between the results with external and without external field. The electric field perpendicular to the motion of the ions and the external magnetic field is of course always present. Future experiments at lower temperatures and with a suitable laser polarization in order to minimize the number of allowed transitions should give a clearer picture of the underlying Green function.

Chapter 7

Spatially extended quantum sources

Extended sources arise in physical systems in a number of different situations. First of all, a point source can be viewed as the limit of a spatially extended source. Therefore, all results given for point sources should be obtained by a suitable limiting process from the results for extended sources. Considerably extended (up to some μm) quantum sources emerge in coherent atomic ensembles. Sometimes it is possible to characterize these ensembles by a macroscopic wave function. A prime example are condensates of dilute Bose gases, where a single quantum mechanical state is populated by a large number of atoms. Contrary to point-like sources, the scattering wave $\psi_{\text{sc}}(\mathbf{r})$ from an extended source $\sigma(\mathbf{r})$ is no longer just a multiple of the Green function but is obtained by an additional integration over coordinate space (see equation (2.33)):

$$\psi_{\text{sc}}(\mathbf{r}) = \int d\mathbf{r}' G(\mathbf{r}, \mathbf{r}'; E) \sigma(\mathbf{r}'). \quad (7.1)$$

We already noted that the energy-dependent Green function is known only for very few systems. Since the treatment of extended sources involves additional integrations, we will have to fall back to approximation schemes for the calculation of the scattering wave. However, at least one important reference case can be solved completely analytically. In molecular physics, considerable interest exists in radiation induced transitions between different electronic states. The initial state in these models is often described as a harmonic oscillator eigenstate. The formalism of quantum source theory can be used to calculate transition amplitudes and is closely related to the so-called Franck-Condon factor [Fra25, Con28]. The availability of new analytic reference-cases is important in order to establish criteria for the validity of numerical approximation schemes commonly employed in this field (see also [Ler90]). Specifically, the so-called reflection approximation plays a dominant role and we will derive and analyze this method within the energy-dependent Green function approach. The theory of the photodissociation of molecules like H_2^+ , D_2^+ , or even H_2O relies on the computation of the corresponding Franck-Condon factors [Her50, Dun68, Hel78, HE99].

7.1 Gaussian source distribution in a linear force field

We consider a source of isotropic Gaussian shape

$$\sigma(\mathbf{r}) = \gamma\psi_{\text{in}}(\mathbf{r}) = \gamma N_0 \exp(-r^2/(2a^2)). \quad (7.2)$$

The width of the source is specified by a and $N_0 = a^{-3/2}\pi^{-3/4}$ denotes the proper normalization from the condition

$$\int d^3\mathbf{r} |\psi_{\text{in}}(\mathbf{r})|^2 = 1. \quad (7.3)$$

The parameter γ takes care of the scattering potential W , which was introduced in equation (2.31). Here, we assume a constant potential γ . The three dimensional Green function for the linear force field is given in equation (4.21). The direct evaluation of equation (7.1) in position space is not easily achieved. Instead we use the integral representation of the energy-dependent Green function. For a more compact notation we introduce a set of scaled variables (the scaling parameter β was already defined in equation (4.23))

$$\begin{aligned} \xi &= \beta F x & \boldsymbol{\rho} &= \beta F \mathbf{r} \\ \nu &= \beta F y & \epsilon &= -2\beta E \\ \zeta &= \beta F z & \tau &= t/(2\hbar\beta), \end{aligned} \quad (7.4)$$

together with the scaled width $\alpha = \beta F a$. The Green function (see equation (2.16)) becomes

$$G_{\text{field}}(\boldsymbol{\rho}, \boldsymbol{\rho}'; \epsilon) = -2i\beta(\beta F)^3 \int_0^\infty \frac{d\tau}{(i\pi\tau)^{3/2}} e^{i(\boldsymbol{\rho}-\boldsymbol{\rho}')^2/\tau + i\tau(\zeta+\zeta'-\epsilon) - i\tau^3/12}, \quad (7.5)$$

and the scattered wave is given by equation (7.1):

$$\psi_{\text{sc}}(\boldsymbol{\rho}) = -2i\beta\gamma N_0 \int_0^\infty \frac{d\tau}{(i\pi\tau)^{3/2}} e^{i\tau(\zeta-\epsilon) - i\tau^3/12} \int d^3\boldsymbol{\rho}' e^{i(\boldsymbol{\rho}-\boldsymbol{\rho}')^2/\tau + i\tau\zeta'} e^{-\rho'^2/(2\alpha^2)}. \quad (7.6)$$

Now it is possible to carry out the Gaussian $\boldsymbol{\rho}$ integration. The remaining time integration has the form

$$\psi_{\text{sc}}(\mathbf{r}) = -2i\Lambda(\tilde{\epsilon})\beta(\beta F)^3 \int_{-2i\alpha^2}^\infty \frac{du}{(i\pi u)^{3/2}} \exp\left(\frac{i}{u}\tilde{\rho}^2 + iu(\tilde{\zeta} - \tilde{\epsilon}) - \frac{i u^3}{12}\right), \quad (7.7)$$

with the shifted parameters

$$\tilde{\zeta} = \zeta + 2\alpha^4 \quad \tilde{\epsilon} = \epsilon + 4\alpha^4, \quad \tilde{\rho}^2 = \xi^2 + \nu^2 + \tilde{\zeta}^2, \quad (7.8)$$

and an energy dependent factor $\Lambda(\tilde{\epsilon}) = \gamma(2\sqrt{\pi}a)^{3/2} e^{2\alpha^2(\tilde{\epsilon}-4\alpha^4/3)}$. We moved the temporal integration into the complex plane by substituting $u = \tau - 2i\alpha^2$. The representation chosen in equation (7.7) emphasizes the close relationship of $\psi_{\text{sc}}(\mathbf{r})$ to the Green function $G_{\text{field}}(\boldsymbol{\rho}, \mathbf{o}; \epsilon)$ given in equation (7.5). To evaluate the remaining integral analytically, we

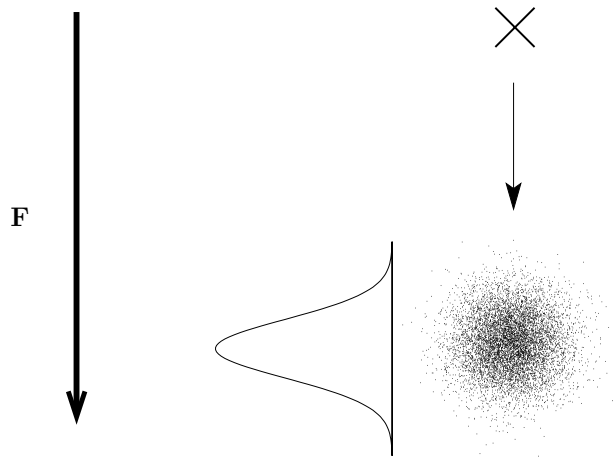


Figure 7.1: A Gaussian source distribution in a linear force field emits matter waves, that can be projected back to a virtual point-source which is vertically upwards shifted against the direction of the force \mathbf{F} .

split the path of integration into two sections, one along the real u -axis, the other one along the imaginary u -axis: $\psi_{\text{sc}}(\mathbf{r}) = \psi_{\text{near}}(\mathbf{r}) + \psi_{\text{far}}(\mathbf{r})$. The contribution due to

$$\begin{aligned} \psi_{\text{near}}(\mathbf{r}) &= -2i\Lambda(\tilde{\epsilon})\beta(\beta F)^3 \int_{-2i\alpha^2}^0 \frac{du}{(i\pi u)^{3/2}} e^{i\tilde{\rho}^2/u + iu(\tilde{\zeta} - \tilde{\epsilon}) - iu^3/12} \\ &\sim \Lambda(\tilde{\epsilon}) \frac{2\beta(\beta F)^3 \sqrt{2}\alpha}{\pi^{3/2} \tilde{\rho}^2} e^{-\tilde{\rho}^2/(2\alpha^2)} \end{aligned} \quad (7.9)$$

is a purely real term which drops off very quickly with increasing distance $\tilde{\rho}$ from the source region. The more interesting far-field contribution $\psi_{\text{far}}(\mathbf{r})$ can be exactly evaluated using the integral representation from equation (7.5):

$$\begin{aligned} \psi_{\text{far}}(\mathbf{r}) &= -2i\Lambda(\tilde{\epsilon})\beta(\beta F)^3 \int_0^\infty \frac{du}{(i\pi u)^{3/2}} e^{i\tilde{\rho}^2/u + iu(\tilde{\zeta} - \tilde{\epsilon}) - iu^3/12} \\ &= \Lambda(\tilde{\epsilon}) G_{\text{field}}(\tilde{\rho}, \mathbf{o}; \tilde{\epsilon}). \end{aligned} \quad (7.10)$$

With the help of equation (4.16) we can cast the last equation into the form

$$\psi_{\text{far}}(\mathbf{r}) = \gamma(2\sqrt{\pi}a)^{3/2} e^{-ma^2E/\hbar^2 + m^2F^2a^6/(3\hbar^4)} G_{\text{field}}(\mathbf{r}, -\frac{m\mathbf{F}}{2\hbar^2}a^4; E). \quad (7.11)$$

This expression displays a remarkable feature of the wave function $\psi_{\text{far}}(\mathbf{r})$ originating from a Gaussian source: The extended Gaussian source can be replaced by a virtual point source of the same energy at a location shifted by $m\mathbf{F}a^4/(2\hbar^2)$ from the center of the Gaussian distribution, carrying the energy dependent weight $\Lambda(\tilde{\epsilon})$. A sketch of this situation is shown in Figure 7.1. The virtual point source can be situated well outside the main Gaussian density distribution, since the shift increases very fast ($\propto a^4$) with the source width.

From equation (7.11), the expression for the currents due to the Gaussian distribution in equation (7.2) are conveniently found from the analogous expressions for a point source by just performing the indicated shifts. Neglecting $\psi_{\text{near}}(\mathbf{r})$, the far-field current density reads according to equation (4.24)

$$j_z(\boldsymbol{\rho}, \tilde{\epsilon}) = 16\sqrt{\pi}\gamma^2\beta^3 F^2/\hbar e^{4\alpha^2(\tilde{\epsilon}-4\alpha^4/3)} \times \\ \times \frac{\alpha^3}{\tilde{\rho}^3} \left\{ \tilde{\zeta}[\text{Ai}'(\tilde{\epsilon} - \tilde{\zeta} + \tilde{\rho})]^2 + \beta \left[\tilde{\zeta}(\tilde{\zeta} - \tilde{\epsilon}) + \tilde{\rho}^2 \right] [\text{Ai}(\tilde{\epsilon} - \tilde{\zeta} + \tilde{\rho})]^2 \right\}. \quad (7.12)$$

The same procedure yields the total current. However, since both $\psi_{\text{near}}(\mathbf{r})$ and $\sigma(\mathbf{r})$ are purely real and only the imaginary part of $\psi(\mathbf{r})$ is needed for the evaluation of the total current, the following expression obtained by shifting the energy in equation (4.25) is even an exact result:

$$J(\tilde{\epsilon}) = 64\pi^{3/2}\gamma^2\alpha^3\beta/\hbar e^{4\alpha^2(\tilde{\epsilon}-4\alpha^4/3)} \left\{ [\text{Ai}'(\tilde{\epsilon})]^2 - \tilde{\epsilon}[\text{Ai}(\tilde{\epsilon})]^2 \right\}. \quad (7.13)$$

We can check the result with the help of the sum rule given in equation (2.43). Indeed we obtain

$$\int_{-\infty}^{\infty} dE J(E) = \frac{2\pi}{\hbar} \gamma^2. \quad (7.14)$$

In Figure 7.2 we plot the resulting total current J as a function of energy E for different source widths a . From the validity of the sum rule we know that the area under all curves is equal. For small source sizes a plateau structure in the current is present and a asymmetric dependency on the energy is visible. The plateau structure is a typical feature of the electric field Green function where we linked the plateaus to two path interference phenomena in the corresponding current density distribution (see also Section 4.3).

7.1.1 Limit of large sources

In the limit of extended Gaussian sources, a simple approximation to this formula is available that leads to a geometrical interpretation. We start out with a time dependent integral formulation of the total current that follows from equations (2.38) and (2.6) after the spatial integrations are performed:

$$J(\tilde{\epsilon}) = 32\gamma^2\alpha^3\beta/\hbar e^{4\alpha^2(\tilde{\epsilon}-4\alpha^4/3)} \text{Im} \left\{ \int_0^{\infty} \frac{i du}{(iu)^{3/2}} e^{-iu\tilde{\epsilon}-iu^3/12} \right\}. \quad (7.15)$$

The integral is evaluated in saddle point approximation. Assuming $\alpha \gg \epsilon$ (note $\epsilon = \tilde{\epsilon} - 4\alpha^4$), we keep only the leading order terms of a Taylor expansion in the exponent and prefactor. The resulting current has Gaussian shape:

$$J_{\text{sp}}(\epsilon) = \frac{2\sqrt{\pi}\gamma^2\beta}{\alpha\hbar} e^{-\epsilon^2/(4\alpha^2)}. \quad (7.16)$$

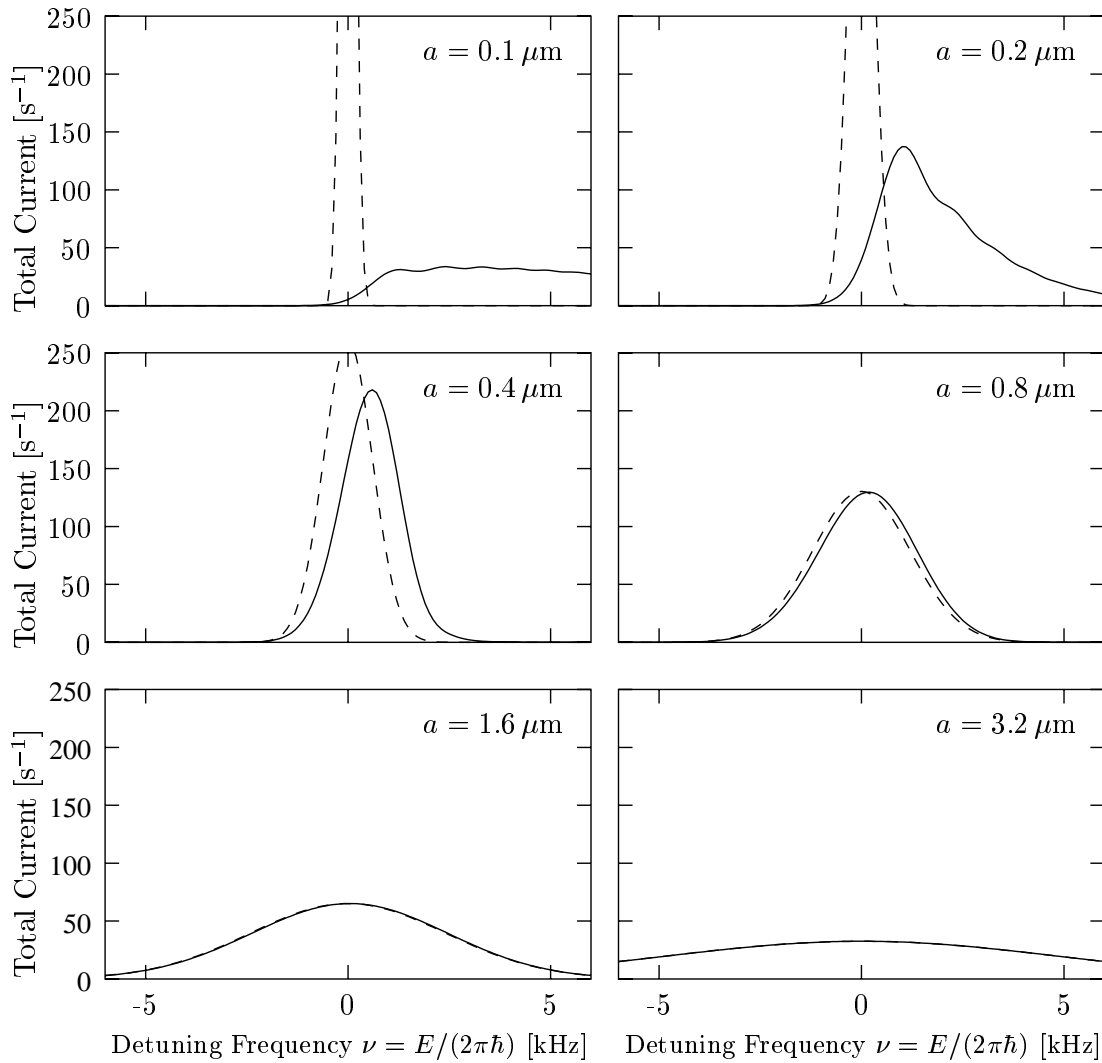


Figure 7.2: Transition from a point-like to an extended source in a linear potential. The source width is denoted by a . The solid line is the exact result from equation (7.13), whereas the dashed line shows the reflection approximation (equation (7.17)). For small source widths the reflection approximation fails to reproduce the quantum mechanical result. Parameter: $F = m_{\text{Rb}} g$, with $g = 9.81 \text{ m/s}^2$, and $m_{\text{Rb}} = 87 \text{ u}$.

This expression is equivalent to the implicit representation

$$J_{\text{sp}}(E) = \frac{2\pi}{\hbar} \int d^3\mathbf{r} |\sigma(\mathbf{r})|^2 \delta(E + Fz). \quad (7.17)$$

Evidently, the approximation (7.17) obeys the sum rule (2.43) for the total current $J(E)$. For extended sources, the energy dependence of $J_{\text{sp}}(E)$ reflects the source structure: By the resonance condition $E + Fz = 0$, the total current probes the density $|\psi_{\text{in}}(\mathbf{r})|^2$ on different slices across the source. In Figure 7.2 the dashed line denotes this slicing approximation. Since a similar approximation is sometimes employed in the theory of Franck-Condon factors, we will use the more common name *reflection approximation*. A necessary condition for applying this approximation is

$$E < \frac{mF^2a^4}{2\hbar^2}, \quad (7.18)$$

since then the virtual point source depicted in Figure 7.1 acquires a negative virtual energy. Only tunneling sources lack the interference fringes connected to classically allowed trajectories. In Chapter 8 we will further investigate this behavior and also discuss Gaussian sources with non-vanishing angular momentum.

7.2 Gaussian sources in parallel fields

Before we present a general derivation of the reflection approximation, we want to consider one additional example involving a Gaussian source. This time we analyze the Hamiltonian of a linear force field with an additional quadratic potential in the direction perpendicular to the linear field:

$$\mathbf{H}_{F\parallel B} = \frac{\mathbf{p}^2}{2m} + \frac{1}{2}m\omega_L^2(x^2 + y^2) - Fz. \quad (7.19)$$

Since all spatial coordinates are separable, we can construct the time evolution operator by multiplication of the one- and two-dimensional contributions (see Example 3 on page 19):

$$\begin{aligned} K_{F\parallel B}(x, y, z; 0|x', y', z'; t) &= e^{-3/4i\pi} \frac{m\omega_L}{2\pi\hbar \sin(\omega_L t)} \sqrt{\frac{m}{2\pi\hbar t}} \times \\ &\times \exp\left(\frac{im\omega}{2\hbar} \frac{(x^2 + x'^2 + y^2 + y'^2) \cos(\omega t) - 2(xx' + yy')}{\sin(\omega t)}\right) \times \\ &\times \exp\left(\frac{im}{2\hbar t}(z - z')^2 + \frac{iFt}{2\hbar}(z + z') - \frac{iF^2t^3}{24m\hbar}\right) \end{aligned} \quad (7.20)$$

Switching to more convenient units given by equation (7.8) and by

$$\tilde{\omega} = 2\hbar\beta\omega_L, \quad (7.21)$$

we obtain the total current from equation (2.38)

$$\begin{aligned}
J_{00}(E) = \frac{-4\beta}{\hbar\pi^3\alpha^3} \Im \left[\int d^3\boldsymbol{\rho} e^{-\rho^2/(2\alpha^2)} \int d^3\boldsymbol{\rho}' e^{-\rho'^2/(2\alpha^2)} \int_0^\infty d\tau \frac{\tilde{\omega}}{\sqrt{i\tau} \sin(\tilde{\omega}\tau)} \times \right. \\
\left. \times \exp\left(i\tilde{\omega}[(\xi - \xi')^2 + (\nu - \nu')^2] \cot(\tilde{\omega}\tau) + 2i\tilde{\omega}[\xi\nu' - \xi'\nu]\right) \times \right. \\
\left. \times \exp\left(+\frac{i}{\tau}(\zeta - \zeta')^2 + i\tau[\zeta + \zeta' - \epsilon] - \frac{i\tau^3}{12}\right) \right], \quad (7.22)
\end{aligned}$$

Since all coordinate space integrals are of Gaussian type, we can evaluate the integral and only the time-dependent integration remains

$$J_{00}(E) = \Im \left[\int_0^\infty d\tau \frac{32i\alpha^3\beta\tilde{\omega}e^{-i\tau\epsilon - \alpha^2\tau^2 - i\tau^3/12}}{\hbar\sqrt{i\tau} + 4\alpha^2(4\alpha^2\tilde{\omega} \cos(\tilde{\omega}\tau) + i(1 + 4\alpha^4\tilde{\omega}^2) \sin(\tilde{\omega}\tau))} \right]. \quad (7.23)$$

For the special case $a^2 = \hbar/(m\omega_L)$ (or $2\tilde{\omega} = 1/\alpha^2$ in scaled units) we get the simpler expression

$$\begin{aligned}
J_{00}(E) = e^{2-16\alpha^6/3+4\alpha^2\tilde{\epsilon}} \Im \left[\int_0^\infty du \frac{8i\alpha\beta e^{-iu(\tilde{\epsilon}+1/(2\alpha^2))-iu^3/12}}{\hbar\sqrt{iu}} \right] \\
= \frac{16\pi^{3/2}\alpha\beta}{\hbar} \exp\left(2 - \frac{16\alpha^6}{3} + 4\alpha^2\tilde{\epsilon}\right) \left(\text{Ai} \left[\tilde{\epsilon} + \frac{1}{2\alpha^2} \right] \right)^2. \quad (7.24)
\end{aligned}$$

Here, we used the shifted quantities from equation (7.8) and introduced $u = \tau - 4i\alpha^2$. The last equation contains essentially the one-dimensional propagator of the linear force field, which is available analytically. This simplification is to be expected since a source of the form

$$\sigma(\mathbf{r}) = \left(\frac{m\omega_L}{\pi\hbar} \right)^{1/2} \exp\left(-\frac{m\omega_L(x^2 + y^2)}{2\hbar} \right) \quad (7.25)$$

is an eigenstate of the Hamiltonian under consideration. In Figure 7.3 we plot the total current as a function of the energy for different widths a of the source. For larger sources the energy-dependence of the total current shows a strong asymmetry, whereas for smaller source sizes an oscillatory structure emerges. Also the Landau-level structure becomes visible in the first two panels at energies $2\hbar\omega_L \approx 8$. The corresponding point-source current is depicted in Figure 4.1 on page 41. In Section 7.3.1 we will derive the reflection approximation for the same problem and compare it with the exact results.

7.3 General source distribution

In the previous sections we considered the specific case of a Gaussian source function. However, the reflection approximation is not limited to Gaussian distributions and we will now derive a justification for the approximation involving a general source term. In the

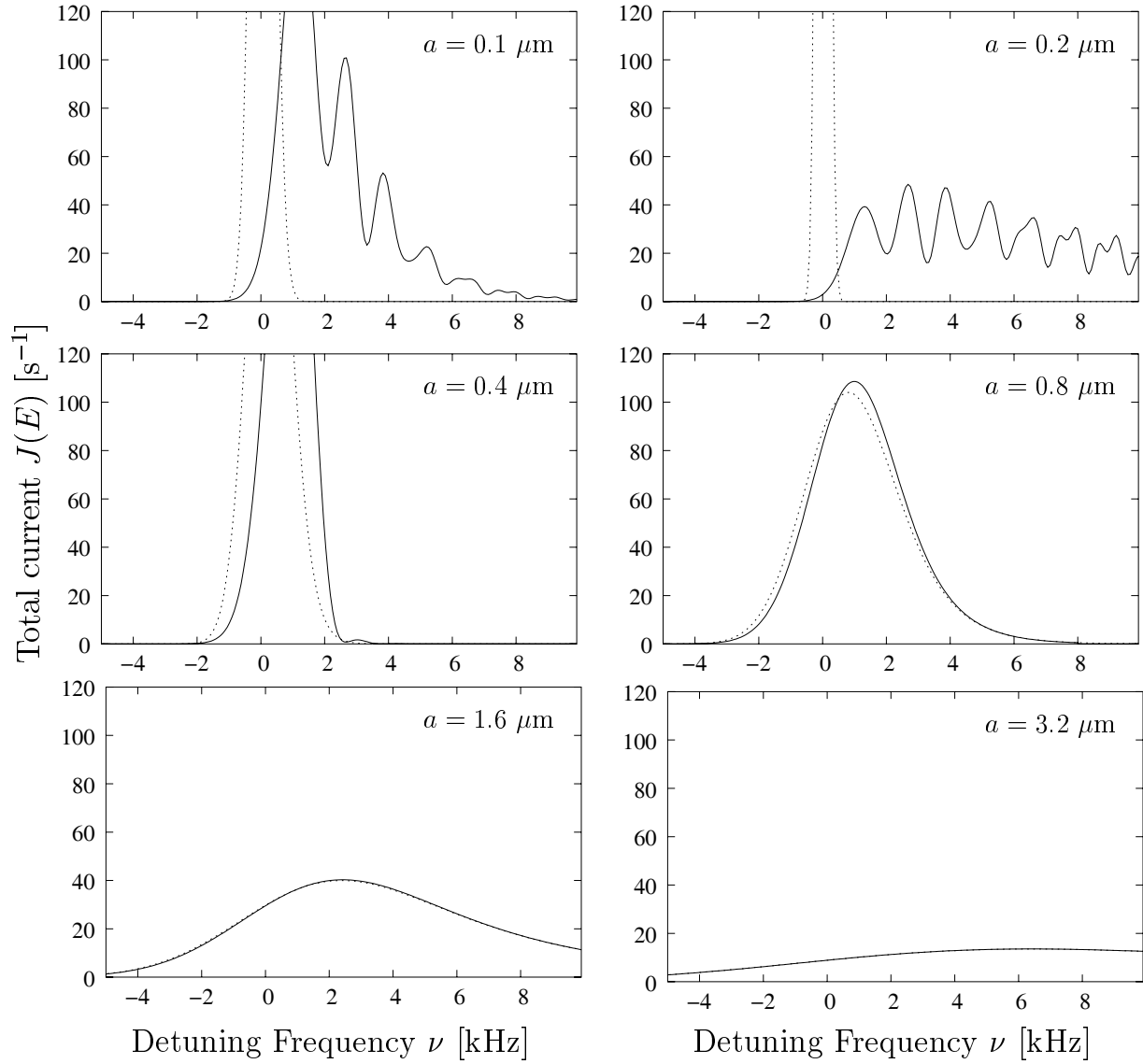


Figure 7.3: Transition from a point-like to an extended source in a quadratic potential. The source width is denoted by a . The solid line is the exact result from equation (7.23), whereas the dashed line shows the reflection approximation (equation (7.40)). For small source widths the reflection approximation fails to reproduce the quantum mechanical result. Parameter: $\tilde{\omega} = 1$, $F = m_{\text{Rb}} g$, with $g = 9.81 \text{ m/s}^2$, and $m_{\text{Rb}} = 87 \text{ u}$.

linear force field the total current due to a source $\sigma(\mathbf{r})$ is determined by inserting the field Green function in equation (2.42):

$$J(E) = \frac{1}{\hbar^2} \int_{R^7} d^3\mathbf{r} d^3\mathbf{r}' dt \left(\frac{m}{2\pi i \hbar t} \right)^{3/2} e^{iEt/\hbar} e^{\frac{i}{\hbar} [\frac{m}{2t} |\mathbf{r}-\mathbf{r}'|^2 + \frac{Ft}{2}(z+z') - \frac{F^2 t^3}{24m}]} \sigma(\mathbf{r})^* \sigma(\mathbf{r}'). \quad (7.26)$$

After introducing relative coordinates by the coordinate transformation

$$(x, y, z) = (u + u', v + v', w + w') \quad (u, v, w) = \mathbf{s} \quad (7.27)$$

$$(x', y', z') = (u - u', v - v', w - w') \quad (u', v', w') = \mathbf{s}', \quad (7.28)$$

this becomes

$$J(E) = \frac{8}{\hbar^2} \int_{R^7} d\mathbf{s} d\mathbf{s}' dt \left(\frac{m}{2\pi i \hbar t} \right)^{3/2} e^{i(E+i\eta+Fw)t/\hbar + i\frac{2m}{\hbar t} |\mathbf{s}'|^2 - \frac{i}{24m\hbar} F^2 t^3} \sigma(\mathbf{s} + \mathbf{s}')^* \sigma(\mathbf{s} - \mathbf{s}'). \quad (7.29)$$

Up to now this is an exact result. Now we will make the first approximation. We use a Taylor expansion for the product of the shifted source terms $\sigma(\mathbf{s} + \mathbf{s}')^* \sigma(\mathbf{s} - \mathbf{s}')$ and consider here only the first order term. Integrating over \mathbf{s}' yields

$$\int d^3\mathbf{s}' \exp(-\gamma s'^2) f(s + s') f^*(s - s') \approx |f(s)|^2 \int d^3\mathbf{s}' \exp(-\gamma s'^2) = |f(s)|^2 \pi^{3/2} \gamma^{-3/2}, \quad (7.30)$$

where $\gamma = -2im/(\hbar t)$. We discuss higher order terms in Appendix D, but may already comment that this so-called peak approximation only works for extended sources, where the overlap between $\sigma(\mathbf{s} + \mathbf{s}')^*$ and $\sigma(\mathbf{s} - \mathbf{s}')$ is significant in a large region determined by the imaginary part of t . With these drastic omissions we get a considerably simplified equation for the total current

$$J(E) = \frac{1}{\hbar^2} \int_{R^4} d\mathbf{s} dt e^{i(E+Fw)t/\hbar} e^{-\frac{i}{24m\hbar} F^2 t^3} |\sigma(\mathbf{s})|^2. \quad (7.31)$$

Next we introduce the scaled variable $\tau = t/(2\hbar\beta)$, carry out the integration over τ using equation (B.11)

$$J(E) = \frac{2\beta}{\hbar} \int_{R^4} d\mathbf{s} d\tau e^{2i\tau\beta(E+Fw) - i\tau^3/12} |\sigma(\mathbf{s})|^2 \quad (7.32)$$

$$= -\frac{4\beta\pi}{\hbar} \int_{R^3} d\mathbf{s} \text{Ai}[-2\beta(E + Fw)] |\sigma(\mathbf{s})|^2, \quad (7.33)$$

and consider the semiclassical limit $\hbar \rightarrow 0$ (or $\beta \rightarrow \infty$):

$$J(E) = \frac{2\pi}{\hbar} \int_{R^3} d\mathbf{s} |\sigma(\mathbf{s})|^2 \lim_{\beta \rightarrow \infty} \{-2\beta \text{Ai}[-2\beta(E + Fw)]\} = \frac{2\pi}{\hbar} \int_{R^3} d\mathbf{s} |\sigma(\mathbf{s})|^2 \delta(E + Fw). \quad (7.34)$$

In the last line we use a known representation of the δ -function in terms of the Airy function:

$$\delta(x) = \lim_{\epsilon \rightarrow 0} \frac{1}{\epsilon} \text{Ai}\left(\frac{x}{\epsilon}\right). \quad (7.35)$$

Equation (7.34) is exactly the desired reflection approximation. The limited validity of the expression is obvious, since the derivation required two significant simplifications. The replacement of the Airy function by a δ function is also dubbed δ -function approximation (see references in [Her50, Dun68]). Although higher order terms from the Taylor expansion of the source terms are in principle available, the convergence of the expansion can not be taken for granted. So-called quantum corrections to the (not even) semiclassical reflection approximation are also considered by Gislason [Gis73], and by Heller in a Wigner phase-space approach to the problem [Hel78].

7.3.1 Reflection approximation in parallel fields

We already used the reflection approximation for the case of a Gaussian source in a linear force field. As a second example consider the additional quadratic potential given in equation (7.19). The three-dimensional Gaussian source is, of course, just the product of three one-dimensional Gaussian distributions

$$\sigma_{3D}(\mathbf{r}) = \prod_{i=1}^3 \sigma_{1D}(x_i), \quad (7.36)$$

where

$$|\sigma_{1D}(x_i)|^2 = a^{-1} \pi^{-1/2} e^{-x_i^2/a^2}. \quad (7.37)$$

Applying the reflection approximation we obtain

$$J(E) = \frac{2\pi}{\hbar} \iint dx dy |\sigma_{1D}(x)|^2 |\sigma_{1D}(y)|^2 \int dz |\sigma_{1D}(z)|^2 \delta \left(\frac{1}{2} m \omega_L^2 (x^2 + y^2) - Fz - E \right). \quad (7.38)$$

Introducing cylindrical coordinates with $x = \tilde{\omega}^2(\xi^2 + \nu^2)$ yields

$$J(\epsilon) = \frac{2\sqrt{\pi}\beta}{\hbar\alpha^3\tilde{\omega}^2} \exp(-\epsilon^2/(4\alpha^2)) \int_0^\infty dx \exp \left(-\frac{x^2}{4\alpha^2} - x \frac{2\epsilon - 4/\tilde{\omega}^2}{4\alpha^2} \right). \quad (7.39)$$

Therefore, the total current becomes

$$J(\epsilon) = \frac{2\pi\beta}{\hbar\alpha^2\tilde{\omega}^2} \exp \left(\frac{1 + \epsilon\tilde{\omega}^2}{\alpha^2\tilde{\omega}^4} \right) \operatorname{erfc} \left(\frac{2 + \epsilon\tilde{\omega}^2}{2\alpha\tilde{\omega}^2} \right). \quad (7.40)$$

In Figure 7.3 we compare this result with the exact solution given in equation (7.24). Again, the source width is the important parameter that determines the applicability of the reflection approximation. Interference phenomena that lead to the pronounced oscillation in the current for small sources are absent in the simple reflection approximation.

7.4 The Franck-Condon principle

The total scattering current from an extended source is closely connected to the *Franck-Condon* principle. Franck was considering transitions between different molecular states.

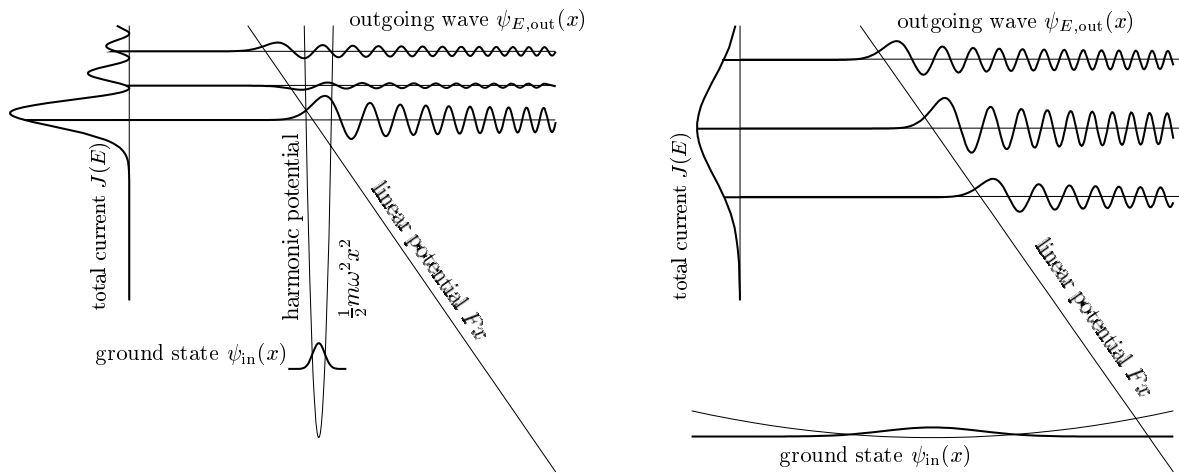


Figure 7.4: One-dimensional model for the evaluation of the Franck-Condon factor. Left panel: The strong harmonic potential sustains a narrow ground state wave-function that probes the outgoing wave function. The total current shows strong oscillations. Right panel: For a large source the oscillating structure of the outgoing wave is washed out. The total current reflects the source-structure and attains a Gaussian shape. In both cases the total current is obtained from equation (7.49).

To calculate the total cross section of absorption processes in molecular transitions Franck postulated the following empirical rule [Fra25]: The electron jump in a molecule takes place so rapidly in comparison to the vibrational motion that immediately afterwards the nuclei still have very nearly the same relative positions and velocities as before the jump. We will use the following wave-mechanical formulation of the Franck-Condon principle, due to Condon [Con28]: The total absorption cross section is proportional to the square of the matrix element of the interaction $W(\mathbf{r})$ between the initial state and the final state [Her50]:

$$\sigma_{\text{tot}}(E) \propto |\langle \psi_{\text{fi}}(E) | W | \psi_{\text{in}} \rangle|^2. \quad (7.41)$$

In the quantum source approach equation (3.25) gives the following symbolic form of the total current

$$J(E) = \frac{2\pi}{\hbar} \sum_{\text{fi}} \delta(E - E_{\text{fi}}) |\langle \psi_{\text{fi}}(E) | W | \psi_{\text{in}} \rangle|^2, \quad (7.42)$$

which is also considered by Heller [Hel78].

7.4.1 Application to continuum transitions

The Franck-Condon formula (7.41) involves the overlap integral between initial and final states. In the Green function approach we avoid the explicit calculation of the final state wave function, since all information about this state is already encoded in the Green function. To see how both methods are connected, we consider the example of a transition

from a bound state in a harmonic potential to a continuum state in a linear force field. The Hamiltonian of the initial state is given by the harmonic oscillator potential

$$H_{\text{in}} = \frac{p^2}{2m} + \frac{1}{2}m\omega^2 x^2. \quad (7.43)$$

Thus, the ground state wave function

$$\psi_{\text{in}} = \left(\frac{m\omega}{\pi\hbar}\right)^{1/4} \exp(-x^2/(2a^2)) \quad (7.44)$$

is a Gaussian distribution with half width

$$a = \sqrt{\frac{\hbar}{m\omega}}. \quad (7.45)$$

In the lower part of Figure 7.4 we plot the ground state wave function and the quadratic potential. For the final state we use the Hamiltonian

$$H_{\text{fi}} = \frac{p^2}{2m} - Fx + E_{\text{offset}}. \quad (7.46)$$

The upper part of Figure 7.4 shows the potential and the imaginary part of the continuum wave function given by

$$\begin{aligned} \psi_{\text{out}}(x) &= \int dx' G_{\text{field}}(x, x'; E) \sigma(x') \\ &= 2i\sqrt{2\hbar\pi}^{-1/4} \sqrt{F\alpha\beta^3} e^{-8\alpha^6/3+2\alpha^2\tilde{\epsilon}} \int_0^\infty du \frac{1}{\sqrt{i u}} e^{iu(\tilde{\zeta}-\tilde{\epsilon})+i\tilde{\zeta}^2/u-iu^3/12} \\ &= 4\sqrt{2\hbar\pi}^{5/4} \sqrt{F\alpha\beta^3} e^{-8\alpha^6/3+2\alpha^2\tilde{\epsilon}} Q_0(\tilde{\zeta}, \tilde{\zeta}, \tilde{\epsilon}), \end{aligned} \quad (7.47)$$

where Q_0 is stated in equation (B.1)

$$Q_0(\rho, \zeta, \epsilon) = \text{Ai}(\epsilon - \zeta + \rho) \text{Ci}(\epsilon - \zeta - \rho), \quad (7.48)$$

and the scaled parameters are defined in equation (7.8). According to equation (3.23) the total current is the imaginary part of the overlap integral between ψ_{in} and ψ_{out} :

$$\sigma_{\text{tot}}(E) \propto J(E) = -\frac{2}{\hbar} \Im [\langle \psi_{\text{in}} | \psi_{\text{out}} \rangle] \quad (7.49)$$

In Figure 7.4 the cross section is plotted in the upper left corner of each panel. We depict the situation for two different harmonic oscillator frequencies. For a weak harmonic potential (corresponding to a small frequency ω), the Gaussian source wave function ψ_{in} becomes broad and the overlap integral is largely determined by the overlap of the first oscillation period of the continuum wave function with the Gaussian ground-state. This interpretation is consistent with the reflection approximation:

$$J(E) = -\frac{2}{\hbar} \int dx \delta(E + Fx) |\psi_{\text{in}}(x)|^2. \quad (7.50)$$

However, for a stronger oscillator potential (corresponding to a higher frequency w) the situation changes completely. Now, the more peaked Gaussian ground state probes the continuum wave function at different energies. Therefore, we get an oscillatory structure with zeroes for some energies.

In [HE98], Section III.A, the authors discuss this example in terms of the Franck-Condon theory (equation (7.41)). One main difference is that the Franck-Condon expression involves the absolute value squared of the overlap between the initial wave function ψ_{in} and the final state wave function ψ_{fi} . It is important to recall that the final wave function is not identical to the scattering wave function ψ_{out} . However, both methods yield identical results for the total cross section, as shown in Section 3.2. One major draw-back of the final state formalism is that the current density (related to the scattering wave function) is not available.

The evaluation of overlap integrals is a non-trivial task, since it involves in general more than one integration (depending on the number of dimensions involved). In the time-dependent propagator picture the crucial “spatial” integrations can sometimes be performed analytically, thus only one integration (the Laplace transform over t to get the energy-dependent result) remains. Lermé [Ler90] lists some analytic expressions for Franck-Condon factors of bound-continuum transitions in one and two-dimensional systems. These factors are obtained from overlap integrals and are compared to numerical calculations and approximation schemes.

Chapter 8

Matter waves in the gravitational field: The “atom laser”

The last chapter is concerned with the emission of matter waves from an extended coherent atom source. A Bose-Einstein condensate (BEC) is a possible realization of this type of quantum source. The controlled and coherent release of atoms from such a condensate is called atom-laser. We will set up and discuss a completely analytical model for the description of the efficiency of such an atom laser and also for the density distribution in the resulting atom beam. Especially for strongly confined Bose-Einstein condensates (realized in so-called microtraps) the appearance of strong interference phenomena in the atomic beam is predicted. In the second part of this chapter we consider rotating quantum sources. A BEC under rotation develops an interesting phase and density structure due to the formation of quantized flux vortices. In the quantum-source approach these vortices are modeled as a superposition of multipole sources carrying high angular momenta. The combination of spatially extended sources with multipole sources leads to interesting effects upon the beam profile of the atom laser. One major advantage of the quantum source theory is the complete inclusion of the gravitational field. Previous theories of the atom laser either neglect gravity completely [BJT99, BS00] or use one-dimensional models that are not easily extended to three dimensions [SS99, SS00]. A first numerical calculation of the output rate of an atom laser in three dimension including gravity is given in [GBA01].

8.1 Bose-Einstein condensation

For a review on the physics and the historical development of Bose-Einstein condensation in dilute gases we refer the reader to the available literature [DGPS99, PS02]. Here, we are mainly interested in the form of the ground state of the BEC, since this determines the analytic model for the source wave function $\sigma(\mathbf{r})$. To be more specific, let us consider a trapped gas of cold Rubidium atoms. With coils around the cloud of atoms a magnetic field is generated that couples to the hyperfine levels of the nuclear spin of the Rubidium atoms. By using a suitable configuration of coils a local potential minimum is produced at

some point inside the trap. Around this local minimum, we can expand the potential due to the magnetic and gravitational forces quadratically. Since the cooled atoms are bosons (the sum of the nuclear spin and the orbital spin is an integer), the thermodynamical occupation number of the ground state of the trapping potential becomes very large for small temperatures, as already predicted (without using quantum mechanics) by Bose and Einstein. In the case of non-interacting particles, we can rewrite the many-particle ground state as a product wave function of single-particle states. The single-particle ground states in a harmonic trapping potential are Gaussian wave functions with a width determined solely by the strength of the trapping potential. The observed widths of condensates are considerably larger than the width expected for a non-interacting gas. Due to van der Waals forces, an effective repulsive interaction enlarges the condensate. One way to treat these interactions analytically is the so-called Gross-Pitaevskii equation (see [FW71, DGPS99] for a derivation and discussion)

$$\left[-\frac{\hbar^2 \nabla^2}{2m} + V_{\text{trap}}(\mathbf{r}) + g_{\text{sc}} |\psi(\mathbf{r})|^2 \right] \psi(\mathbf{r}) = \mu \psi(\mathbf{r}), \quad (8.1)$$

where g_{sc} comes from a simple ansatz for the two-body potential

$$V_{\text{interaction}}(\mathbf{r} - \mathbf{r}') = g_{\text{sc}} \delta(\mathbf{r} - \mathbf{r}'). \quad (8.2)$$

The scattering length a_{sc} provides another way to express the coupling strength $g_{\text{sc}} = 4\pi\hbar^2 a_{\text{sc}}/m$. For large condensates, a further simplification of the Gross-Pitaevskii equation is frequently used, the so-called Thomas-Fermi approximation:

$$|\psi(\mathbf{r})|^2 = g_{\text{sc}}^{-1} (\mu - V_{\text{trap}}(\mathbf{r})) \Theta(\mu - V_{\text{trap}}(\mathbf{r})). \quad (8.3)$$

This rather drastic simplification is obtained by neglecting the kinetic energy term in the Gross-Pitaevskii equation. The numerical solution of the Gross-Pitaevskii equation is in principle possible, but requires some computational effort. A feasible alternative is the use of variational methods to get approximate values for the ground-state energy and density distribution [EB95, EDC⁺96, PGMC⁺97]. The simplest choice of a trial wave function is again a Gaussian function, however this time we consider the width to be a variational parameter. By minimizing the energy functional of the Gross-Pitaevskii equation, we obtain the best approximation to the real ground state in terms of a single Gaussian wave function. In Figure 8.1 we compare three different approaches to obtain the ground state of a harmonically trapped BEC. Note, that we choose a strongly confined BEC with trapping frequency $\omega = 2\pi 3000/\sqrt{2}$ Hz and $N = 100$ atoms. Contrary to the Thomas-Fermi limit, a Gaussian profile is a good approximation to the numerical solution of the Gross-Pitaevskii equation. Therefore, we will use Gaussian wave functions for the description of strongly confined BECs. For larger condensates the Thomas-Fermi wave function may be a more appropriate choice.

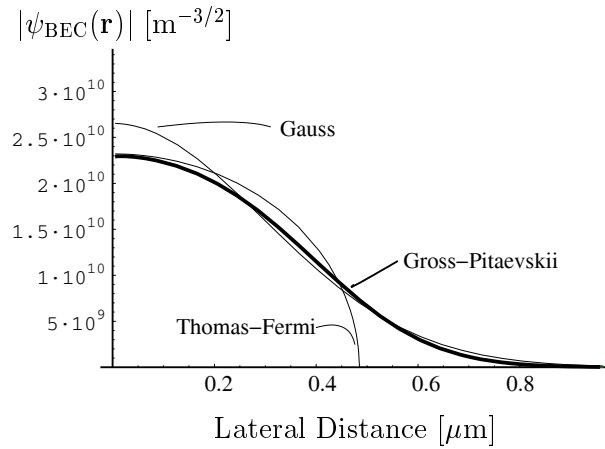


Figure 8.1: Plot of the ^{87}Rb BEC ground state with $N = 100$ atoms in a strong trapping potential ($\omega_x = \omega_y = \omega_z = 2\pi \frac{3000}{\sqrt{2}}$ Hz). The numerical solution of the Gross-Pitaevskii equation is compared with the Thomas-Fermi approximation and the variational ground state using a Gaussian trial function. The Gaussian wave function provides a good approximation of the Gross-Pitaevskii solution.

8.2 Radio output coupling from a BEC

After the discussion of the trapping potential and the ground state of a BEC, we consider the controlled release of atoms from the trap. Many experiments with BECs study the condensate by simply switching off the trapping potential. The BEC drops down and expands due to the inter-atomic repulsion and the dispersion of the wave-packet. This expansion (typical by a factor of forty) makes the initial rather small ($\approx 10 \mu\text{m}$) condensates easier visible and allows to detect the presence of the condensed state due to the different expansion rate compared to that of a thermal cloud. Of course, the condensate is lost afterwards and a new one has to be created. On the long run a more stable condensate (for example by refilling the BEC) is desirable to study effects on longer time scales. One way to monitor the BEC without switching off the trap is the use of a very weak perturbation in order to coherently out-couple a small fraction of condensate atoms. A first pulsed atom laser (driven by a rather strong perturbation using a magnetic field amplitude of about 0.5 Gauss) was realized in the group of Ketterle [MAK⁺97]. Shortly afterwards the quasi-continuous release of atoms was achieved by using a much weaker perturbation (about 1 mGauss magnetic field amplitude) [BHE99]. In both setups an oscillating magnetic field is applied to the magnetically trapped atoms. This field induces Rabi-type oscillations between the different magnetic hyperfine levels of the trapped atoms (i.e. $m = +1, 0, -1$). Clearly, a state with a magnetic quantum number of $m = 0$ is not trapped any more and can therefore leave the trap region. This non-trapped state enters the gravitational field of the earth which determines the evolution of the out-coupled atom wave function. The out-coupled atoms still form a coherent ensemble of atoms.

8.3 Transition from a BEC state to the gravitational field

We use a simple two state model to study the properties of the released atoms. One state is a bound state of the Hamiltonian \mathbf{H}_{trap} , the second state is a scattering state of the Hamiltonian \mathbf{H}_{cont} containing an external potential. Both states have an energy difference of $\Delta E = E_{\text{cont}} - E_{\text{trap}}$ and are weakly coupled by a homogeneous but oscillating interaction potential of strength $\hbar\Omega$:

$$(\mathbf{i}\hbar\partial_t - \mathbf{H}_{\text{cont}})\psi_{\text{cont}}(\mathbf{r}, t) = \hbar\Omega e^{-i\Delta Et/\hbar}\psi_{\text{trap}}(\mathbf{r}, t), \quad (8.4)$$

$$(\mathbf{i}\hbar\partial_t - \mathbf{H}_{\text{trap}})\psi_{\text{trap}}(\mathbf{r}, t) = \hbar\Omega e^{+i\Delta Et/\hbar}\psi_{\text{cont}}(\mathbf{r}, t). \quad (8.5)$$

We split off the time dependence of the states

$$\psi_{\text{cont}}(\mathbf{r}, t) = e^{-iE_{\text{cont}}t/\hbar}\psi_{\text{cont}}(\mathbf{r}), \quad (8.6)$$

$$\psi_{\text{trap}}(\mathbf{r}, t) = e^{-iE_{\text{trap}}t/\hbar}\psi_{\text{trap}}(\mathbf{r}), \quad (8.7)$$

to obtain the stationary equations

$$(E_{\text{cont}} - \mathbf{H}_{\text{cont}})\psi_{\text{cont}}(\mathbf{r}) = \hbar\Omega\psi_{\text{trap}}(\mathbf{r}), \quad (8.8)$$

$$(E_{\text{trap}} - \mathbf{H}_{\text{trap}})\psi_{\text{trap}}(\mathbf{r}) = \hbar\Omega\psi_{\text{cont}}(\mathbf{r}). \quad (8.9)$$

Upon introducing the energy-dependent Green function $G_{\text{cont}}(\mathbf{r}, \mathbf{r}'; E)$ for \mathbf{H}_{cont}

$$(E - \mathbf{H}_{\text{cont}})G_{\text{cont}}(\mathbf{r}, \mathbf{r}'; E) = \delta(\mathbf{r} - \mathbf{r}'), \quad (8.10)$$

the formal solution of equation (8.8) is given by

$$\psi_{\text{cont}}(\mathbf{r}) = \hbar\Omega \int d^3\mathbf{r}' G_{\text{cont}}(\mathbf{r}, \mathbf{r}'; E_{\text{cont}}) \psi_{\text{trap}}(\mathbf{r}'). \quad (8.11)$$

A similar equation holds for $\psi_{\text{trap}}(\mathbf{r})$. However, if we assume only a weak interaction in the sense that $\psi_{\text{trap}}(\mathbf{r})$ is not changed appreciably by the interaction, we may as a first approximation replace $\psi_{\text{trap}}(\mathbf{r})$ in equation (8.11) by the bound eigenstate $\psi_0(\mathbf{r})$ of \mathbf{H}_{trap} , which is defined by

$$(E_0 - \mathbf{H}_{\text{trap}})\psi_0(\mathbf{r}) = 0. \quad (8.12)$$

In this way we have decoupled both equations and we obtain a new Schrödinger equation with an inhomogeneous source term $\sigma(\mathbf{r}) = \hbar\Omega\psi_0(\mathbf{r})$

$$(E_{\text{cont}} - \mathbf{H}_{\text{cont}})\psi_{\text{cont}}(\mathbf{r}) = \sigma(\mathbf{r}). \quad (8.13)$$

The state $\psi_0(\mathbf{r})$ is the BEC ground-state wave function, that is described above. Employing a Gaussian wave function in the following form

$$\sigma(\mathbf{r}) = \sqrt{N} \hbar\Omega a^{-3/2} \pi^{-3/4} \exp(-r^2/(2a^2)), \quad (8.14)$$

enables us to use the analytic results for the Green function of the linear force field with an extended source from Chapter 7. Here, $\hbar\Omega$ denotes the strength of the interaction potential and N the number of condensate atoms.

8.4 Energy range for the operation of an atom laser

First, we investigate the total current generated by the out-coupling process. From equation (7.13) we expect a strong energy dependence of the current. The energy parameter is given by the difference of the applied radio frequency $h\nu$ and the condensate energy E_0 :

$$E = h\nu - E_0 \equiv h\Delta\nu \quad (8.15)$$

If $E < mF^2a^4/(2\hbar^2)$ holds, the reflection approximation may be used to further simplify the calculations. Experimental data concerning the number of remaining condensate atoms $N(T)$ after $T = 20$ ms of atom laser operation is available [GBA01]. Obviously, this number is related to the current via

$$N(T) = N(0) \exp[-J(E)T], \quad (8.16)$$

where $N(0)$ denotes the initial number of atoms in the BEC and $J(E)$ the total current. Besides the gravitational force, the relevant parameters entering the theoretical prediction for $J(E)$ in equation (7.13) are the coupling strength $\hbar\Omega$ and the Gaussian width a of the condensate. In Figure 8.2, the calculated number of remaining atoms is compared to the experimental measurement by Bloch et al. reported in [GBA01]. The coupling frequency Ω used for the calculation is fixed by the sum rule (2.43) applied to the experimental data, and the effective width $a = 2.8 \mu\text{m}$ (that is actually largely governed by atomic repulsion in the BEC) is obtained from a fit. Contrary to the case of photodetachment, the current characteristics faithfully reproduces the Gaussian shape of the source, as stated by the reflection approximation obtained by slicing the condensate at height $z = E/F$ (7.17). However, according to the exact expression for $J(E)$ in equation (7.13), source theory predicts a dramatic change in behavior of the total current for smaller condensate sizes as illustrated before in Figure 7.2 on page 81. The corresponding beam profiles are shown in Figure 8.3. We chose as initial energy $E = h\Delta\nu$ with $\Delta\nu = 2.5$ kHz. The distance from the source is varied from $z_{\min} = 0.2$ mm to $z_{\max} = 1.2$ mm. In the figure, a distinct ring pattern in the current density prevails for $a \leq 0.4 \mu\text{m}$. The number of fringes diminishes with increasing source width, until for $a \geq 0.8 \mu\text{m}$ the current profile attains an increasingly narrow Gaussian shape. To interpret this behavior, we first note that for an extended source region, the simple concept of two interfering paths originating from a single point in space is not readily applicable. Recalling the particular property of a Gaussian source to act as a virtual point source shifted in space (7.11), we may recover the concept of interfering paths. However, the effective initial kinetic energy decreases with growing source size (7.8) and becomes negative for $E < mF^2a^4/(2\hbar^2)$, leading to a “virtual” tunneling source that emits a beam of Gaussian profile.

The required condensate width is in principle obtainable with present-day microtraps [OFS⁺01, RHH99]. However the operation of these traps remains challenging. Future experiments in next generation microtraps should be able to collect data in the interesting regime that is governed by quantum interferences. One possible application of an atom laser is the formation of a tailored beam wave function by using a superposition of different

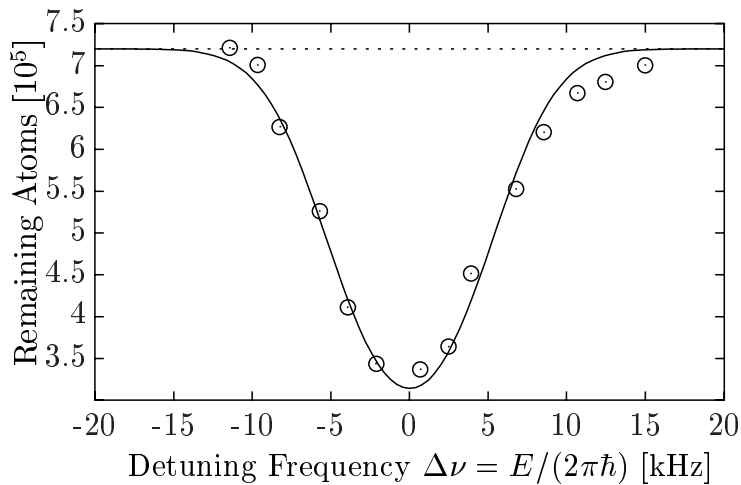


Figure 8.2: Number of atoms remaining in a Bose-Einstein condensate $N(T)$ after continuous release of atoms for $T = 20$ ms as a function of the detuning frequency $\Delta\nu$. Circles: Measurement by Bloch et al. reported in [GBA01]. Solid line: Theoretical prediction according to equations (7.13) and (8.16) with effective Gaussian condensate width $a = 2.8 \mu\text{m}$ and outcoupling strength $\Omega = 2\pi \cdot 105.585$ Hz.

radio frequencies. Also interference effects between condensates in two narrowly separated traps can be studied, since the beams from the adjacent traps will overlap at some distance from the condensate and form additional interference pattern.

8.5 Vortices and atom lasers

As mentioned in the introduction of this chapter, another indication of the quantum nature of BECs is the occurrence of superfluidity and the formation of quantized flux vortices. These states naturally arise in a rotating condensate or may be imprinted on a condensate by optical techniques [DGL⁺99]. For simplicity, we assume that the rotating BEC quantum fluid is in its thermodynamical ground state, where it exhibits a set of vortices (at least, one) symmetrically arranged in an extended lattice structure [ASRVK01, ECHC02].

8.5.1 Ideal atom laser from a single vortex

Here, we examine the atom laser beam arising in the presence of a single vortex with fixed direction in a non-interacting boson gas in an isotropic trap. The wave function of the rotating condensate is then given by the first excited radial harmonic oscillator state [FS01] and drops to zero along the vortex line. (In practice, the vortex line is not stationary, but may precess slowly in time [HACC01].) For simplicity, we will first align the vortex to the direction of the gravitational force along the z -axis. This enforces the

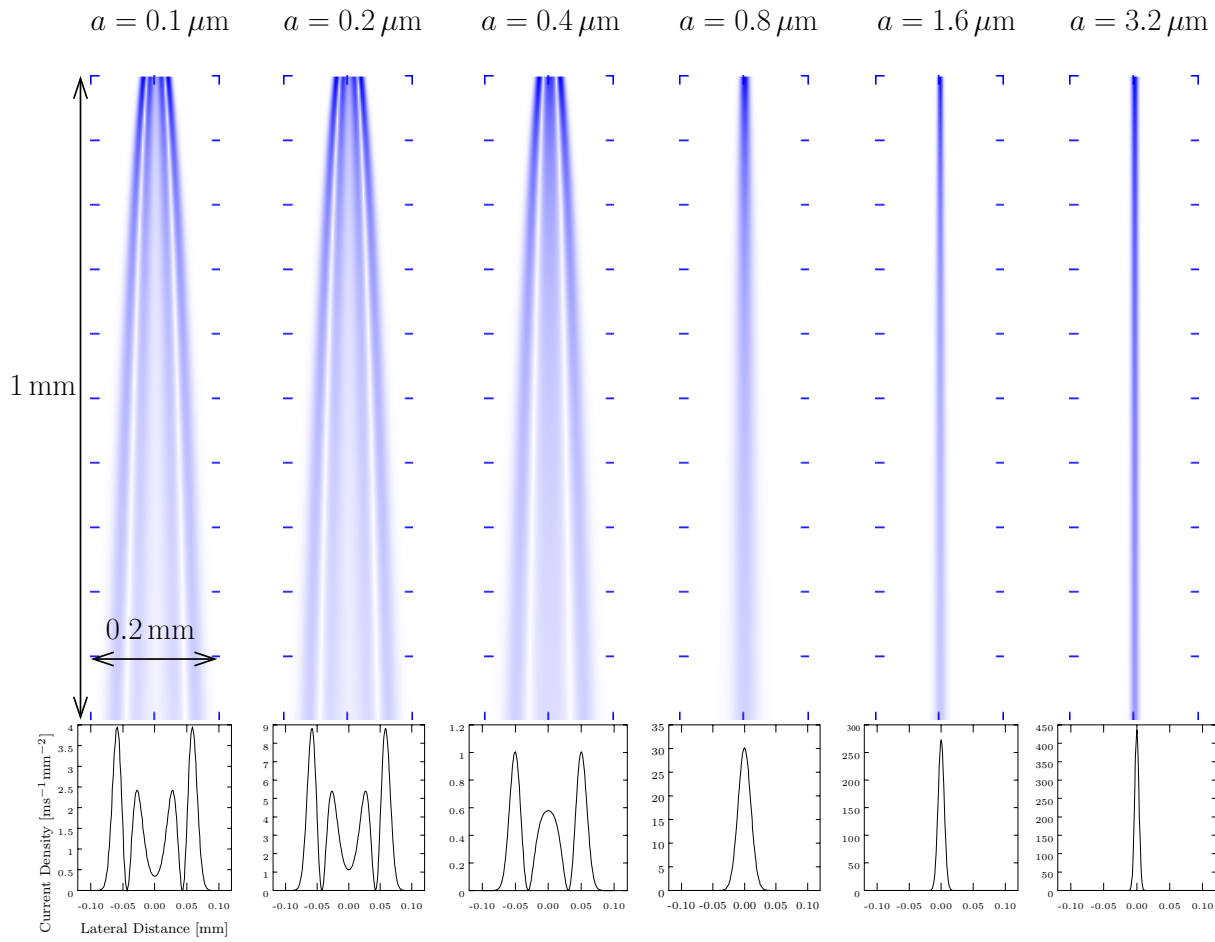


Figure 8.3: Transition from a strongly confined condensate to a more extended source distribution. There is rotational symmetry about the vertical axis. The source width is denoted by a . Interference fringes are clearly seen for $a \leq 0.4 \mu\text{m}$. Parameter: $\Delta\nu = E/(2\pi\hbar) = 2.5 \text{ kHz}$, $F = m_{\text{Rb}} g$, with $g = 9.81 \text{ m/s}^2$, and $m_{\text{Rb}} = 87 \text{ u}$.

oscillator eigenstate with angular momentum $l = m = 1$ as source wave function $\sigma_{11}(\mathbf{r})$. In analogy to the multipole source formalism presented in Section 3.4, application of the corresponding spherical tensor gradient $\mathbf{K}_{11}(\nabla)$ given in equation (3.38) to the vortex-free BEC ground state in equation (8.14) yields the corresponding vortex source-function

$$\sigma_{11}(\mathbf{r}) = N_1 \mathbf{K}_{11}(\nabla) \sigma(\mathbf{r}) = \frac{\sqrt{N} \hbar \Omega}{a^{5/2} \pi^{3/4}} (x + iy) e^{-r^2/2a^2}, \quad (8.17)$$

where $N_1 = a\sqrt{8\pi/3}$. In general, we define Gaussian multipole sources $\sigma_{lm}(\mathbf{r})$ analogous to equation (3.40) via

$$\sigma_{lm}(\mathbf{r}) = N_l \mathbf{K}_{lm}(\nabla) \sigma(\mathbf{r}), \quad (8.18)$$

where the constant $N_l^2 = 2\pi^{3/2}a^{2l}/\Gamma(l+3/2)$ is obtained from the normalization condition

$$\int d\mathbf{r} |\sigma_{lm}(\mathbf{r})|^2 = N(\hbar\Omega)^2. \quad (8.19)$$

The multipole source functions obtained in this way are the lowest-lying oscillator eigenstates of (l, m) spherical symmetry and with energy $E = (l+3/2)\hbar^2/Ma^2$. From equation (2.33) we evaluate the wave function $\psi_{lm}(\mathbf{r})$ of the corresponding out-coupled state

$$\psi_{lm}(\mathbf{r}) = (-1)^l N_l \int d^3r' \sigma(\mathbf{r}') K_{lm}(\nabla') G(\mathbf{r}, \mathbf{r}'; E). \quad (8.20)$$

Here, we integrated by parts to shift the spherical tensor operator to the Green function. Furthermore, the following substitution rule allows us to replace derivatives of $G_{\text{field}}(\mathbf{r}, \mathbf{r}'; E)$ with respect to the source location \mathbf{r}' by derivatives with respect to \mathbf{r} and the energy E . One easily verifies that indeed

$$\left(\frac{\partial}{\partial \xi'}, \frac{\partial}{\partial \nu'}, \frac{\partial}{\partial \zeta'} \right) G_{\text{field}}(\boldsymbol{\rho}, \boldsymbol{\rho}'; \epsilon) = - \left(\frac{\partial}{\partial \xi}, \frac{\partial}{\partial \nu}, \frac{\partial}{\partial \zeta} + 2 \frac{\partial}{\partial \epsilon} \right) G_{\text{field}}(\boldsymbol{\rho}, \boldsymbol{\rho}'; \epsilon). \quad (8.21)$$

Using this knowledge we obtain the multipole beam wave function in terms of derivatives of the known atom laser wave function for zero angular momentum $\psi(\mathbf{r})$ given in equation (7.11)

$$\psi_{lm}(\mathbf{r}) = N_l K_{lm} [\partial_x, \partial_y, \partial_z - F\partial_E] \psi(\mathbf{r}). \quad (8.22)$$

For multipole sources a more compact notation employs the special functions Q_k , defined in Appendix B. The atomic beam function for $l=0, m=0$ in terms of the Q_k function reads

$$\psi(\mathbf{r}) = -4\beta(\beta F)^3 \Lambda(\tilde{\epsilon}) Q_1(\tilde{\boldsymbol{\rho}}, \tilde{\zeta}; \tilde{\epsilon}), \quad (8.23)$$

where

$$\Lambda(\tilde{\epsilon}) = \sqrt{N}\hbar\Omega(2\sqrt{\pi}a)^{3/2} e^{2\alpha^2(\tilde{\epsilon}-4\alpha^4/3)}. \quad (8.24)$$

With the help of the differentiation rules given in equations (B.3) and (B.4), the derivatives originating from the spherical tensor operator K_{lm} can be expressed as a sum over Q_k -terms of higher order k . For a single vortex, it suffices to consider the sources $\sigma_{1m}(\mathbf{r})$ with $l=1$, and $m=0, \pm 1$:

$$\psi_{10}(\boldsymbol{\rho}) = 4\sqrt{2}\beta(\beta F)^3 \alpha \Lambda(\tilde{\epsilon}) \left[2\tilde{\zeta} Q_2(\tilde{\boldsymbol{\rho}}, \tilde{\zeta}; \tilde{\epsilon}) - 4\alpha^2 Q_1(\tilde{\boldsymbol{\rho}}, \tilde{\zeta}; \tilde{\epsilon}) + Q_0(\tilde{\boldsymbol{\rho}}, \tilde{\zeta}; \tilde{\epsilon}) \right], \quad (8.25)$$

$$\psi_{1\pm 1}(\boldsymbol{\rho}) = \mp 8\beta(\beta F)^3 \alpha \Lambda(\tilde{\epsilon}) \left(\tilde{\xi} \pm i\tilde{\nu} \right) Q_2(\tilde{\boldsymbol{\rho}}, \tilde{\zeta}; \tilde{\epsilon}). \quad (8.26)$$

Note that $\psi_{1\pm 1}$ vanishes on the z -axis: For a parallel orientation of the vortex line and the gravitational force, the empty vortex core is preserved in the atom laser profile. In analogy to Section 8.4, we calculate the overall out-coupling rate as a function of the radiation frequency detuning ($E = h\Delta\nu$). According to equation (3.53), the total multipole current is available from

$$J_{lm}(E) = -\frac{2}{\hbar} \Im [\langle \sigma_{lm} | G | \sigma_{lm} \rangle]. \quad (8.27)$$

Like the point source currents (to which they reduce as $\alpha \rightarrow 0$), the Gaussian multipole currents are expressed using the auxiliary functions $Q_{i_k}(\tilde{\epsilon})$ covered in Appendix B. Within the $l = 1$ triplet, the expressions for the total currents explicitly read

$$J_{10}(\tilde{\epsilon}) = \frac{32}{\hbar} \beta(\beta F)^3 \alpha^2 \Lambda(\tilde{\epsilon})^2 [Q_{i_2}(\tilde{\epsilon}) + 8\alpha^4 Q_{i_1}(\tilde{\epsilon}) - 4\alpha^2 Q_{i_0}(\tilde{\epsilon}) + \frac{1}{2} Q_{i_{-1}}(\tilde{\epsilon})], \quad (8.28)$$

$$J_{1\pm 1}(\tilde{\epsilon}) = \frac{32}{\hbar} \beta(\beta F)^3 \alpha^2 \Lambda(\tilde{\epsilon})^2 Q_{i_2}(\tilde{\epsilon}). \quad (8.29)$$

Thanks to the preserved rotational symmetry of the system, all total current matrix elements $J_{lm,l'm'}(\tilde{\epsilon})$ with $m \neq m'$ vanish, as indicated in Section 3.4.1. If $\tilde{\epsilon}$ is large, i. e., for extended condensates with $\alpha \gg 1$, we may replace the functions $Q_{i_k}(\tilde{\epsilon})$ by their asymptotic series. Further expanding the currents around their maximum near $\epsilon = 0$, we obtain their large-source approximations:

$$J_{10}(\tilde{\epsilon}) \sim N \sqrt{\pi} \beta \hbar \Omega^2 \frac{\epsilon^2}{\alpha^3} e^{-\epsilon^2/4\alpha^2}, \quad (8.30)$$

$$J_{1\pm 1}(\tilde{\epsilon}) \sim 2N \sqrt{\pi} \hbar \Omega^2 \frac{\beta}{\alpha} e^{-\epsilon^2/4\alpha^2}. \quad (8.31)$$

As expected from the earlier results for a simple Gaussian source, these currents can be interpreted as the integrated condensate density along a slice through the BEC at a height z fixed by the “resonance condition” $E + Fz = 0$:

$$J_{lm}(E) \sim \frac{2\pi}{\hbar} \int d^3\mathbf{r} |\sigma_{lm}(\mathbf{r})|^2 \delta(E + Fz). \quad (8.32)$$

For illustration, we consider two orientations of the vortex with respect to the gravitational force \mathbf{F} . A vortex parallel to the field is simply represented by the Gaussian condensate wave function $\sigma_{11}(\mathbf{r})$ given in equation (8.17). The beam wave function and the total current are stated in equations (8.26) and (8.29), respectively. A different expression arises for the case of a vortex along the x -axis, i. e., perpendicular to \mathbf{F} . The corresponding BEC source function $\sigma_{1\perp}(\mathbf{r})$ is connected to the parallel vortex model by a rotation $\exp(-i\pi\hat{L}_y/2)$. Application of the $l = 1$ rotation matrix for angular momentum eigenstates [Edm57] yields the following source term

$$\sigma_{1\perp}(\mathbf{r}) = \frac{1}{2} \left[\sigma_{11}(\mathbf{r}) + \sqrt{2} \sigma_{10}(\mathbf{r}) + \sigma_{1,-1}(\mathbf{r}) \right], \quad (8.33)$$

with a corresponding superposition of equations (8.25) and (8.26) as beam wave function $\psi_{1\perp}(\mathbf{r})$. Also, the associated total current becomes

$$J_{1\perp}(\tilde{\epsilon}) = \frac{1}{2} [J_{11}(\tilde{\epsilon}) + J_{10}(\tilde{\epsilon})]. \quad (8.34)$$

Figure 8.4 depicts the total currents generated by an ideal ^{87}Rb BEC of width $a = 2 \mu\text{m}$. For this choice of parameters we have $\alpha \approx 3.33$, so that the effective energy $\tilde{\epsilon} = 4\alpha^4$ of the

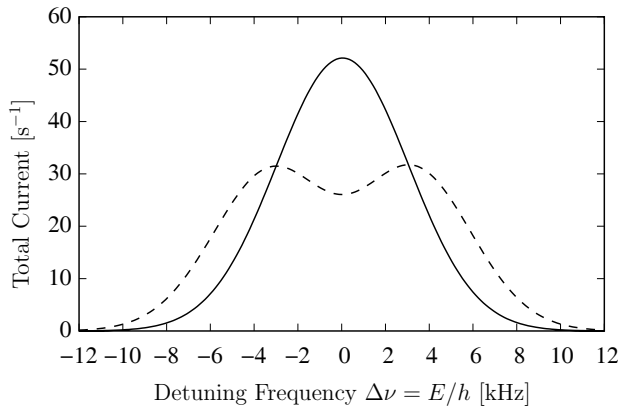


Figure 8.4: Total current generated per atom in a ^{87}Rb BEC with one vortex as a function of the detuning frequency $\Delta\nu$. Solid line: The source $\sigma_{11}(\mathbf{r})$ (8.17) with the vortex line parallel to the gravitational field \mathbf{F} . Dashed line: Vortex line perpendicular to \mathbf{F} , represented by $\sigma_{1\perp}(\mathbf{r})$ (8.33). Parameters: $a = 2 \mu\text{m}$, $\Omega = 2\pi \times 100 \text{ Hz}$.

assigned virtual point source indicates tunneling emission. While in parallel orientation the current distribution is simply Gaussian, it features a dip in the total current at $\Delta\nu = 0$ for a vortex line perpendicular to the gravitational field. This behavior is easily understood from equation (8.32): Due to the presence of the vortex line in the slicing plane, at $z = 0$ the condensate density adopts a minimum. We note that the reflection approximation fails for small condensates (with $\alpha \sim 1$) and it becomes necessary to use the exact results given in equations (8.28) and (8.29). The corresponding density profiles at a distance $z = 1 \text{ mm}$ for three different energies ($\Delta\nu = 0, \pm 4 \text{ kHz}$) are shown in Figure 8.5. Interestingly, the sign of the detuning influences the density profile. Even though the total current is almost the same for $\Delta\nu = \pm 4 \text{ kHz}$, the density shows a different pattern for both frequencies. For tunneling sources, we expect density profiles of overall Gaussian shape, with a mean width $D(z) = 2\tilde{z}/\tilde{\kappa}$, where $\tilde{z} = (\zeta + 2\alpha^4)/\beta F$ and $\tilde{\kappa} = 4\beta F\alpha^2$ denote the distance from the virtual source and the virtual evanescent wave number, respectively [BBG⁺98]. However, this Gaussian envelope is modulated by a factor $f(\xi, \nu)$ that depends on the relative orientation of the vortex and the gravitational force. A fairly cumbersome calculation yields for the asymptotic shape of the density profiles generated by the sources given by equations (8.17) and (8.33) in the far-field sector and for $\alpha \gg 1$:

$$\rho(\xi, \nu) \sim 16N(\hbar\Omega)^2\beta^5 F^3\alpha^3 \frac{f(\xi, \nu)}{\sqrt{2\pi\zeta}(\zeta + 2\alpha^4)^2} \exp\left[-\left(\frac{\epsilon^2}{4\alpha^2} + \frac{2\alpha^2(\xi^2 + \nu^2)}{\zeta + 2\alpha^4}\right)\right], \quad (8.35)$$

where the modulation factors $f_{11}(\xi, \nu)$ and $f_{1\perp}(\xi, \nu)$ for parallel and perpendicular orientation read

$$f_{11}(\xi, \nu) = \xi^2 + \nu^2, \quad f_{1\perp}(\xi, \nu) = \frac{\epsilon^2}{4} + \left(\nu - \frac{\epsilon\sqrt{\zeta}}{2\sqrt{2}\alpha^2}\right)^2. \quad (8.36)$$

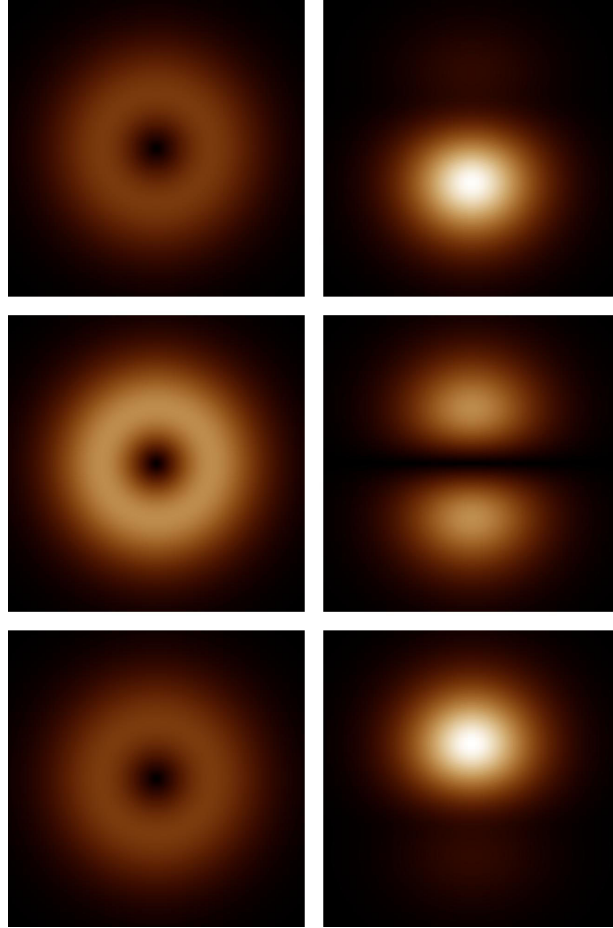


Figure 8.5: Atom laser density profiles for a rotating ^{87}Rb BEC source sustaining one vortex. Left column: Parallel orientation of vortex line and force \mathbf{F} , with source $\sigma_{11}(\mathbf{r})$ (8.17). Right column: Vortex perpendicular to \mathbf{F} , as given by $\sigma_{1\perp}(\mathbf{r})$ (8.33). The detuning frequencies $\Delta\nu$ are -4 kHz (top row), 0 kHz (center row), and $+4$ kHz (bottom row), respectively. The brightest spots of the distribution pertain to a density of 2.5 atoms/ μm^3 . Displayed area: $30\ \mu\text{m} \times 30\ \mu\text{m}$, distance from source: $z = 1$ mm; source parameters: $a = 2\ \mu\text{m}$, $\Omega = 2\pi \times 100$ Hz, $N = 10^6$ atoms.

All quantities are expressed in the dimensionless coordinates introduced in equation (7.4). In the parallel case the vortex core is preserved in the beam profile, since $f_{1\perp}(\xi = 0, \nu = 0) = 0$. The dependence of $f_{1\perp}(\xi, \nu)$ on the source distance ζ and the detuning $\nu = -\epsilon/2\hbar\beta$ renders the atom laser profiles generated in perpendicular orientation more intriguing. The detuning-dependent, isotropic contribution $\epsilon^2/4$ competes with a shifted parabolic term that grows linearly with the detector distance ζ . For $\zeta \ll 2\alpha^4$, detuning blurs the simple vortex image present at center resonance, while for $\zeta \gg 2\alpha^4$ the latter term in equation (8.36) dominates, causing the appearance of a node line in the profile whose relative position shifts linearly with the detuning ν . The transition between these markedly different regimes of the atom laser occurs at considerable distance from the BEC. In our example, we find $\zeta = 2\alpha^4$ for a separation $z \approx 150 \mu\text{m}$, and the figure depicts the far-field behavior. However, for larger sources, this characteristic distance quickly reaches macroscopic dimensions: For an atom laser supplied by a BEC of width $a = 10 \mu\text{m}$, we find $z \approx 10 \text{ cm}$!

8.5.2 Vortex lattices

Using the tools developed in the previous section, we proceed to give an example of a multipole source where larger values of the angular momentum are present. Rotating Bose-Einstein condensates show superfluid behavior and respond to an externally induced rotation by formation of a vortex lattice [MAH⁺99, MCWD00, ASRVK01, ECHC02]. (For a review on vortices in BECs, see [FS01].) No attempt at a description of the formation and parameters of this lattice will be made. Rather, we present a theoretical model for a stationary atom laser supplied by an already formed vortex lattice, with vortex lines oriented parallel to the gravitational field \mathbf{F} . The wave function of the lattice state (the laser source) is most conveniently modeled in the rotating reference frame (rf), where it becomes time-independent; we denote it by $\sigma_{\text{latt,rf}}(\mathbf{r})$. However, the laser is observed in the laboratory frame and hence we first discuss the transformation between both frames.

In the laboratory frame (lf), the rotating-frame source function $\sigma_{\text{latt,rf}}(\mathbf{r})$ becomes explicitly time dependent. The transformation between both frames of reference involves a uniform rotation around the z -axis with frequency Ω_{rot} , which is generated by the unitary operator $\exp(-iL_z\Omega_{\text{rot}}t/\hbar)$. The full time-dependent source term in the lab frame consequently reads $\sigma_{\text{latt,lf}}(\mathbf{r}, t) = e^{-iEt/\hbar}e^{-iL_z\Omega_{\text{rot}}t/\hbar}\sigma_{\text{latt,rf}}(\mathbf{r})$. Here, decomposition of the source $\sigma_{\text{latt,rf}}(\mathbf{r})$ into a superposition of eigenstates $\sigma_{m,\text{rf}}(\mathbf{r})$ of L_z makes sense:

$$\sigma_{\text{latt,rf}}(\mathbf{r}) = \sum_m \sigma_{m,\text{rf}}(\mathbf{r}) . \quad (8.37)$$

Thus, in the laboratory frame, the rotating source function appears split into stationary components $\sigma_{m,\text{rf}}(\mathbf{r})$ shifted in energy. With $E_m = E + m\hbar\Omega_{\text{rot}}$, we obtain

$$\sigma_{\text{latt,lf}}(\mathbf{r}, t) = \sum_m e^{-iE_m t/\hbar} \sigma_{m,\text{rf}}(\mathbf{r}) . \quad (8.38)$$

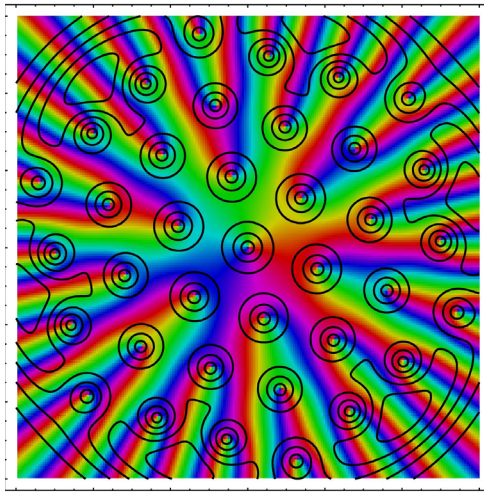


Figure 8.6: BEC wave function $\sigma_{\text{rf}}(\mathbf{r})$ with 37 vortices. Vortex spacing $10 \mu\text{m}$. Size parameter $a = 5 \mu\text{m}$. The black lines are lines of constant density and shading denotes the phase.

The atomic beam wave function resulting from a time-dependent source in the presence of the gravitational field is propagated by the linear field propagator

$$\psi_{\text{latt,lf}}(\mathbf{r}, t) = -\frac{i}{\hbar} \int d^3\mathbf{r}' \int_{-\infty}^t dt' K_{\text{field}}(\mathbf{r}, t|\mathbf{r}', t') \sigma_{\text{latt,lf}}(\mathbf{r}', t'). \quad (8.39)$$

Employing the propagator representation of the field Green function from equation (2.15), we finally obtain for the beam wave function the expression

$$\psi_{\text{latt,lf}}(\mathbf{r}, t) = \sum_m e^{-iE_m t/\hbar} \psi_{m,\text{rf}}(\mathbf{r}), \quad (8.40)$$

where

$$\psi_{m,\text{rf}}(\mathbf{r}) = \int d^3\mathbf{r}' G_{\text{field}}(\mathbf{r}, \mathbf{r}'; E_m) \sigma_{m,\text{rf}}(\mathbf{r}'). \quad (8.41)$$

We note that both $\psi_{m,\text{rf}}(\mathbf{r})$ and its source $\sigma_{m,\text{lf}}(\mathbf{r})$ are eigenfunctions of L_z . This shows that like the BEC, the atomic beam profile rotates uniformly with frequency Ω_{rot} . Next, we further characterize the source function $\sigma_{\text{latt,rf}}(\mathbf{r})$ for the vortex lattice. This state of the BEC is commonly described as a superposition of angular momentum eigenstates of the harmonic oscillator [BR99, Ho01]. The number of vortices and their positions are available from minimizing the energy functional of the Gross-Pitaevskii equation in the rotating frame. For a parallel arrangement of the vortices and the gravitational field \mathbf{F} , we may model the vortex state as a product of a two-dimensional ‘‘lattice function’’ $\sigma_{2D}(x, y)$ detailing the vortex positions (x_k, y_k) with a Gaussian envelope enforced by the harmonic trap potential. Introducing complex coefficients $v_k = x_k + iy_k$, the lattice function is

obtained as a product involving all vortex positions that alternatively may be expressed as a polynomial in $(x + iy)$,

$$\sigma_{2D}(x, y) = \prod_{k=1}^n [(x + iy) - v_k] = \sum_{k=0}^n w_k^{(n)} (x + iy)^k. \quad (8.42)$$

The coefficients w_k are linked to v_k via the recursion relation

$$w_k^{(n)} = w_{k-1}^{(n-1)} - v_{k+1} w_k^{(n-1)}, \quad \text{with } w_0^{(0)} = 1. \quad (8.43)$$

Usually, these lattices possess elements of symmetry which enforce selection rules on the w_k , leaving only few non vanishing coefficients. The complete three-dimensional source function in the rotating frame then reads

$$\sigma_{\text{latt,rf}}(\mathbf{r}) = N_n \exp\left(-\frac{x^2 + y^2}{2a_x^2} - \frac{z^2}{2a_z^2}\right) \sigma_{2D}(x, y). \quad (8.44)$$

The constant N_n is determined by the normalization condition $\int d^3\mathbf{r} |\sigma(\mathbf{r})_{\text{latt,rf}}|^2 = N(\hbar\Omega)^2$:

$$N_n = \frac{\sqrt{N} \hbar\Omega}{\pi^{3/4} \sqrt{a_z \sum_{k=0}^n k! |w_k^{(n)}|^2 a_x^{2k+2}}}. \quad (8.45)$$

From equation (8.42) the decomposition of $\sigma_{\text{latt,rf}}(\mathbf{r})$ into eigenstates $\sigma_{m,\text{rf}}(\mathbf{r})$ of L_z is readily obtained

$$\sigma_{m,\text{rf}}(\mathbf{r}) = N_n w_m^{(n)} (x + iy)^m \exp\left(-\frac{x^2 + y^2}{2a_x^2} - \frac{z^2}{2a_z^2}\right). \quad (8.46)$$

Thus, all $n + 1$ source components are eigenstates of the harmonic trap potential, and the highest quantum number m equals the number of vortices present in the BEC.

For the special case of an isotropic trap ($a_x = a_z = a$), the theory outlined above provides both out-coupling rate and beam profile in analytic form. Since the components $\sigma_{m,\text{rf}}(\mathbf{r})$ then simultaneously present eigenstates of L_z and the total angular momentum L^2 with quantum number $l = m$, the source is entirely made up from circular Gaussian multipole states $\sigma_{mm}(\mathbf{r}) = N_m K_{mm}(\nabla)\sigma(\mathbf{r})$:

$$\sigma_{m,\text{rf}}(\mathbf{r}) = C_n \sqrt{m!} w_m^{(n)} a^m \sigma_{mm}(\mathbf{r}), \quad (8.47)$$

where $C_n^2 = [\sum_{k=0}^n k! |w_k^{(n)}|^2 a^{2k}]^{-1}$ denotes the normalization constant. According to equation (8.40), the rotating beam is thus produced by a weighed superposition of stationary sources $\sigma_{mm}(\mathbf{r})$ with effective energy $E_m = E + m\hbar\Omega_{\text{rot}}$. As explained in Section 7.1, outside the source region each Gaussian multipole source $\sigma_{lm}(\mathbf{r})$ in expression (8.18) may be mapped onto a corresponding displaced virtual point source of adjusted strength $\Lambda(\tilde{\epsilon})$. This allows to calculate the wave function $\psi_{mm}(\mathbf{r})$ generated by $\sigma_{mm}(\mathbf{r})$ along the lines

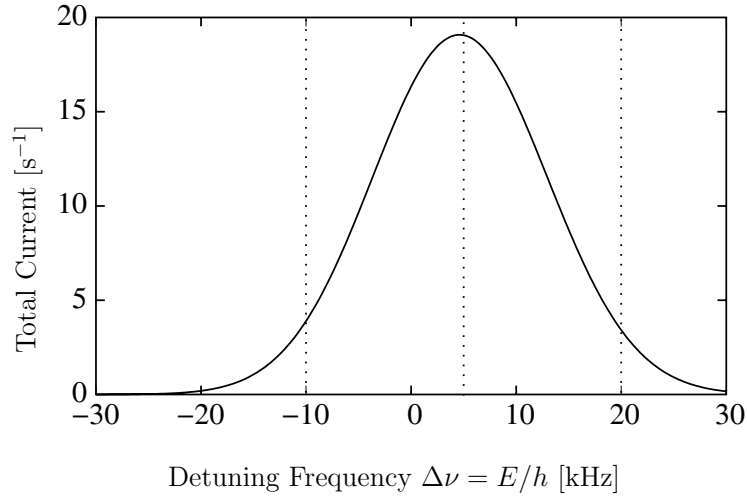


Figure 8.7: Total current per atom in a ^{87}Rb BEC with 37 vortices as a function of detuning frequency $\Delta\nu$. The vortex structure of the BEC is not visible in the integrated current. Vortex separation in the BEC: $10\ \mu\text{m}$, rotation frequency $\Omega_{\text{rot}} = 2\pi \times 250\ \text{Hz}$, out-coupling strength $\Omega = 2\pi \times 100\ \text{Hz}$, size parameter $a = 5\ \mu\text{m}$.

presented in Section 8.5.1, and the final result closely resembles the corresponding linear field multipole Green function $G_{mm}(\mathbf{r}, \mathbf{o}; E)$:

$$\psi_{mm}(\mathbf{r}) = -\frac{4\beta(\beta F)^3}{\sqrt{m!}} \Lambda(\tilde{\epsilon}_m) [2\alpha(\xi + i\nu)]^m \text{Q}_{m+1}(\tilde{\rho}, \tilde{\zeta}; \tilde{\epsilon}_m), \quad (8.48)$$

where $\tilde{\epsilon}_m = -2\beta E_m + 4\alpha^4$ denotes the shifted and scaled energy parameter. Similarly, the total current $J_{mm}(E_m)$ generated by $\sigma_{mm}(\mathbf{r})$ is available and reads

$$J_{mm}(E_m) = \frac{8}{\hbar} \beta(\beta F)^3 (2\alpha)^{2m} \Lambda(\tilde{\epsilon}_m)^2 \text{Qi}_{m+1}(\tilde{\epsilon}_m). \quad (8.49)$$

Substituting equations (8.47) and (8.48) into expression (8.40), the wave function of the rotating atom laser beam ultimately becomes

$$\psi_{\text{latt,lf}}(\mathbf{r}, t) = C_n \sum_{m=0}^n e^{-iE_m t/\hbar} \sqrt{m!} w_m^{(n)} a^m \psi_{mm}(\mathbf{r}). \quad (8.50)$$

Due to cylindrical symmetry, all elements of the total current matrix $J_{lm,l'm'}(E)$ in equation (3.53) with $m \neq m'$ vanish (see Section 3.4.1). Therefore, the (stationary) out-coupling rate $J_{\text{latt}}(E)$ reduces to a properly weighed sum of the ballistic multipole currents $J_{mm}(E_m)$ given in equation (8.49):

$$J_{\text{latt}}(E) = C_n^2 \sum_{m=0}^n m! |w_m^{(n)}|^2 a^{2m} J_{mm}(E_m). \quad (8.51)$$

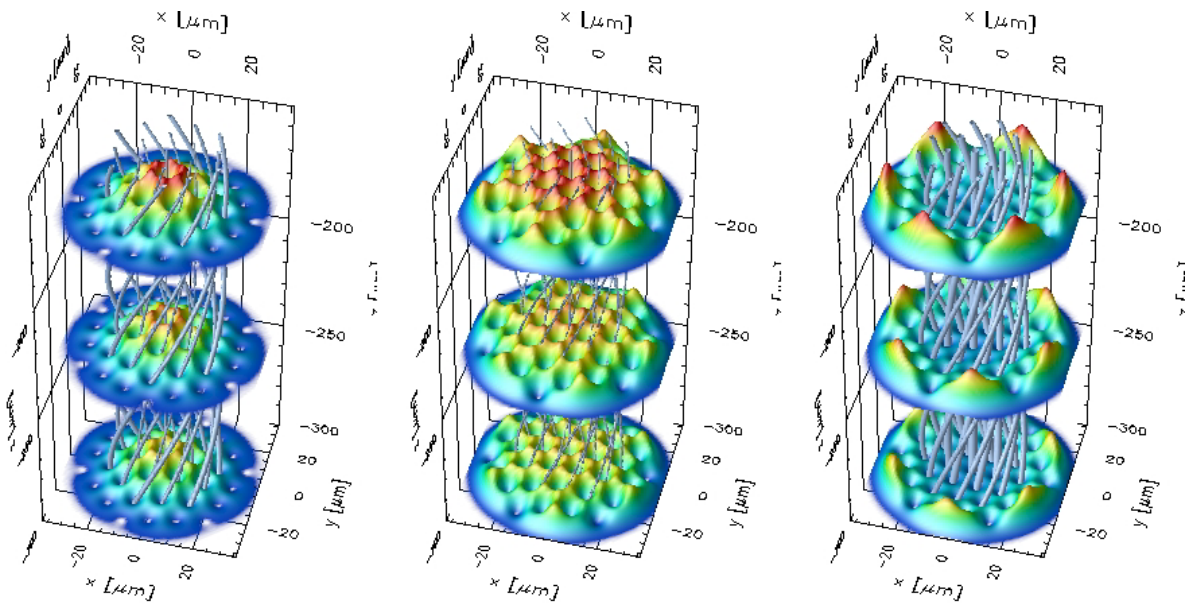


Figure 8.8: Beam profile of an atom laser from a BEC with 37 vortices at different energies and heights. We plot the density distribution on three different slices through the beam. Also, at all distances the vortex cores are indicated by small tubes. From the left figure to the right one we vary the detuning frequency ($-10, 5, 20$) kHz. These frequencies are marked by dotted lines in Figure 8.7. The three distances chosen are $(177, 239, 300)$ μm from the center of the BEC. For other BEC parameters see Figure 8.7.

We illustrate these results by using a model condensate featuring a symmetrical triangular lattice of 37 vortices, with a distance between the vortices of $10 \mu\text{m}$, embedded into a Gaussian source of width $a = 5 \mu\text{m}$. A sketch of the resulting density distribution is shown in Figure 8.6. While the frequency dependence of the out-coupling rate merely shows the familiar Gaussian character (compare Figures 8.4 and 8.7), plots of the resulting atom laser profile exhibit rich detail (Figure 8.8): Tracing the rotation of the source, the vortex pattern, which is fully transferred from the BEC into the laser beam, forms an intertwined braid-like structure along the z -axis. It modulates the lateral beam profile which now strongly depends on the detuning frequency $\Delta\nu$. The out-coupling rate varies between the different angular momentum components $\sigma_{m, \text{rf}}(\mathbf{r})$ (8.47) that make up the source. A negative shift in the frequency suppresses states with high $|m|$, leading to an approximate Gaussian shape of the particle distribution, whereas positive detuning ($\Delta\nu > 0$) emphasizes these contributions. The centrifugal barrier effective for them then produces a ring-like “crown” emission pattern.

Chapter 9

Summary

The careful analysis of the energy-dependent Green function in at most quadratic potentials proved very rewarding for a variety of physical systems. Besides the availability of the quantum mechanical solution, the consistent treatment of interference phenomena connected to classical trajectories is a key element for an interpretation of the structures arising in the generated currents. A good example is the controllable field-slit proposed in Chapter 2. Choosing a suitable Hilbert space for the propagator simplifies the calculation of Green functions considerably. We examined the **energy-dependent Green function** in momentum, position and Bargmann space. By giving a number of tutorial examples and applications, we immediately took advantage of the underlying mathematical theorems. From a physical point of view, we should stress that the energy-dependent Green function is much more than merely a Laplace transform of the quantum propagator. **Only the energy-dependent Green function can provide the bridge to experiments and the real world**, since most processes in quantum mechanics are observed at a given energy, not time. Its analytic structure differs completely from the propagator and none of the available methods for the calculation of Feynman kernels are applicable for the analytic computation of the Green function.

A comprehensive analysis of **photodetachment experiments in external electromagnetic fields** was carried out. Specifically, the addition of a magnetic field to a uniform electric field gives rise to a number of newly predicted effects and phenomena. Using the theory of multipole sources, we presented for the first time a systematic study of the scattering currents in parallel magnetic and electric fields. The closed analytic form enables us to go beyond the known set of p-wave currents and to give quantitative predictions for the total current of arbitrary multipole sources. Also, we have direct access to the corresponding current density distribution which shows intricate structures. We attributed these structures to the **interference of multiple classical trajectories**. Besides this classical regime, the derived quantum solution allows us to investigate the limit of small energies. Here, the Heisenberg uncertainty principle governs the distribution and therefore leads again to an intelligible interpretation of the current distribution. All given results are highly relevant to present-day photodetachment experiments. The very sensitive photodetachment microscope of Blondel is carefully shielded against the magnetic field of the

earth, since even a tiny magnetic flux distorts and changes the images dramatically.

Knowing the analytic properties of the propagator, we could tackle the problem of finding the **Green function in crossed electric and magnetic fields**. An analytic solution is given in the two-dimensional case. There, the local density of states, linked to the imaginary part of the energy-dependent Green function, is represented by shifted harmonic oscillator eigenstates. However, these states are a function of the energy and not the position operator. By employing two different approaches to obtain this result, we gained more insight into the structure of the Green function and could identify the canonical transformation and its unitary transformation that map the position variable to the energy. **The combination of electric and magnetic fields has profound impacts on the density of states which have not been considered before.** The singularities present in a purely magnetic field disappear and are replaced by the smoother oscillator functions. Prototype calculations of the Hall resistivity show a wealth of interesting features and the existence of **fractional plateaus in the quantum Hall effect**. The derived electric and magnetic field dependence of the **breakdown of the integer quantum Hall effect** is in excellent agreement with experimental results. In principle, a three-dimensional extension of the quantum Hall effect should be observable in photodetachment experiments, as our calculations for the cross-sections show. Again, the Green function provides an excellent tool to derive and analyze the expected currents in these experiments.

In the presence of a vector potential, the important question of **gauge invariance of the currents** arises. We answered this question by relating the gauge-transformation to a relocation of the coordinate system.

The combination of extended sources with the previously derived Green functions leads to other applications of the theory of quantum sources. We applied the theory to **matter waves originating from a Bose-Einstein condensate**. Again, the given solutions cover a wide range of emission characteristics of such an atom source. The progress in trapping techniques (microtraps) and the possibility of sustaining a condensate by refilling render the presented model highly relevant. The detailed expressions for the range of operation of an atom laser and the resulting matter waves are needed for a theoretical description of newly developed technologies like matter-wave guides and atom beam interferometers. The **interference of atomic matter waves** from different sources could probe the relative phase relation of neighboring condensates and detect changes due to external potentials. Another application is the production of **tailored wave functions** by employing a superposition of atomic matter waves with different emission energies.

The Green function and quantum source formalism is not limited to the ground state of a condensate. Excited states of rotating condensates bear flux vortices and are included in our theory. The presence of these excitations is reflected in the predicted beam profiles and suggests the **use of atom lasers as a monitoring device** for the time-evolution of a macroscopic quantum state.

Yet another field of physics is accessible by the energy-dependent Green function. The transition from a bound state to a continuum state of a molecule is a standard topic of the **theory of Franck-Condon factors**. By providing reference cases for Franck-Condon factors in several dimensions and for different potentials, we compared commonly applied

approximation schemes like the so-called reflection approximation with the newly obtained exact results. The **derivation of the reflection approximation** in terms of the energy-dependent Green function and the subsequent analysis of its validity show that quantum interferences are persistent in these transitions and cannot be automatically included in simple approximation schemes.

The given results surely represent only a glimpse of how many modern-day experiments can be described in terms of energy-dependent Green functions.

Appendix A

Linear canonical transformation of a quadratic Hamiltonian

A.1 Evaluation of the matrix representation

Using the commutation rules, the matrix $\hat{\mathbb{k}}$ can be easily computed for at most quadratic Hamiltonians. Upon inserting the commutator from equation (3.31) into equation (3.28) we get (all operators are in the Heisenberg picture)

$$\begin{aligned}
 \begin{pmatrix} \mathbf{x}(t) \\ -\mathbf{p}(t) \\ \mathbf{1} \end{pmatrix} &= \mathbf{U}^\dagger(t) \circ \begin{pmatrix} \mathbf{x}(0) \\ -\mathbf{p}(0) \\ \mathbf{1} \end{pmatrix} \circ \mathbf{U}(t) \\
 &= \begin{pmatrix} \mathbf{x}(0) \\ -\mathbf{p}(0) \\ \mathbf{1} \end{pmatrix} + \frac{it}{\hbar} \left[\mathbf{H}, \begin{pmatrix} \mathbf{x}(0) \\ -\mathbf{p}(0) \\ \mathbf{1} \end{pmatrix} \right] + \frac{1}{2!} \left(\frac{it}{\hbar} \right)^2 \left[\mathbf{H}, \left[\mathbf{H}, \begin{pmatrix} \mathbf{x}(0) \\ -\mathbf{p}(0) \\ \mathbf{1} \end{pmatrix} \right] \right] + \dots \\
 &= \begin{pmatrix} \mathbf{x}(0) \\ -\mathbf{p}(0) \\ \mathbf{1} \end{pmatrix} + \frac{it}{\hbar} (-i\hat{\mathbb{k}}) \begin{pmatrix} \mathbf{x}(0) \\ -\mathbf{p}(0) \\ \mathbf{1} \end{pmatrix} + \frac{1}{2!} \left(\frac{it}{\hbar} \right)^2 (-i\hat{\mathbb{k}})^2 \begin{pmatrix} \mathbf{x}(0) \\ -\mathbf{p}(0) \\ \mathbf{1} \end{pmatrix} + \dots \\
 &= \exp \left(\hat{\mathbb{k}}t \right) \begin{pmatrix} \mathbf{x}(0) \\ -\mathbf{p}(0) \\ \mathbf{1} \end{pmatrix}. \tag{A.1}
 \end{aligned}$$

Thus we obtain the desired result

$$\hat{\mathbb{g}}(t) = \exp \left(\hat{\mathbb{k}}t \right).$$

A.2 Homogeneous electric and magnetic fields at arbitrary angles

The Hamiltonian is given in equation (4.1) and reads

$$\mathbf{H} = \frac{\mathbf{p}_x^2 + \mathbf{p}_y^2 + \mathbf{p}_z^2}{2m} + \frac{1}{2}m\omega_L^2 (x^2 + y^2) + x\mathbf{F}_x + y\mathbf{F}_y + z\mathbf{F}_z - \mathbf{p}_y x \omega_L + \mathbf{p}_x y \omega_L. \quad (\text{A.2})$$

Using the results from the previous section we obtain

$$\left[\begin{array}{c} \mathbf{H}, \\ \left(\begin{array}{c} \mathbf{x}_1 \\ \mathbf{x}_2 \\ \mathbf{x}_3 \\ -\mathbf{p}_1 \\ -\mathbf{p}_2 \\ -\mathbf{p}_3 \\ \mathbf{1} \end{array} \right) \end{array} \right] = -i\hat{\mathbf{k}} \left(\begin{array}{c} \mathbf{x}_1 \\ \mathbf{x}_2 \\ \mathbf{x}_3 \\ -\mathbf{p}_1 \\ -\mathbf{p}_2 \\ -\mathbf{p}_3 \\ \mathbf{1} \end{array} \right),$$

where

$$\hat{\mathbf{k}} = \begin{pmatrix} 0 & \omega_L & 0 & -\frac{1}{m} & 0 & 0 & 0 \\ -\omega_L & 0 & 0 & 0 & -\frac{1}{m} & 0 & 0 \\ 0 & 0 & 0 & 0 & 0 & -\frac{1}{m} & 0 \\ m\omega_L^2 & 0 & 0 & 0 & \omega_L & 0 & -\mathbf{F}_x \\ 0 & m\omega_L^2 & 0 & -\omega_L & 0 & 0 & -\mathbf{F}_y \\ 0 & 0 & 0 & 0 & 0 & 0 & -\mathbf{F}_z \\ 0 & 0 & 0 & 0 & 0 & 0 & 0 \end{pmatrix}.$$

Standard techniques are used to evaluate the exponential of the matrix $\hat{\mathbf{k}}t$ (see also [Kra00]). We obtain

$$\begin{aligned} \hat{\mathbf{g}} &= \exp(\hat{\mathbf{k}}t) \\ &= \begin{pmatrix} \cos^2 \omega_L t & \frac{\sin(2\omega_L t)}{2} & 0 & -\frac{\sin(2\omega_L t)}{Be} & \frac{-1+\cos(2\omega_L t)}{Be} & 0 & \frac{\mathbf{F}_x(1-\cos(2\omega_L t))+\mathbf{F}_y(2\omega_L t-\sin(2\omega_L t))}{4m\omega^2} \\ -\frac{\sin(2\omega_L t)}{2} & \cos^2 \omega_L t & 0 & \frac{2\sin^2 \omega_L t}{Be} & -\frac{\sin(2\omega_L t)}{Be} & 0 & \frac{\mathbf{F}_y(1-\cos(2\omega_L t))+\mathbf{F}_x(-2\omega_L t+\sin(2\omega_L t))}{4m\omega^2} \\ 0 & 0 & 1 & 0 & 0 & -\frac{t}{M} & \frac{\mathbf{F}_z t^2}{2M} \\ \frac{Be \sin(2\omega_L t)}{4} & \frac{Be \sin^2 \omega_L t}{2} & 0 & \cos^2 \omega_L t & \frac{\sin(2\omega_L t)}{2} & 0 & \frac{-\mathbf{F}_y(1-\cos(2\omega_L t))-\mathbf{F}_x(2\omega_L t+\sin(2\omega_L t))}{4\omega_L^2} \\ -\frac{Be \sin^2 \omega_L t}{2} & \frac{Be \sin(\omega_L t)}{4} & 0 & -\frac{\sin(2\omega_L t)}{2} & \cos^2 \omega_L t & 0 & \frac{-\mathbf{F}_x(-1+\cos(2\omega_L t))-\mathbf{F}_y(2\omega_L t+\sin(2\omega_L t))}{4\omega_L^2} \\ 0 & 0 & 0 & 0 & 0 & 1 & -\mathbf{F}_z t \\ 0 & 0 & 0 & 0 & 0 & 0 & 1 \end{pmatrix}. \end{aligned} \quad (\text{A.3})$$

The classical equation of motion is readily extracted from this matrix. For $\mathbf{x}(0) = \mathbf{o}$, the expressions are:

$$\begin{aligned} x_1(t) &= \frac{\sin(2\omega_L t)}{Be} \mathbf{p}_1(0) - \frac{-1 + \cos(2\omega_L t)}{Be} \mathbf{p}_2(0) + \frac{\mathbf{F}_x(1 - \cos(2\omega_L t)) + \mathbf{F}_y(2\omega_L t - \sin(2\omega_L t))}{4m\omega_L^2}, \\ x_2(t) &= +\frac{2\sin^2\omega_L t}{Be} \mathbf{p}_1(0) - \frac{\sin(2\omega_L t)}{Be} \mathbf{p}_2(0) + \frac{\mathbf{F}_y(1 - \cos(2\omega_L t)) + \mathbf{F}_x(-2\omega_L t + \sin(2\omega_L t))}{4m\omega_L^2}, \\ x_3(t) &= \frac{1}{m} t \mathbf{p}_3(0) + \frac{1}{m} \frac{1}{2} \mathbf{F}_z t^2. \end{aligned} \tag{A.4}$$

Next we determine the 3×3 block-matrices α , β , ϑ , and δ defined by splitting $\hat{\mathfrak{g}}(t)$ into

$$\hat{\mathfrak{g}}(t) = \left(\begin{array}{cc|c} \alpha & \beta & \vec{\alpha}' \\ \vartheta & \delta & \vec{\alpha}'' \\ \hline 0 & 0 & 1 \end{array} \right),$$

and indeed get the propagator given in equation (4.17) by inserting the matrices into equation (3.32).

Appendix B

Integrals involving Airy functions

In the course of our investigation into ballistic multipole matter waves, integral expressions of the following type:

$$\mathbb{Q}_k(\rho, \zeta; \epsilon) = \frac{i}{2\pi\sqrt{\pi}} \int_0^\infty \frac{d\tau}{(i\tau)^{k+1/2}} \exp \left\{ i \left[\frac{\rho^2}{\tau} + \tau(\zeta - \epsilon) - \frac{\tau^3}{12} \right] \right\} \quad (\text{B.1})$$

are frequently encountered. For integer indices k , this set of integrals permits explicit evaluation in terms of products of Airy functions. Introducing the Airy Hankel function $\text{Ci}(u) = \text{Bi}(u) + i \text{Ai}(u)$ [AS65], the basic member of this class reads:

$$\mathbb{Q}_0(\rho, \zeta; \epsilon) = \text{Ai}(\epsilon - \zeta + \rho) \text{Ci}(\epsilon - \zeta - \rho). \quad (\text{B.2})$$

This result is easily verified by observing that (B.1) in this case reduces to the Laplace transform of the ballistic propagator in one dimension (using dimensionless units) and therefore must equal the well-known Green function of a freely falling particle in a single spatial dimension [Rob96]. Indeed, apart from scaling the integrals (B.1) for positive integer indices represent the stationary ballistic Green functions in the spaces of odd dimension $D = 2k + 1$. In particular, uniformly accelerated waves in physical space ($D = 3$) are represented by the function $\mathbb{Q}_1(\rho, \zeta; \epsilon)$ [DS76, BBG⁺98, KBK02].

From the definition (B.1), two recurrence formulae for increasing and decreasing value of the index k are immediately available:

$$\mathbb{Q}_{k+1}(\rho, \zeta; \epsilon) = -\frac{1}{2\rho} \frac{\partial}{\partial \rho} \mathbb{Q}_k(\rho, \zeta; \epsilon) = \left[-\frac{1}{2\rho} \frac{\partial}{\partial \rho} \right]^k \mathbb{Q}_0(\rho, \zeta; \epsilon), \quad (\text{B.3})$$

$$\mathbb{Q}_{-(k+1)}(\rho, \zeta; \epsilon) = \frac{\partial}{\partial \zeta} \mathbb{Q}_{-k}(\rho, \zeta; \epsilon) = \frac{\partial^k}{\partial \zeta^k} \mathbb{Q}_0(\rho, \zeta; \epsilon). \quad (\text{B.4})$$

(The latter equalities require $k \geq 0$.) From a practical point of view, the expressions thus obtained become rather unwieldy with growing $|k|$. The following five-point recursion relation, again easily verified using the integral representation (B.1), presents a favorable alternative:

$$\rho^2 \mathbb{Q}_{k+2}(\rho, \zeta; \epsilon) - \left(k + \frac{1}{2} \right) \mathbb{Q}_{k+1}(\rho, \zeta; \epsilon) + (\zeta - \epsilon) \mathbb{Q}_k(\rho, \zeta; \epsilon) + \frac{1}{4} \mathbb{Q}_{k-2}(\rho, \zeta; \epsilon) = 0. \quad (\text{B.5})$$

Finally, we inquire into the asymptotic behavior of (B.1) in the limit $\rho \rightarrow 0$. Here, we are interested in the case of integer index $k \geq 1$. Then, small values of τ provide the bulk contribution to the integral, which allows us to neglect the linear and cubic terms in the exponent of (B.1). In this approximation, the integral evaluates to a Gamma function of half-integer argument [AS65]:

$$Q_k(\rho, \zeta; \epsilon) \sim \frac{\Gamma(k - 1/2)}{2\pi^{3/2}\rho^{2k-1}} = \frac{(2k - 3)!!}{2^k \pi \rho^{2k-1}}. \quad (\text{B.6})$$

Therefore, the function $Q_k(\rho, \zeta; \epsilon)$ diverges as $\rho \rightarrow 0$. This singularity, however, affects only the real part of $Q_k(\rho, \zeta; \epsilon)$.

The functions $Q_i_k(\epsilon)$

Another important class of functions that regularly appears when calculating ballistic total currents is contained in (B.1) as a limiting case:

$$Q_i_k(\epsilon) = \lim_{\rho \rightarrow 0} \lim_{\zeta \rightarrow 0} \Im \{Q_k(\rho, \zeta; \epsilon)\}. \quad (\text{B.7})$$

Unlike the functions $Q_k(\rho, \zeta; \epsilon)$ that are divergent in this limit for $k > 0$ (reflecting the multipole source singularity), their imaginary parts $Q_i_k(\epsilon)$ remain well-defined. Obviously, $Q_i_0(\epsilon) = \text{Ai}(\epsilon)^2$, and all other expressions are available from suitably modified recurrences (B.3), (B.4):

$$Q_i_k(\epsilon) = \lim_{z \rightarrow 0} \left\{ \left[-\frac{1}{2z} \frac{\partial}{\partial z} \right]^k \text{Ai}(\epsilon + z) \text{Ai}(\epsilon - z) \right\}, \quad (\text{B.8})$$

$$Q_{i-k}(\epsilon) = \lim_{z \rightarrow 0} \left\{ \frac{\partial^k}{\partial z^k} \text{Ai}(\epsilon - z)^2 \right\}. \quad (\text{B.9})$$

($k \geq 0$). Thus, the functions $Q_i_k(\epsilon)$ can be extracted from the Taylor series of $\text{Ai}(\epsilon + z) \text{Ai}(\epsilon - z)$ and $\text{Ai}(\epsilon - z)^2$, respectively. For practical purposes, again the following recursion relation adapted from (B.5) proves more suitable:

$$\left(k + \frac{1}{2}\right) Q_{i_{k+1}}(\epsilon) + \epsilon Q_{i_k}(\epsilon) - \frac{1}{4} Q_{i_{k-2}}(\epsilon) = 0. \quad (\text{B.10})$$

For the sake of completeness, we note that unlike the functions $Q_k(\rho, \zeta; \epsilon)$ (B.1), the limits (B.7) can also be evaluated for half-integer index $Q_{i_{k+1/2}}(\epsilon)$, which in turn allows to calculate ballistic multipole currents in spaces of even dimension. Here, direct evaluation of the integral (B.1) shows that:

$$Q_{i_{1/2}}(\epsilon) = \frac{1}{2\sqrt{\pi}} \left\{ \frac{1}{3} - \text{Ai}_1(2^{2/3}\epsilon) \right\} \quad (\text{B.11})$$

holds, where $\text{Ai}_1(u) = \int_0^u dz \text{Ai}(z)$ denotes the integral of the Airy function [AS65]. (In particular, $\text{Qi}_{1/2}(0) = 1/6\sqrt{\pi}$.) The other functions of half-integer index $\text{Qi}_{k+1/2}(\epsilon)$ are available from the differentiation formula:

$$\text{Qi}_{k-1/2}(\epsilon) = -\frac{\partial}{\partial \epsilon} \text{Qi}_{k+1/2}(\epsilon), \quad (\text{B.12})$$

as well as the recursion relation (B.10).

Appendix C

Useful relations involving Hermite polynomials

Most of the following formulae are given in [Buc53], § 13. The definition of the Hermite polynomials $\text{He}_n(z)$ reads

$$\text{He}_n(z) = (-1)^n e^{z^2/2} \frac{d^n}{dz^n} \left(e^{-z^2/2} \right). \quad (\text{C.1})$$

Two recurrence relations are particularly useful:

$$\text{He}_{n+1}(z) = z \text{He}_n(z) - n \text{He}_{n-1}(z), \quad (\text{C.2})$$

$$\frac{d}{dz} \text{He}_n(z) = n \text{He}_{n-1}(z). \quad (\text{C.3})$$

Using these relations we calculate

$$\mathcal{N}_k(\epsilon) = \frac{1}{k!} \int_{-\infty}^{\epsilon} dz e^{-z^2/2} [\text{He}_k(z)]^2. \quad (\text{C.4})$$

From equation (C.1) we get

$$\mathcal{N}_k(\epsilon) = \frac{(-1)^k}{k!} \int_{-\infty}^{\epsilon} dz \text{He}_k(z) \frac{d^k}{dz^k} \left(e^{-z^2/2} \right). \quad (\text{C.5})$$

Next we employ the second recurrence relation and integrate by parts:

$$\begin{aligned} \mathcal{N}_k(\epsilon) &= \frac{(-1)^k}{k!} \text{He}_k(\epsilon) \left(\frac{d}{dz} \right)^{k-1} e^{-z^2/2} \Big|_{z=\epsilon} + \\ &\quad + \frac{(-1)^{(k-1)}}{k!} \int_{-\infty}^{\epsilon} dz \left[\frac{d}{dz} \text{He}_k(z) \right] \left[\frac{d^{k-1}}{dz^{k-1}} \left(e^{-z^2/2} \right) \right] \\ &= \frac{-1}{k!} \text{He}_k(\epsilon) \text{He}_{k-1}(\epsilon) e^{-\epsilon^2/2} + \mathcal{N}_{k-1}(\epsilon). \end{aligned} \quad (\text{C.6})$$

Since $\mathcal{N}_0(\epsilon)$ evaluates to an error function [AS65],

$$\mathcal{N}_0(\epsilon) = \int_{-\infty}^{\epsilon} dz e^{-z^2/2} = \sqrt{\frac{\pi}{2}} \left[1 + \operatorname{erf} \left(\frac{\epsilon}{\sqrt{2}} \right) \right], \quad (\text{C.7})$$

repeated usage of equation (C.6) yields the final result

$$\mathcal{N}_k(\epsilon) = \sqrt{\frac{\pi}{2}} \left[1 + \operatorname{erf} \left(\frac{\epsilon}{\sqrt{2}} \right) \right] - \sum_{n=0}^{k-1} \frac{1}{(n+1)!} \operatorname{He}_n(\epsilon) \operatorname{He}_{n+1}(\epsilon) e^{-\epsilon^2/2}. \quad (\text{C.8})$$

Appendix D

Series expansion for the reflection approximation

We start from the expression for the total current in a homogeneous force field given in equation (2.42). The time-dependent propagator in D dimensions reads

$$K(x, y, z, t|x', y', z', 0) = \left(\frac{m}{2\pi i \hbar t}\right)^{D/2} \exp \left\{ \frac{i}{\hbar} \left[\frac{m}{2t} |\mathbf{r} - \mathbf{r}'|^2 + \frac{Ft}{2}(z + z') - \frac{F^2 t^3}{24m} \right] \right\}. \quad (\text{D.1})$$

Thus the total current becomes

$$J(E) = \frac{1}{\hbar^2} \int_{R^{2D+1}} d^D \mathbf{r} d^D \mathbf{r}' dt \left(\frac{m}{2\pi i \hbar t}\right)^{D/2} e^{iEt/\hbar} e^{\frac{i}{\hbar} \left[\frac{m}{2t} |\mathbf{r} - \mathbf{r}'|^2 + \frac{Ft}{2}(z + z') - \frac{F^2 t^3}{24m} \right]} \sigma(\mathbf{r})^* \sigma(\mathbf{r}'). \quad (\text{D.2})$$

Introducing the usual set of scaled variables from equation (7.4) (however, not for the spatial coordinates) we obtain

$$J(E) = \frac{2\beta}{\hbar} (\beta F)^D \int_{R^{2D+1}} d^D \mathbf{r} d^D \mathbf{r}' d\tau \left(\frac{1}{i\pi\tau}\right)^{D/2} e^{i\tau\beta[F(z+z')+2E] + \frac{i}{\tau}(\beta F)^2 |\mathbf{r} - \mathbf{r}'|^2 - \frac{i\tau^3}{12}} \sigma(\mathbf{r})^* \sigma(\mathbf{r}'). \quad (\text{D.3})$$

In the next step we switch to relative coordinates defined by

$$(x, y, z) = (u + u', v + v', w + w'), \quad (\text{D.4})$$

$$(x', y', z') = (u - u', v - v', w - w'), \quad (\text{D.5})$$

and

$$(u, v, w) = \mathbf{s}, \quad (\text{D.6})$$

$$(u', v', w') = \mathbf{s}'. \quad (\text{D.7})$$

Using these variables, the new expression for the total current is given by

$$J(E) = \frac{2\beta(2\beta F)^D}{\hbar} \int_{R^{2D+1}} d^D \mathbf{s} d^D \mathbf{s}' d\tau \left(\frac{1}{i\pi\tau}\right)^{D/2} \times \\ \times e^{2i\tau\beta(\mathbf{F}\cdot\mathbf{s}+E)} e^{\frac{i}{\tau}4(\beta F)^2 |\mathbf{s}'|^2 - \frac{i\tau^3}{12}} \sigma(\mathbf{s} + \mathbf{s}')^* \sigma(\mathbf{s} - \mathbf{s}'). \quad (\text{D.8})$$

Series expansion in one dimension

As a tutorial example we study the one-dimensional problem. Assuming that σ is a real-valued source function, we first expand $h(s, s') = \sigma(s + s')^* \sigma(s - s')$ around $s' = 0$:

$$\begin{aligned} h(s, s') &\approx h(s) + \frac{1}{2!} h''(s) s'^2 + \frac{1}{4!} h^{(4)}(s) s'^4 + \dots \\ &= h_0(s) + h_1(s) s'^2 + h_2(s) s'^4 + \dots + h_n(s) s'^{2n} + \dots \end{aligned} \quad (\text{D.9})$$

We can perform the integration over s' and get

$$\int ds' e^{\frac{i}{\tau} 4(\beta F)^2 s'^2} h(s, s') = \frac{(i\tau)^{1/2}}{2\beta F} \sum_{n=0}^{\infty} \Gamma(n + 1/2) \frac{(i\tau)^n}{(2\beta F)^{2n}} h_n(s). \quad (\text{D.10})$$

The τ integration is also feasible and yields

$$\int d\tau (i\tau)^n e^{2i\tau\beta(Fs+E) - \frac{i\tau^3}{12}} = 2\pi(-1)^n \text{Ai}^{(n)}[-2^{5/3}\beta(E + Fs)] \quad (\text{D.11})$$

Inserting these results into the original equation (D.8) we obtain

$$J(E) = \frac{4\beta}{\hbar} \pi^{1/2} \sum_{n=0}^{\infty} \Gamma(n + 1/2) \frac{(-1)^n}{(2\beta F)^{2n}} \int_R ds h_n(s) \text{Ai}^{(n)}[-2^{5/3}\beta(E + Fs)]. \quad (\text{D.12})$$

A further simplification can be achieved by approximating the Airy functions with δ functions. Formally, we exploit the relation

$$\delta^{(n)}(x) = \lim_{\beta \rightarrow \infty} \beta^{n+1} \text{Ai}^{(n)}(\beta x), \quad (\text{D.13})$$

to get a new expression:

$$J(E) = -\frac{2}{\hbar} \pi^{1/2} \sum_{n=0}^{\infty} \frac{\Gamma(n + 1/2)}{(2\beta F)^{3n} F} \int_R ds h_n(s) \delta^{(n)}(s + E/F). \quad (\text{D.14})$$

Integration by parts $\int ds f(s) \delta^{(n)}(s) = (-1)^n \int ds f^{(n)}(s) \delta(s)$ yields

$$J(E) = -\frac{2}{\hbar} \pi^{1/2} \sum_{n=0}^{\infty} \frac{\Gamma(n + 1/2)}{(2\beta F)^{3n} F} (-1)^n h_n^{(n)}(-E/F). \quad (\text{D.15})$$

References

- [Arf70] G. Arfken. *Mathematical Methods for Physicists*. Academic Press, New York, 2nd edition, 1970.
- [AS65] M. Abramowitz and I.A. Stegun. *Handbook of Mathematical Functions*. Dover, New York, 1965.
- [ASRVK01] J.R. Abo-Shaeer, C. Raman, J.M. Vogels, and W. Ketterle. Observation of vortex lattices in Bose-Einstein condensates. *Science*, 292:476, 2001.
- [Bar61] V. Bargmann. On a Hilbert space of analytic functions and an associated integral transform, part i. *Communications on pure and applied mathematics*, 14:187–214, 1961.
- [Bar67] V. Bargmann. On a Hilbert space of analytic functions and an associated integral transform, part ii. *Communications on pure and applied mathematics*, 20:1–101, 1967.
- [Bar70] V. Bargmann. Group representations on Hilbert spaces of analytic functions. In R. P. Gilbert and R. G. Newton, editors, *Analytic methods in mathematical physics*. Gordon and Breach Science Publishers, New York, 1970.
- [Bay78] B.F. Bayman. A generalization of the spherical harmonic gradient formula. *J. Math. Phys.*, 19:2558, 1978.
- [BBG⁺98] C. Bracher, W. Becker, S.A. Gurvitz, M. Kleber, and M.S. Marinov. Three-dimensional tunneling in quantum ballistic motion. *Am. J. Phys.*, 66:38, 1998.
- [BDD96] C. Blondel, C. Delsart, and F. Dulieu. The photodetachment microscope. *Phys. Rev. Lett.*, 77:3755, 1996.
- [BDDV99] C. Blondel, C. Delsart, F. Dulieu, and C. Valli. Photodetachment microscopy of O⁻. *Eur. Phys. J. D*, 5:207, 1999.
- [BHE99] I. Bloch, T.W. Hänsch, and T. Esslinger. Atom laser with a cw output coupler. *Phys. Rev. Lett.*, 82:3008, 1999.

- [BIL79] W. A. M. Blumberg, W. M. Itano, and D. J. Larson. Theory of the photodetachment of negative ions in a magnetic field. *Physical Review D*, 19:139–148, 1979.
- [BJL78] W. A. M. Blumberg, R. M. Jopson, and D. J. Larson. Precision laser photodetachment spectroscopy in magnetic fields. *Physical Review Letters*, 40:1320–1323, 1978.
- [BJT99] Y.B. Band, P.S. Julienne, and M. Trippenbach. Radio frequency output coupling of the Bose-Einstein condensate for atom lasers. *Phys. Rev. A*, 59:3823, 1999.
- [BKK02] C. Bracher, T. Kramer, and M. Kleber. Ballistic matter waves with angular momentum: Exact solutions and applications. *accepted for publication in Phys. Rev. A*, 2002. arXiv:quant-ph/0207105.
- [BR99] D.A. Butts and D.S. Rokhsar. Predicted signatures of rotating Bose-Einstein condensates. *Nature*, 397:327, 1999.
- [Bra99] C. Bracher. *Quantum Ballistic Motion and its Applications*. PhD thesis, Technische Universität München, 1999. Unpublished.
- [Bri85] D.M. Brink. *Semi-classical methods for nucleus-nucleus scattering*. Cambridge University Press, Cambridge, 1985.
- [BRK97] C. Bracher, M. Riza, and M. Kleber. Propagator theory in scanning tunneling microscopy. *Phys. Rev. B*, 56:7704, 1997.
- [BS00] R.J. Ballagh and C.M. Savage. The theory of atom lasers. *Modern Physics Letters B*, 14:153, 2000.
- [Buc53] H. Buchholz. *Die Konfluente Hypergeometrische Funktion*, volume 2 of *Ergebnisse der angewandten Mathematik*. Springer, 1953.
- [BV71] V.L. Bakhrakh and S.I. Vetchinkin. Green’s functions of the Schrödinger equation for the simplest systems. *Theoret. Math. Phys.*, 6:283, 1971. [Teoret. Mat. Fiz. 6, 392–402 (1971)].
- [Con28] E.U. Condon. Nuclear motions associated with electron transitions in diatomic molecules. *Phys. Rev.*, 32:858, 1928.
- [DD89] M.L. Du and J.B. Delos. Effect of an electric field on the photodetachment of H^- . *Phys. Lett. A*, 134:476, 1989.
- [DGL⁺99] L. Dobrek, M. Gajda, M. Lewenstein, K. Sengstock, G. Birkl, and W. Ertmer. Optical generation of vortices in trapped Bose-Einstein condensates. *Phys. Lett. A*, 51:133, 1999.

- [DGPS99] F. Dalfovo, S. Giorgini, L.P. Pitaevskii, and S. Stringari. Theory of Bose-Einstein condensation in trapped gases. *Rev. Mod. Phys.*, 71:463, 1999.
- [DKO82] Yu.N. Demkov, V.D. Kondratovich, and V.N. Ostrovskii. Interference of electrons resulting from the photoionization of an atom in an electric field. *JETP Lett.*, 34:403, 1982. [Pis'ma Zh. Eksp. Teor. Fiz. 34, 425–427 (1981)].
- [DMM75] V.V. Dodonov, I.A. Malkin, and V. Man'ko. The Green function of the stationary Schrödinger equation for a particle in a uniform magnetic field. *Phys. Lett. A*, 51:133, 1975.
- [DR01] W. Dittrich and M. Reuter. *Classical and Quantum Dynamics*. Springer, Berlin, 3rd edition, 2001.
- [DS76] F.I. Dalidchik and V.Z. Slonim. Strong exchange interaction effects in a homogeneous electric field. *Sov. Phys. JETP*, 43:25, 1976. [Zh. Eksp. Teor. Fiz. 70, 47–60 (1976)].
- [dSdSD88] C.F. de Souza and A. de Souza Dutra. Galilean transformation and the path integral propagator for a crossed electric and magnetic field. *Am. J. Phys.*, 57:330, 1988.
- [Dun68] G.H. Dunn. Photodissociation of H_2^+ and D_2^+ : Theory. *Phys. Rev.*, 172:1, 1968.
- [EB95] M. Edwards and K. Burnett. Numerical solution of the nonlinear Schrödinger equation for small samples of trapped atoms. *Phys. Rev. A*, 51:1382, 1995.
- [ECHC02] P. Engels, I. Coddington, P. C. Haljan, and E. A. Cornell. Nonequilibrium effects of anisotropic compression applied to vortex lattices in Bose-Einstein condensates. *Phys. Rev. Lett.*, 89:100403, 2002.
- [Eco83] E.N. Economou. *Green's Functions in Quantum Physics (Solid-State Sciences 7)*. Springer, Berlin, 1983.
- [EDC⁺96] M. Edwards, R.J. Dodd, C.W. Clark, P.A. Ruprecht, and K. Burnett. Properties of a Bose-Einstein condensate in an anisotropic harmonic potential. *Phys. Rev. A*, 53:R1950, 1996.
- [Edm57] A.R. Edmonds. *Angular Momentum in Quantum Mechanics*. Princeton University Press, Princeton, 1957.
- [Fab81] I.I. Fabrikant. Interference effects in photodetachment and photoionization of atoms in a homogeneous electric field. *Sov. Phys. JETP*, 52:1045, 1981. [Zh. Eksp. Teor. Fiz. 79, 2070–2077 (1980)].

- [Fab91] I.I. Fabrikant. Near-threshold photodetachment of H^- in parallel and crossed electric and magnetic fields. *Phys. Rev. A*, 43:258, 1991.
- [FH65] R.P. Feynman and A.R. Hibbs. *Quantum Mechanics and Path Integrals*. McGraw-Hill, New York, 1965.
- [Fra25] J. Franck. Elementary processes of photochemical reactions. *Trans. Faraday Soc.*, 21:536, 1925.
- [FS01] A.L. Fetter and A.A. Svidzinsky. Rotating vortex lattice in a Bose-Einstein condensate trapped in combined quadratic and quartic radial potentials. *J. Phys.: Condens. Matter*, 13:R135, 2001.
- [FW71] A.L. Fetter and J.D. Walecka. *Quantum theory of many-particle systems*. McGraw-Hill, New York, 1971.
- [Gal38] G. Galilei. *Discorsi e dimostrazioni matematiche intorno a due nuove scienze attenenti alla meccanica & i movimenti locali*. Leiden, 1638.
- [GBA01] F. Gerbier, P. Boyer, and A. Aspect. Quasicontinuous atom laser in the presence of gravity. *Phys. Rev. Lett.*, 86(21):4729, May 2001.
- [Gis73] E.A. Gislason. Series expansion of Franck-Condon factors. I. Linear potential and the reflection approximation. *Journal of Chemical Physics*, 58:3702, 1973.
- [GKK91] B. Gottlieb, M. Kleber, and J. Krause. Tunneling from a 3-dimensional quantum well in an electric field: an analytic solution. *Z. Phys. A – Hadrons and Nuclei*, 339:201, 1991.
- [Gou72] G. Gountaroulis. Green-function of the free electron in a uniform magnetic field. *Phys. Lett. A*, 40:132, 1972.
- [GP91] A. Galindo and P. Pascual. *Quantum Mechanics II*. Springer, Berlin, 1991.
- [GP00] G. Grosso and G.P. Parravicini. *Solid State Physics*. Academic Press, New York, 2000.
- [GS98] C. Grosche and F. Steiner. *Handbook of Feynman Path Integrals*, volume 145 of *Springer Tracts in Modern Physics*. Springer, Berlin, 1998.
- [HACC01] P.C. Haljan, B.P. Anderson, I. Coddington, and E.A. Cornell. Use of surface-wave spectroscopy to characterize tilt modes of a vortex in a Bose-Einstein condensate. *Phys. Rev. Lett.*, 86(14):2922, April 2001.
- [HCF86] N.J.M. Horing, H.L. Cui, and G. Fiorenza. Nonrelativistic Schrödinger Green's function for crossed time-dependent electric and magnetic fields. *Phys. Rev. A*, 34:612, 1986.

- [HE98] B. Hüpper and B. Eckhardt. Uniform semiclassical expansion for the direct part of Franck-Condon transitions. *Phys. Rev. A*, 57:1536, 1998.
- [HE99] B. Hüpper and B. Eckhardt. Uniform semiclassical calculation of the direct part of the photodissociation cross section of water. *Journal of Chemical Physics*, 110:11749, 1999.
- [Hel78] E.J. Heller. Quantum corrections to classical photodissociation models. *J. Chem. Phys.*, 68(5):2066, March 1978.
- [Her50] G. Herzberg. *Molecular Spectra and Molecular Structure*. D. van Nostrand, 1950.
- [Ho01] T.-L. Ho. Bose-Einstein condensates with large number of vortices. *Phys. Rev. Lett.*, 87(6):060403–1, August 2001.
- [Hob31] E.W. Hobson. *The Theory of Spherical and Ellipsoidal Harmonics*. Cambridge University Press, Cambridge, 1931.
- [Hor65] N.J.M. Horing. Quantum theory of electron gas plasma oscillation in a magnetic field. *Annals of Physics*, 31:1, 1965.
- [HP64] L. Hostler and R.H. Pratt. Coulomb Green's function in closed form. *Phys. Rev. Lett.*, 10:469, 1964.
- [HS52] I. Halperin and L. Schwartz. *Introduction to the Theory of Distributions*. University of Toronto Press, Toronto, 1952.
- [Jac75] J.D. Jackson. *Classical Electrodynamics*. Wiley, New York, 2nd edition, 1975.
- [JP71] A.V. Jones and G.J. Papadopoulos. On the exact propagator. *Journal of Physics A*, 4:L86, 1971.
- [JS72] H. Jeffreys and B. Swirles. *Methods of Mathematical Physics*. Cambridge University Press, London, 3rd edition, 1972.
- [KBK01] T. Kramer, C. Bracher, and M. Kleber. Four-path interference and uncertainty principle in photodetachment microscopy. *Europhys. Lett.*, 56:471, 2001.
- [KBK02] T. Kramer, C. Bracher, and M. Kleber. Matter waves from quantum sources in a force field. *J. Phys. A: Math. Gen.*, 35:8361, 2002.
- [KDP80] K.v. Klitzing, G. Dorda, and M. Pepper. New method for high-accuracy determination of the fine-structure constant based on quantized Hall resistance. *Phys. Rev. Lett.*, 45:494, 1980.

- [Ken27] E.H. Kennard. Zur Quantenmechanik einfacher Bewegungstypen. *Zeitschrift für Physik*, 44:326–352, 1927.
- [KHN93] S. Kawaji, K. Hirakawa, and M. Nagata. Device-width dependence of plateau width in quantum Hall states. *Physica B*, 184:17–20, 1993.
- [Kle90] H. Kleinert. *Path integrals in quantum mechanics, statistics and polymer physics*. World Scientific, Singapore, 1990.
- [Kra00] T. Kramer. *Quantum ballistic motion in uniform electric and magnetic fields*. Diploma thesis, Technische Universität München, 2000. Unpublished.
- [Ler90] J. Lermé. Iterative methods to compute one- and two-dimensional Franck-Condon factors. Tests of accuracy and applications to study indirect molecular transitions. *Chemical Physics*, 145:67–88, 1990.
- [LLF90] Y.L. Li, C.H. Liu, and S.J. Franke. Three-dimensional Green’s function for wave propagation in a linearly inhomogeneous medium—the exact analytic solution. *J. Acoust. Soc. Am.*, 87:2285, 1990.
- [Loh92] A. Lohr. *Tunneln im Magnetfeld*. Diploma thesis, Technische Universität München, 1992. Unpublished.
- [MAH⁺99] M.R. Matthews, B.P. Anderson, P.C. Haljan, D.S. Hall, C.E. Wieman, and E.A. Cornell. Vortices in a Bose-Einstein condensate. *Phys. Rev. Lett.*, 83:2498, 1999.
- [MAK⁺97] M.-O. Mewes, M.R. Andrews, D.M. Kurn, D.S. Durfee, C.G. Townsend, and W. Ketterle. Output coupler for Bose-Einstein condensed atoms. *Phys. Rev. Lett.*, 78:582, 1997.
- [MCWD00] K.W. Madison, F. Chevy, W. Wohlleben, and J. Dalibard. Vortex formation in a stirred Bose-Einstein condensate. *Phys. Rev. Lett.*, 84:806, 2000.
- [Mer69] E. Merzbacher. *Quantum Mechanics*. Wiley, New-York, 2nd edition, 1969.
- [Mes64] A. Messiah. *Quantum Mechanics*, volume 1. North-Holland, Amsterdam, 1964.
- [MF53] P.M. Morse and H. Feshbach. *Methods of Theoretical Physics*, volume 2. McGraw-Hill, New York, 1953.
- [MJ59] G. Möllenstedt and C. Jönsson. Elektronen-Mehrfachinterferenzen an regelmäßig hergestellten Feinspalten. *Z. Phys.*, 155:472, 1959.
- [Mos52] M. Moshinsky. Diffraction in time. *Phys. Rev.*, 88:625, 1952.

- [MQ71] M. Moshinsky and C. Quesne. Linear canonical transformations and their unitary representations. *Journal of Mathematical Physics*, 12:1772–1780, 1971.
- [Mül66] C. Müller. *Spherical Harmonics (Lecture Notes in Mathematics Vol. 17)*. Springer, Berlin, 1966.
- [MW80] M. Moshinsky and P. Winternitz. Quadratic Hamiltonians in phase space and their eigenstates. *Journal of Mathematical Physics*, 21:1667–1682, 1980.
- [Nie92] L. M. Nieto. Green’s function for crossed time-dependent electric and magnetic fields. phase-space quantum mechanics approach. *Journal of mathematical physics*, 33(10):3402–3409, 1992.
- [OFS⁺01] H. Ott, J. Fortagh, G. Schlotterbeck, A. Grossmann, and C. Zimmermann. Bose-Einstein condensation in a surface microtrap. *Phys. Rev. Lett.*, 87:230401–1, 2001.
- [Pau51] W. Pauli. *Ausgewählte Kapitel aus der Feldquantisierung*. Zürich, 1950/51.
- [PD93] A. D. Peters and J. B. Delos. Photodetachment cross-section of H^- in crossed electric and magnetic-fields. 1. Closed-orbit theory. *Phys. Rev. A*, 47:3020–3035, 1993.
- [PG87] R.E. Prange and S.M. Girvin, editors. *The Quantum Hall effect*. Springer, Berlin, 1987.
- [PGMC⁺97] V.M. Pérez-García, H. Michinel, J.I. Cirac, M. Lewenstein, and P. Zoller. Dynamics of Bose-Einstein condensates: Variational solution to the Gross-Pitaevskii equations. *Phys. Rev. A*, 56:1424, 1997.
- [PJGD97] A. D. Peters, C. Jaffe, J. Gao, and J. B. Delos. Quantum manifestations of bifurcations of closed orbits in the photodetachment cross section of H^- in parallel fields. *Phys. Rev. A*, 56:345–355, 1997.
- [PS02] C. J. Pethick and H. Smith. *Bose-Einstein condensation in dilute gases*. Cambridge University Press, Cambridge, 2002.
- [PTG82] M.A. Paalanen, D.C. Tsui, and A.C. Gossard. Quantized Hall effect at low temperatures. *Phys. Rev. B*, 25:5566, 1982.
- [RHH99] J. Reichel, W. Hänsel, and T.W. Hänsch. Atomic micromanipulation with magnetic surface traps. *Phys. Rev. Lett.*, 83:3398, 1999.
- [Rob96] R.W. Robinett. Quantum mechanical time-development operator for the uniformly accelerated particle. *Am. J. Phys.*, 64:803, 1996.
- [Row78] E.G.P. Rowe. Spherical delta functions and multipole expansions. *J. Math. Phys.*, 19:1962, 1978.

- [Sch51] J. Schwinger. On gauge invariance and vacuum polarization. *Phys. Rev.*, 82:664, 1951.
- [Sch73] J. Schwinger. *Particles, Sources, and Fields*, volume 2. Addison-Wesley, 1973.
- [SOK98] T. Shimada, T. Okamoto, and S. Kawaji. Hall electric field-dependent broadening of extended state bands in Landau levels and breakdown of the quantum Hall effect. *Physica B*, 249-251:107–110, 1998.
- [SS99] J. Schneider and A. Schenzle. Output from an atom laser: theory vs. experiment. *Applied Physics B*, 69:353, 1999.
- [SS00] J. Schneider and A. Schenzle. Investigation of a two-mode atom laser model. *Phys. Rev. A*, 61:053611–1, 2000.
- [TH83] J. Tersoff and D.R. Hamann. Theory and application for the scanning tunneling microscope. *Phys. Rev. Lett.*, 50:1998, 1983.
- [Wig48] E.P. Wigner. On the behavior of cross sections near thresholds. *Phys. Rev.*, 73:1002, 1948.
- [WS83] E.J. Weniger and E.O. Steinborn. New representations for the spherical tensor gradient and the spherical delta function. *J. Math. Phys.*, 24:2553, 1983.
- [WS93] Q. Wang and A.F. Starace. Short-pulse detachment of H^- in the presence of a static electric field. *Phys. Rev. A*, 48:R1741, 1993.
- [WTSS92] J.K. Wang, D.C. Tsui, M. Santos, and M. Shayegan. Heat capacity study of two-dimensional electrons in GaAs/ $Al_xGa_{1-x}As$ multiple-quantum-well structures in high magnetic fields: Spin-split Landau levels. *Phys. Rev. B*, 45:4384, 1992.
- [YKB03] J.N. Yukich, T. Kramer, and C. Bracher. Negative-ion photodetachment in parallel electric and magnetic fields. *in preparation*, 2003.
- [ZDM99] Y. Zhao, M. Du, and J. Mao. Formula for laser pulse photodetachments of negative ions. *J. Phys. B: At. Mol. Phys.*, 32:1409, 1999.

List of publications

- [1] T. Kramer, C. Bracher, and M. Kleber. Four-path interference and uncertainty principle in photodetachment microscopy. *Europhys. Lett.*, 56:471, 2001.
- [2] T. Kramer, C. Bracher, and M. Kleber. Matter waves from quantum sources in a force field. *J. Phys. A: Math. Gen.*, 35:8361, 2002.
- [3] C. Bracher, T. Kramer, and M. Kleber. Ballistic matter waves with angular momentum: Exact solutions and applications. *accepted for publication in Phys. Rev. A*, 2002. arXiv:quant-ph/0207105.
- [4] T. Kramer, C. Bracher, and M. Kleber. Density of states in crossed magnetic and electric fields. *submitted for publication*, 2003.
- [5] B. Donner, C. Bracher, M. Kleber, T. Kramer, and H.J. Kreuzer. Corrugation amplification in scanning tunneling microscopy. *submitted for publication*, 2003.
- [6] J.N. Yukich, T. Kramer, and C. Bracher. Negative-ion photodetachment in parallel electric and magnetic fields. *in preparation*, 2003.

Danksagung

Mein Dank gilt an erster Stelle Prof. Dr. Manfred Kleber, der diese Arbeit vorzüglich betreut hat. Bei allen anstehenden Problemen hatte er immer ein offenes Ohr und verhalf mit stets konstruktiven Vorschlägen der Arbeit zu neuem Schwung. Eine Doktorarbeit muss zum Glück nicht bei Null beginnen und daher ist es mir ein Vergnügen meinen jetzigen und früheren Mitstreitern in der Arbeitsgruppe zu danken: Dipl.-Phys. Bernd Donner, Dr. Andreas Lohr, Dr. Richard Kopold und Dr. Mustafa Riza. Ganz besonders aber freue ich mich über die hervorragende Zusammenarbeit mit Dr. Christian Bracher, mit dem ich lange Zeit das Uni-Zimmer sowie Freud und Leid geteilt habe.

Neben der Physik darf man auch noch leben. Dazu haben meine Eltern, die Familie meines Bruders Dr. Linus Kramer, sowie besonders Julianna Zdunich und Andreas Weber beigetragen. Vielen Dank für Eure Freundschaft und Unterstützung!

Nicht unerwähnt lassen möchte ich die Förderung meines Studiums und dieser Arbeit durch die Studienstiftung des deutschen Volkes, die Deutsche Forschungsgemeinschaft und die Leonhard-Lorenz Stiftung.

Lebenslauf

Dipl.-Phys. Tobias Kramer
Wandeltstr. 2
80805 München

19.6.1974	Geboren in Tübingen.
1980 – 1984	Besuch der Grundschule „Waldhäuser-Ost“ in Tübingen.
1984 – 1993	Besuch des Ludwig-Uhland-Gymnasiums in Tübingen
11.5.1993	Abitur (Note 1.0).
2.8.1993 – 31.10.1994	Zivildienst in der Radioonkologischen Universitätsklinik Tübingen, Abteilung für Medizinische Physik.
1994 – 1996	Studium der Physik an der Universität Tübingen.
30.7.1996	Vordiplom in Physik (Note: „sehr gut“).
Juli 1996 – Juli 2000	Förderung durch die Studienstiftung des deutschen Volkes.
1996 – 1997	Einjähriger Aufenthalt und Studium in den USA an der University of Colorado at Boulder, Colorado, USA, mit Unterstützung der Studienstiftung des deutschen Volkes und der Universität Tübingen. Studium der Physik, Astrophysik, Astronomie und Ozeandynamik.
1997 – 2000	Studium der Physik an der Technischen Universität München.
1999 – 2000	Diplomarbeit an der Technischen Universität München in der theoretischen Physik mit dem Thema „Quantum Ballistic Motion in Uniform Electric and Magnetic Fields“.
26.7.2000	Diplom in Physik (Note 1.0, Prädikat „mit Auszeichnung bestanden“), Nebenfächer „Allgemeine Relativitätstheorie“, „Theoretische Festkörperphysik“ und „Fortgeschrittene Quantenmechanik“.
2000 – heute	Wissenschaftlicher Angestellter an der Technischen Universität München, Doktorand in theoretischer Physik bei Prof. Dr. M. Kleber, Institut für theoretische Physik der TU München.